FINAL REPORT:

RESEARCH STUDY
ON STELLAR X-RAY
IMAGING EXPERIMENT

HENRY H. WILSON
LEON P. VANSPEYBROECK

CONTRACT NO. NAS8 - 24385

PERIOD COVERED:
JUNE 12, 1969 - MARCH 31, 1972

PREPARED FOR:
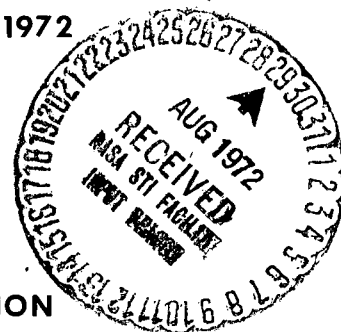
NATIONAL AERONAUTICS
AND SPACE ADMINISTRATION
GEORGE C. MARSHALL
SPACE FLIGHT CENTER
MARSHALL SPACE FLIGHT CENTER, ALABAMA 35812

Final Report

RESEARCH STUDY ON STELLAR X-RAY
IMAGING EXPERIMENT

Period Covered:

June 12, 1969 - March 31, 1972

Contract No.   NAS8-24385

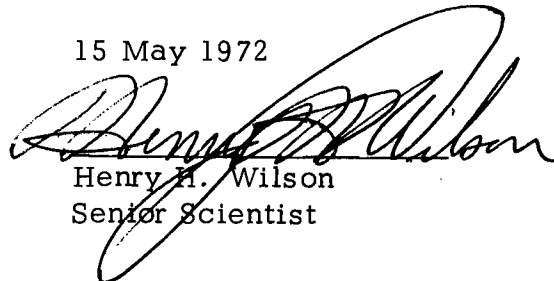Henry H. Wilson
Leon P. VanSpeybroeck

Prepared for:

National Aeronautics and Space Administration
George C. Marshall Space Flight Center
Marshall Space Flight Center, Alabama 35812

Prepared by:

American Science & Engineering, Inc.
955 Massachusetts Avenue
Cambridge, Massachusetts 02139

15 May 1972

Details of illustrations in
this document may be better
studied on microfiche

Henry H. Wilson
Senior Scientist

Approved _____   Approved _____
Leon P. VanSpeybroeck   Herbert Gursky
Project Scientist   Vice President
                                   Space Research
                                   Division

CONTENTS

ILLUSTRATIONS

1.0 INTRODUCTION

This document is being submitted in fulfillment of the Final Report requirement of Contract NAS8-24385 and as such, covers the period from 12 June 1969 through 31 March 1972. The program is being continued under the LOXT HEAO-C Mission Phase B study.

This research study on stellar X-ray imaging concentrated on two areas - the use of Microchannel Plates (MCP) as focal plane read-out devices and the evaluation of mirrors for the X-ray telescopes. The microchannel plate outputs were either imaged on a phosphor screen which was viewed by a low light level vidicon or on a wire array which was read out by digitally processing the output of a charge division network attached to the wires.

A life test has been carried out on two image intensifiers employing microchannel plates. These devices have been maintained in an ion pumped vacuum at pressures between 10^{-8} and 10^{-9} torr for over a year. Both plates have been exposed to greater than 10^{10} incident quanta from ^{55}Fe sources. One of the units has been evaluated continuously with no loss of efficiency and with a gain loss of ten percent or less indicated. The other unit was initially too noisy for evaluation, but this problem has now abated and this unit is performing usefully.

The microchannel plates have now been successfully imaged onto film and video cameras by means of phosphors and onto a wire array from which the position of the event was obtained by charge division. In the latter system the pulse from each end of the wire array was digitalized and minicomputer performed the necessary arithmetic to determine the position of the event.

The coating of microchannel plates with material having high secondary electron emission characteristics has been assayed but the results to date have been inconclusive with possibly higher gain, slightly increased noise and a somewhat lower quantum efficiency indicated.

We have evaluated the optical characteristics of X-ray telescopes of the paraboloid-hyperboloid type by means of a ray tracing procedure. Most of the results can be expressed as simple empirical formulae. These results include the theoretical resolution and vignetting factors for sources at a finite distance such as would be used in a test program. The principal result is that the resolution can be expressed as the sum of two terms, a term quadratic in the angle off axis and proportional to the grazing angle, and a second term which is linear in the angle off axis and proportional to the square of the grazing angle. The latter term, which always dominates for small off axis angles, can be eliminated by using the Wolter-Swartz shield solutions rather than the conic section designs.

We have also evaulated the effects of various environments upon the preliminary LOXT high resolution mirror design.

A system study was carried out with all participants in the LOXT program for the purpose of defining the design parameters for the Large Orbiting X-ray Telescope (HEAO-C) Mission. The results of this study are documented in Appendix B.

2.0 EVALUATION OF MICROCHANNEL PLATES

The purposes of the microchannel plate evaluation has been to determine the following:

1. The basic performance characteristics of microchannel plates under X-rays of various wave lengths. We have been primarily concerned with the quantum efficiency, gain and noise of these devices and have tacitly assumed that the resolution is that of the channel spacing as the associated readout equipment available to us has not approached this resolution.

2. Differences between microchannel plates supplied by various manufacturers (all other characteristics being the same or equatable).

3. The effect of coating the input faces and input ends of the channels of microchannel plates by vacuum deposition with materials having high secondary electron emission characteristics.

4. The life expectancy of these devices under a reasonably hard vacuum and with a flux level comparable to that expected in the HEAO-C Mission.

An X-ray image intensifier assembly is shown in Figure 2-1. The microchannel plate itself is not visible in this photograph as it is behind the fibre optic output and its phosphor.

2.1 Experimental Methods For Microchannel Plate Evaluation

To prevent oil contamination of the microchannel plates an ion-pumped vacuum system is required to contain the plate. In our system a high vacuum detector chamber (shown in Figure 2-2 and 2-3) contains the MCP, and a moderate vacuum chamber contains the X-ray source and other items requiring more frequent maintainance. A gate valve and organic window separate the source chamber from the detector chamber. The detector chamber is evacuated by an ion pump--titanium sublimation well combination, with sorption roughing. The chamber can be roughed from atmospheric

EL-005

Figure 2-1   An X-ray image intensifier.   The part nearest the camera is the
fiber optic output.
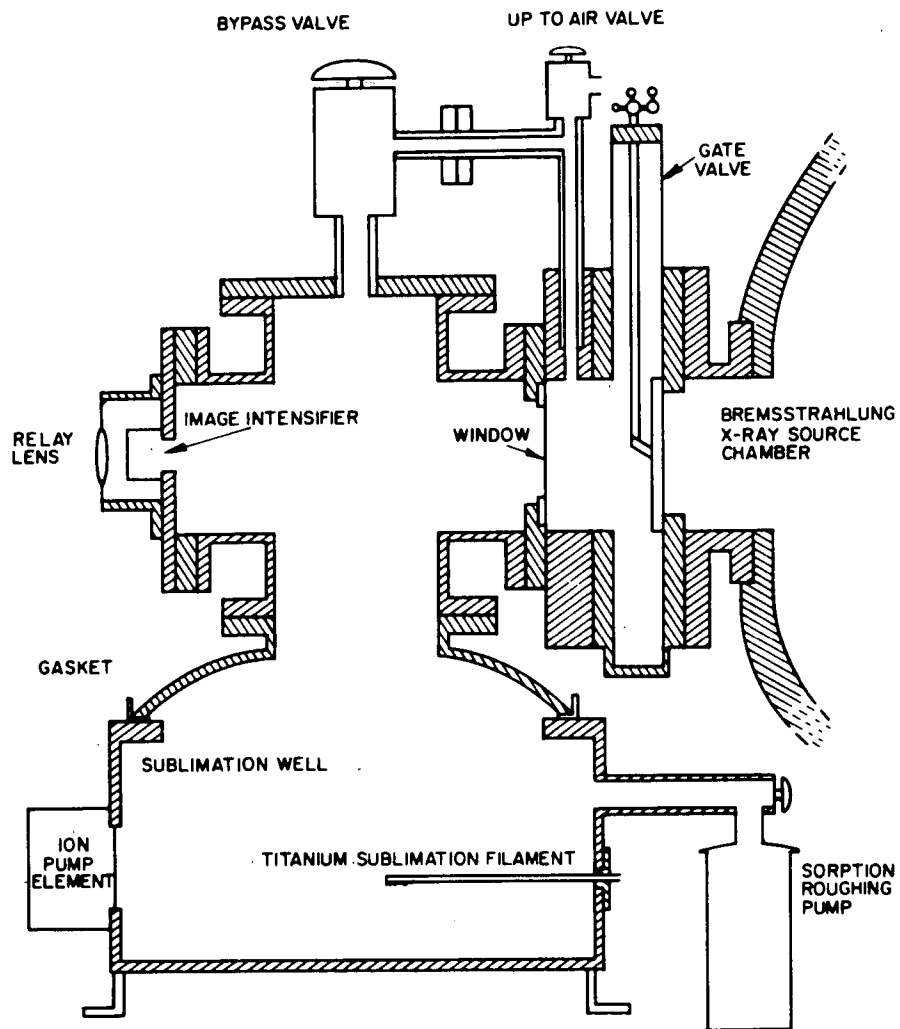
Figure 2-2. The X-ray image intensifier test facility. With the gate valve open and the bypass valve closed, the image intensifier is operated in clean high vacuum, while X-rays from the source chamber pass through the window and irradiate the MCP.
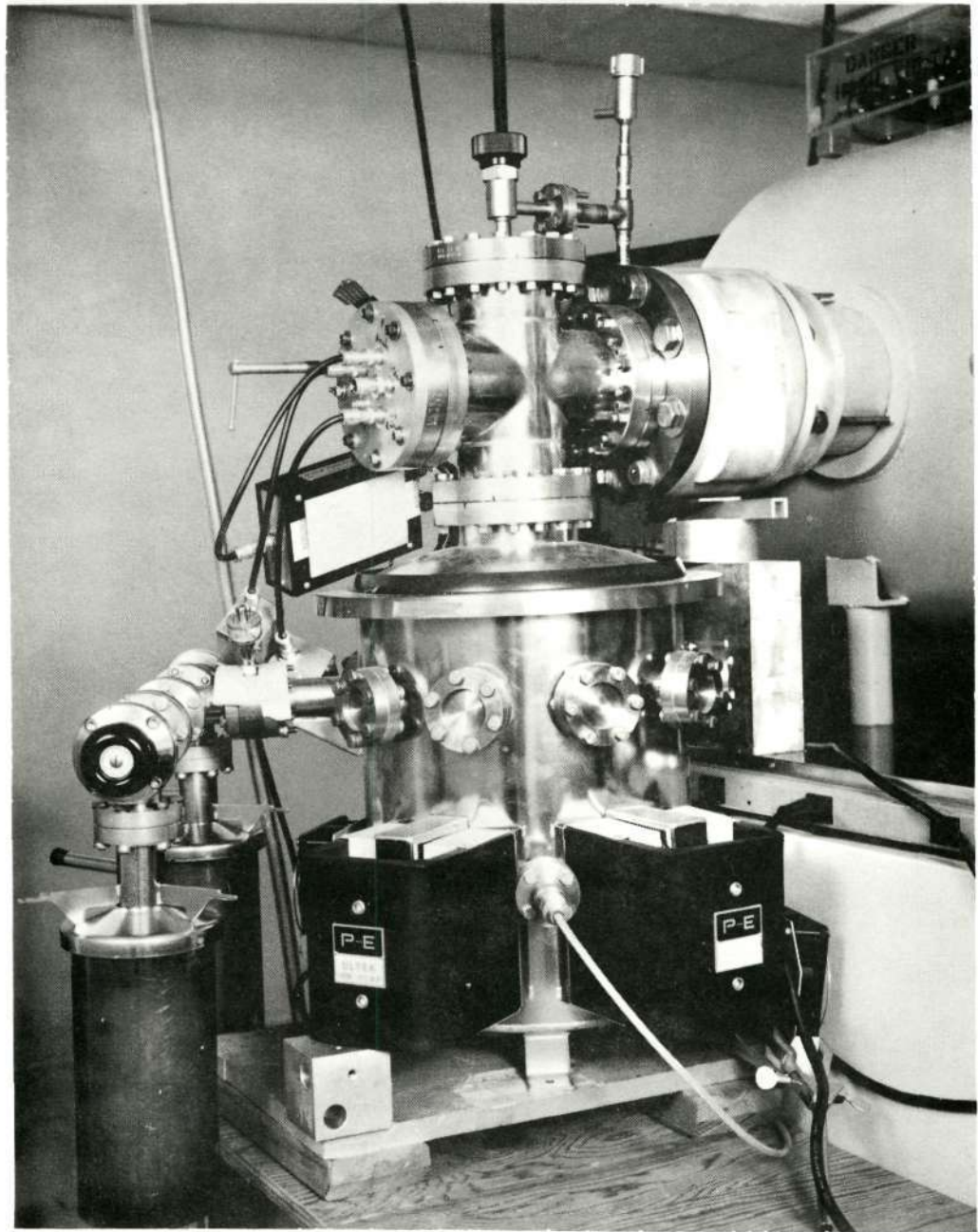
EG-025

Figure 2-3.   Photograph of Ion Pumped Vacuum System.
The MCP is Located near the Center of the
"X" at the Top.

pressure and the ion pump started in under half an hour; it reaches 10^{-8} Torr. The organic window which isolates the detector chamber is sufficiently impermeable so that the pressure does not rise in the detector chamber when the gate valve is opened with the source chamber at 10^{-4} Torr.

An existing diffusion-pumped chamber, which quickly reaches vacuums below 10^{-4} Torr, was modified to house the source in our studies of the response of image intensifiers to X-rays. The source chamber contains a bremsstrahlung X-ray source. A proportional counter, a methane-filled .00012" Mylar window flow counter is used for normalization. In all efficiency measurements, X-rays incident on the MCP traverse the same material as the counter window, so as to reduce uncertainties in calculating the effective transmission for a band of wavelengths.

Proper evaluation of an MCP photocathode requires measurements at several wavelengths so as not to miss the effect of X-ray absorption edges in the cathode material. For this reason a triple target bremsstrahlung X-ray source was constructed which also permitted higher X-ray fluxes for quicker evaluation and changing the X-ray wavelength without opening the vacuum system. Normally targets of aluminum (8.3Å), copper (13.1Å) and carbon (44Å) were utilized although others were available and could be quickly installed. The three targets are mounted side by side in the same plane and are moved into the center position behind the filaments by a rack and pinion (the pinion shaft is turned by a feed through in a vacuum chamber port). Only the target in the center position is connected to the accelerating voltage. This is accomplished by means of a spring loaded contact behind the center position.

Figure 2-4 shows an experimental arrangement for observing the uniformily and spatial resolution of microchannel plates as well as their efficiency and gain. Potentials of the order of 1 Kv are maintained across the MCP while the collecting voltage to the anode is generally 5Kv. With X-rays incident upon the MCP, the output can be recorded in two ways. The light from the phosphor is transmitted by the fiber optic element, collimated by the relay lens and photographed. At the same time the charge pulses at the anode are detected by the charge-sensitive pre-amplifier and stored after amplification and shaping in the pulse height analyzer. Both techniques are used in measuring quantum efficiency, while only the photographic technique provides data on resolution and uniformity and only pulse height analysis gives quantitative information on gain.

The quantum efficiency, gain and noise of microchannel plates are now being obtained electronically from an anode placed in proximity to the output face of the MCP. Figure 2-5 shows the fixture for mounting the MPC for this type of measurement.

The output contact is made by a ring with a shallow depression which locates the MCP. This ring is held at ground potential. Negative high voltage is applied to the input face of the MCP through a spring-loaded contact, which slides inside a fixed locating ring. The springs are placed between the input contact piece and the locating ring; the spring tension can be adjusted by tightening the screws until a predetermined value, as measured by the spring compression is reached. The required contact force is 200-300 grams. Both contact surfaces are polished and flat. The anode is a flat plate 9/16" in diameter, operated at +250 volts. A thin guard ring around the anode is operated at the same potential, but charge pulses in the guard ring are not normally detected.

Figure 2-4. Block diagram of the experimental set up for image intensifier studies. The preamplifier detects charge pulses at the phosphor ultimately producing a spectrum in the pulse height analyzer. The fiber optic output is photographed through the relay lens.
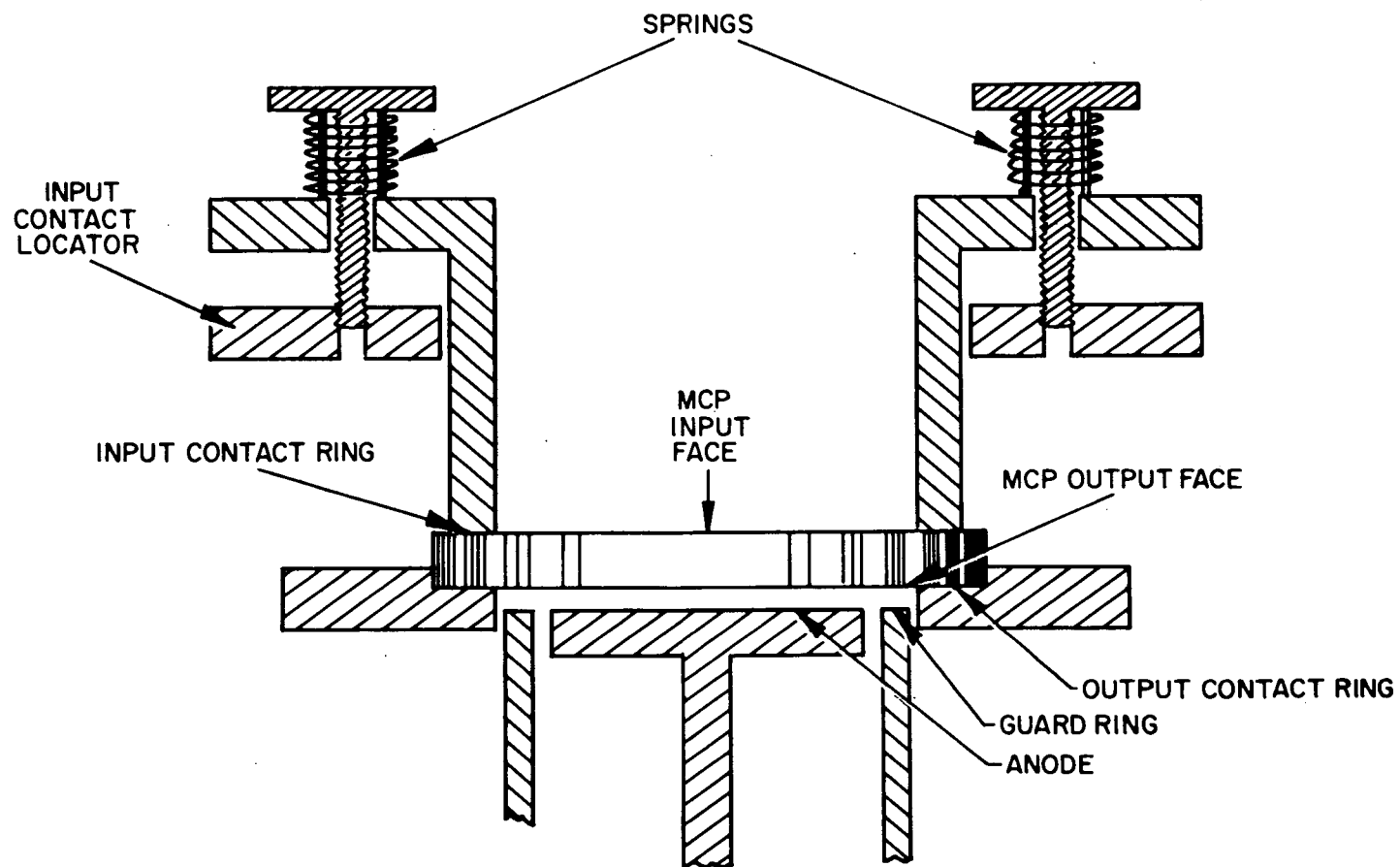
Figure 2-5.   Fixture for testing an MCP.   The input contact ring is spring-loaded and adjusted to give a contact force of 200-300 grams.

Its purpose is to keep electrons generated by contact noise from interferring with the measurements. A block diagram of the electronics is shown in Figure 2-6.

The anode of the MCP receives its bias through an Ortec 109 PC charge-sensitive preamplifier, as shown in the block diagram. The sensitivity of the preamplifier is known so the pulse height spectrum is directly related to the electron yield spectrum from the MCP. (The X-ray intensity is low enough so that each event represents response to a single photon.) The proportional counters are readout by the same type preamplifier. In each case a shaping voltage amplifier is used to produce pulses which can be conveniently handled by the analog-to-digital converters.

The two analog-to-digital converters are interfaced to a NOVA minicomputer which allows simultaneous storage of the two spectra. These spectra can be acquired while a previously acquired set is reduced. One program locates the half-heights of the near gaussian proportional counter spectrum and integrates between them by the trapezoidal rule (including the fractional channels at each end). This sum is divided by 0.761 to give the gaussian equivalent area as a standard. As a check the total counts in the spectrum are also integrated by the computer.

In the case of the microchannel plate the computer reduces the observed spectra from the microchannel plates to two parameters-- their area (quantum efficiency) and the decay constant of their shape (gain). To accomplish this the computer performs a least squares fit to the data it has collected through the analog-to-digital converter (usually after a noise spectrum has been subtracted). The program which utilizes the NOVA's floating point interpreter is documented in the Appendix A. The program actually performs a _weighted_ least squares fit to an exponential because in some
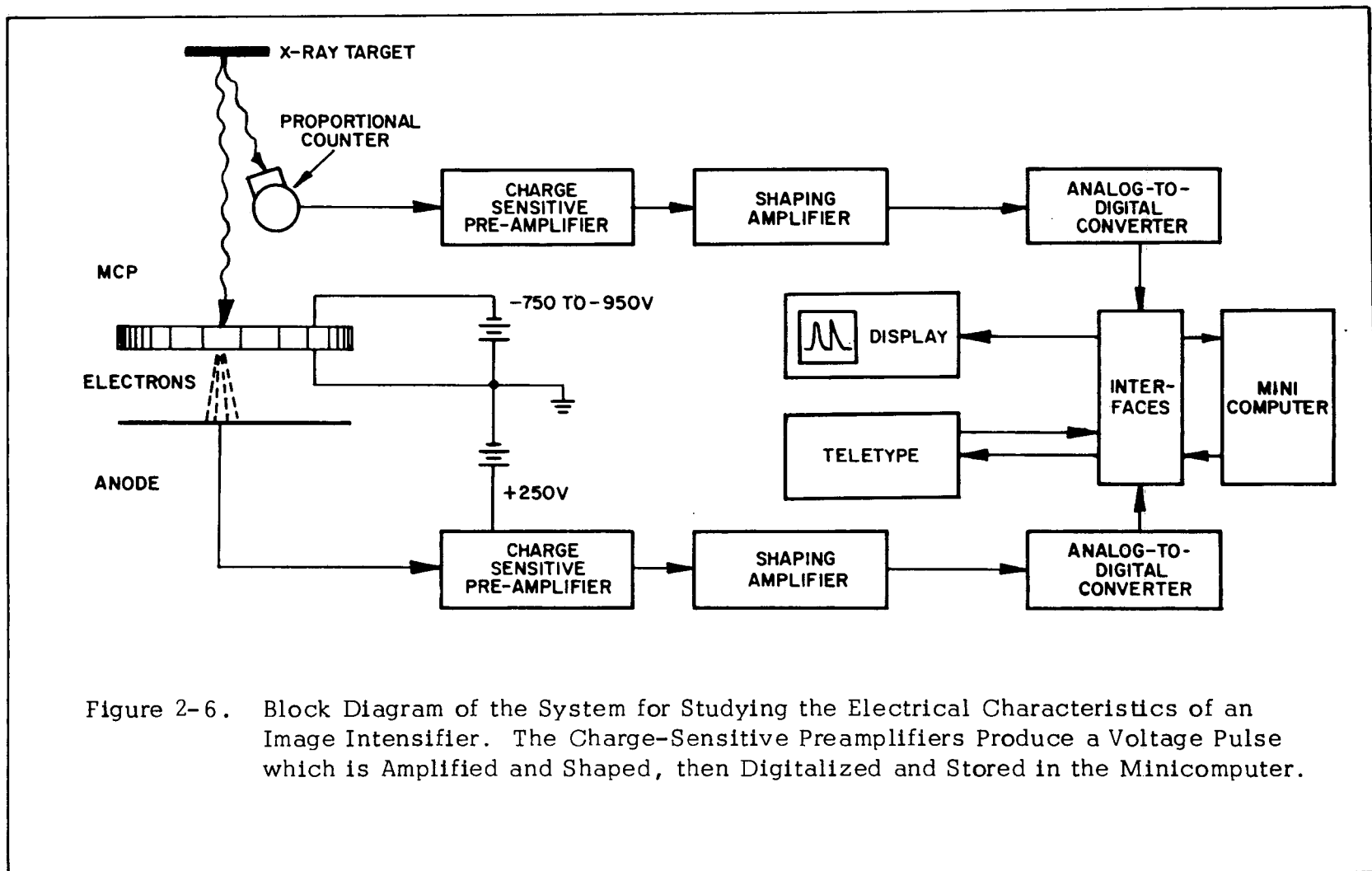
Figure 2-6. Block Diagram of the System for Studying the Electrical Characteristics of an Image Intensifier. The Charge-Sensitive Preamplifiers Produce a Voltage Pulse which is Amplified and Shaped, then Digitalized and Stored in the Minicomputer.

cases the spectra are not quite of exponential shape and failure to weight will result in gross errors brought about by the small number of counts at the high energy end of the spectra.

Figure 2-7 shows the results of such a least squares fit where the straight line is the calculated exponential.

2.2 Microchannel Plate Performance Characteristics

Figure 2-8 shows the spectra observed with a Varian microchannel plate when irradiated by Al(k) X-rays from the bremsstrahlung X-ray source, and filtered by a 1/4 mil aluminum foil.

The physical charactersite of this MCP are:

Plate O. D.	0.975 inches
L/D (Tubes)	42
Channel Diameter	15μ
Open Area	57%
Channel Spacing	18.8μ center-to-center
Plate Thickness	0.247 inches
Bias	5°

The electron gain and quantum efficiencies associated with the figure are shown in Table I.

TABLE I

V_p	A ℓ (k)(8.3Å)		Cu (L)(13.2Å)		C (k) (44Å)	
	Gain*	QE(%)	Gain*	QE(%)	Gain*	QE(%)
750	5078	2.26	4911	2.71	2252	0.89
800	8944	2.23	8700	2.71	4408	0.85
850	16253	2.26	15608	2.49	7733	0.82
900	25714	2.35	23262	2.71	12038	0.85
950	39299	2.41	37726	2.69	20068	0.78

* Electrons/event
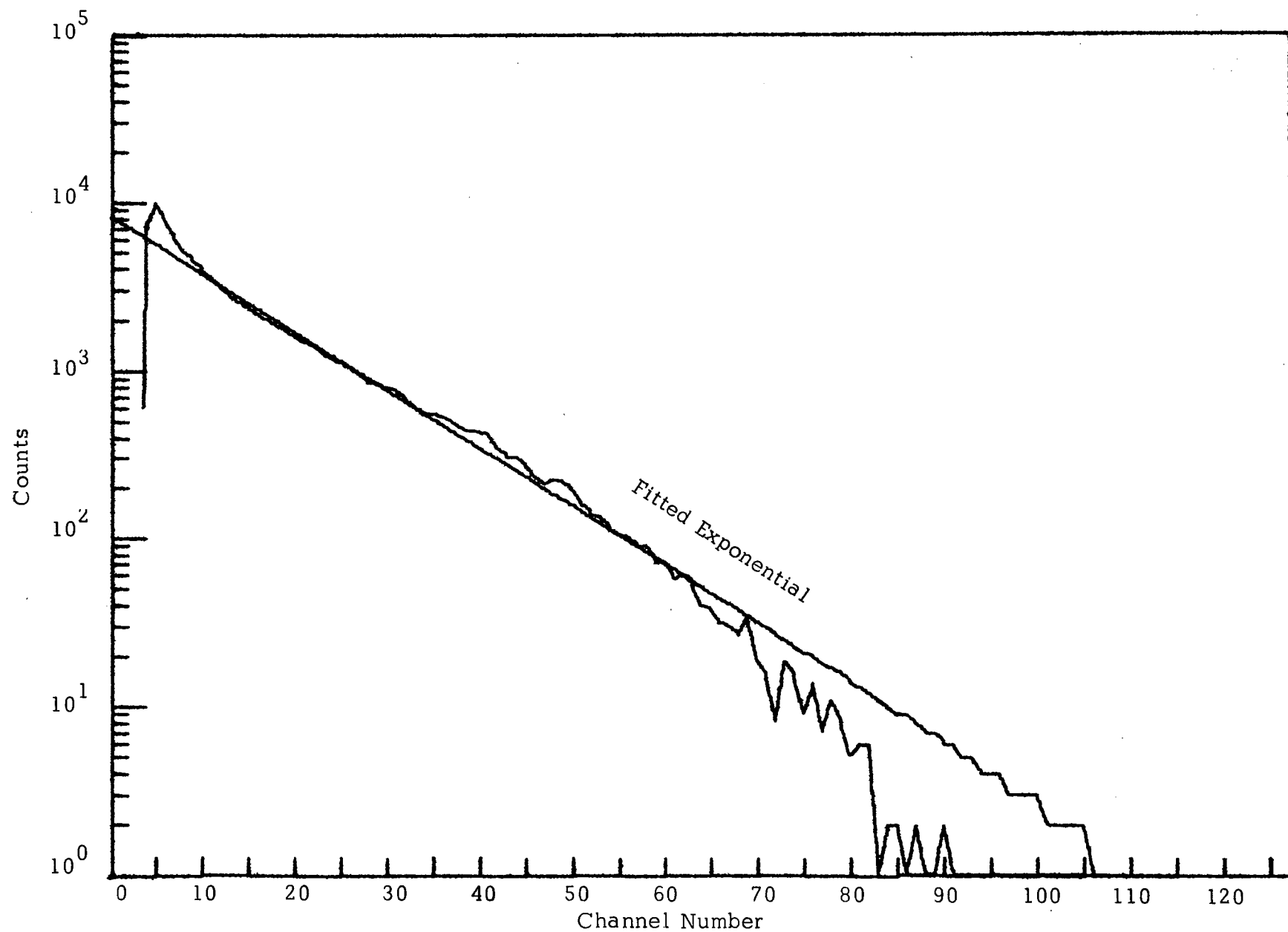
Figure 2-7. Least squares fit of an exponential to a microchannel plate spectrum.
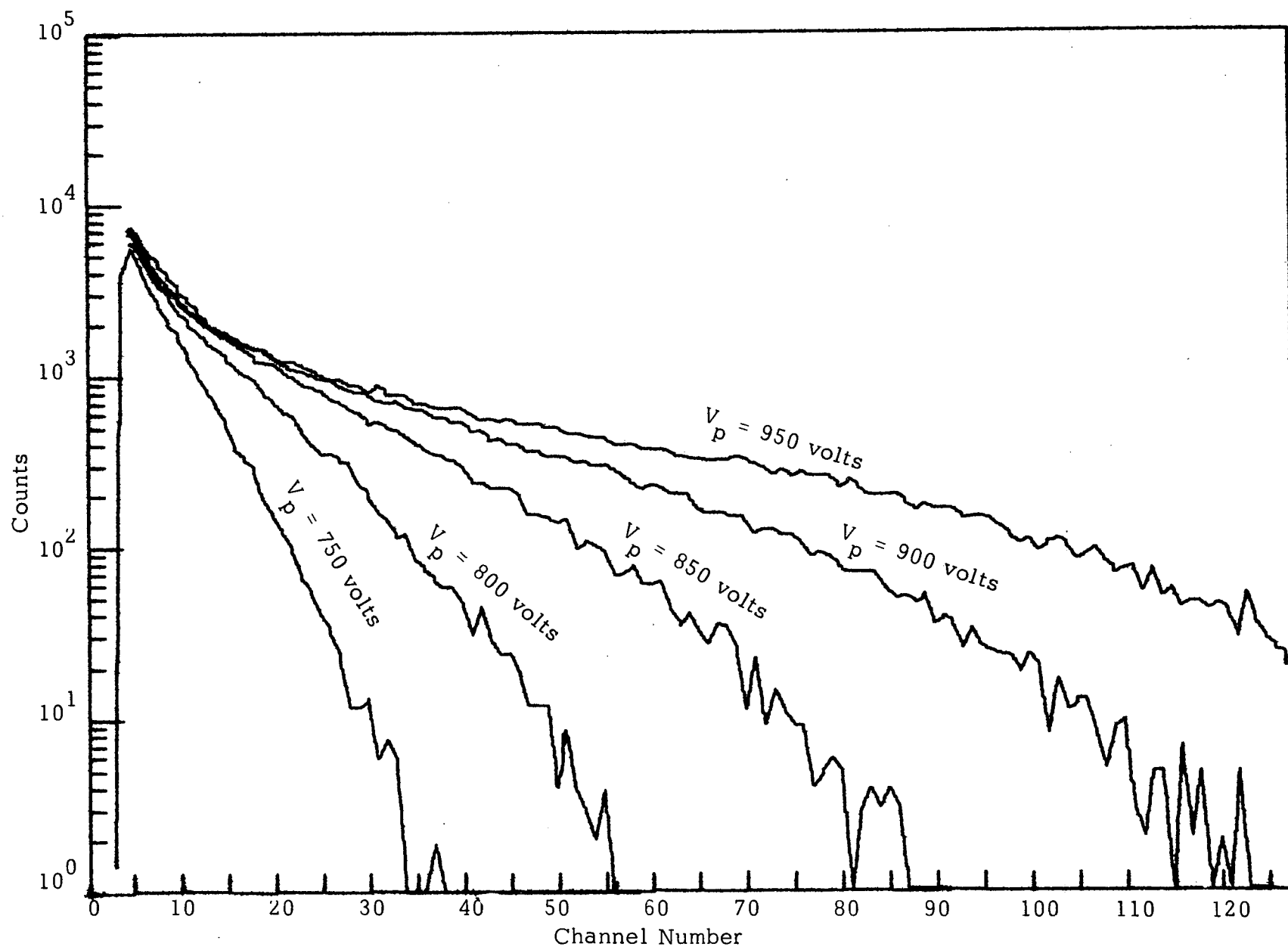
Figure 2-8.   Microchannel plate spectra for various voltages across the plate normalized to incident flux of Al(k) X-rays.

When the exponential portion of the spectra are extrapolated to zero gain (see Figure 2-7) a fairly uniform efficiency vs plate voltage response is noted. The drop in gain and quantum efficiency shown for the carbon X-ray (44Å) in the table above was noted for all MCP's. These Varian MCP's were observed to have extremely low noise while their gain and efficiency were comparable to the Rauland MCP's.

2.3 Coating of Microchannel Plates

The concept of coating microchannel plates by vacuum deposition with materials with high secondary electron emission characteristics is attractive, especially if such increased performance can be obtained without significantly increasing the noise. We have coated MCP's with LiF, MgO and MgF_2 in such a study. We have attempted to coat only the input face and in such a manner as to coat into the channels to a depth of 300Å. The plates have been rotated about an axis parallel to the channel axis in order to accomplish this.

To date the results have not been promising. For the most part there has been a slight increase in noise and a slight reduction in gain and quantum efficiency. Table II shows the post coating (MgF_2) performance of the MCP whose performance was noted in Table I.

TABLE II

	Aℓ	(k)(8.3Å)	Cu	(L)(13.2Å)	C	(k) (44Å)
Volts	Gain*	QE(%)	Gain*	QE(%)	Gain*	QE(%)
750	4124	2.95	3596	4.25	2242	0.89
800	7411	2.66	6109	3.81	4884	0.68
850	15170	1.96	14049	2.28	6805	0.97
900	24385	1.96	22671	2.27	11741	0.90
950	34800	2.23	33807	2.49	17155	1.02

*Electrons/event

An increase in the noise was noted following coating (care was taken to avoid coating the contact areas).

2.4   Space Qualification

To qualify for an extended mission like HEAO-C the image intensifier must demonstrate:

a) that it is not too delicate to survive its expected pre-launch treatment and the shock and vibration of launch.

b) that it can operate continuously in high vacuum for a year.

c) that its count life exceeds the number of counts expected during the mission.

We have two image intensifiers that have had considerable use over a period of a year. The unit shown in Figure 2-1 has received particularly rough treatment. It was launched in an Aerobee 150 sounding rocket on February 6, 1970. Due to a vacuum failure, it was turned on in an ambient pressure in the corona region, and broke down. After the flight it was still operable, but had less gain than previously. Its gain was restored to more than the originally measured value by simply increasing the potential across the MCP, and the same unit was flown in an Aerobee 170 sounding rocket on September 28, 1970. This unit has now experienced two launches, at least twenty vibration tests at Aerobee levels, nine airplane flights, numerous vacuum cycles and a year of laboratory use and storage. It still worked well when last checked; its performance history is depicted in Figure 2-9. The unit shown in Figure 3-1 has been used occasionally over a period of about a year. It sat on a laboratory bench at atmospheric pressure for four months--a storage technique not recommended by the manufacturer--and has been exposed to a vacuum failure while turned on. Its performance was still good at the time

2-15

SENSITIVITY HISTORY, MCP UNIT No.7
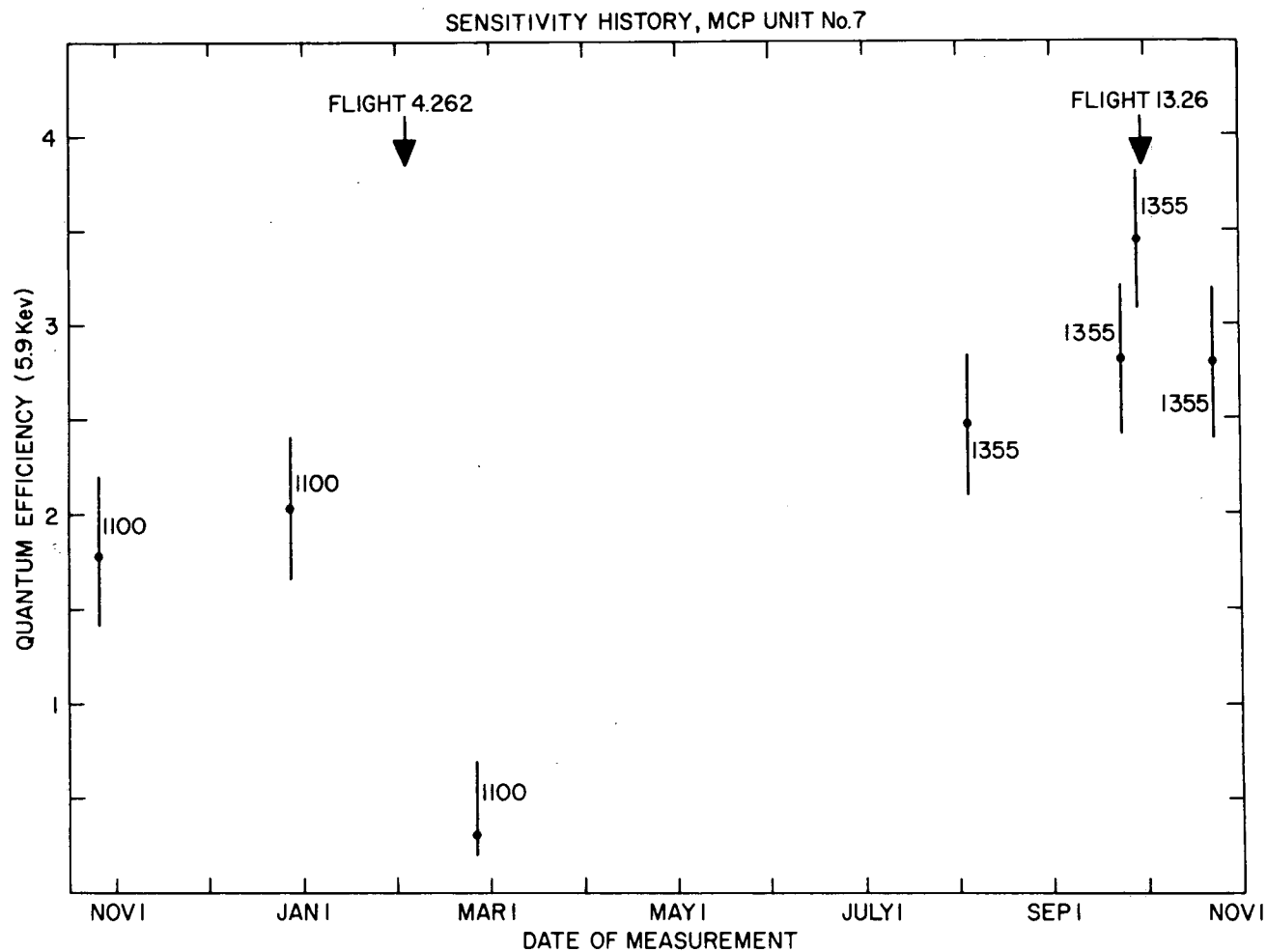
Figure 2-9. History of the quantum efficiency of an image intensifier. Although the unit lost gain because of an accidental exposure to poor vacuum during operation, the performance was easily restored by increasing the potential across the MCP.

of its last testing. Far from being delicate, X-ray image intensifiers appear able to absorb substantially more punishment than a flight unit is likely to sustain.

We are measuring the lifetime in high vacuum, using the facility shown in Figure 2-10. The ion pump with titanium sublimation well and sorption roughing hold the image intensifiers in vacuum below 10^{-8} Torr. We find that this vacuum can be maintained by running the titanium filaments for as little as 45 seconds per month. The ^{55}Fe source shines X-rays on the MCP at a rate comparable to the expected rate on HEAO-C. The potential is kept continuously on the MCP. The source can be rotated so as not to irradiate the MCP during background measurements. The electron yield spectra are recorded frequently.

To date each has had more than 10^{10} quanta incident upon it. The data was reduced using the MCP evaluation program discussed in Section 2.1. Earlier readouts were punched into the NOVA computer by hand so that all data would be subjected to a standardized method of analysis. The computer also subtracted the no-source spectra from those taken with the source. Alignment of the different analog-to-digital converters involved was achieved by use of pulse generators.

The plate which was initially noisy (designated MCP #1) has quieted down and is now performing usefully. However, as Figure 2-11 shows it is still too early to determine any trends in its performance. Figure 2-12 shows the performance of MCP #2 under this test. The quantum efficiency has not been corrected for the decay of the ^{55}Fe source but the source decay exponential (2.7 years) has been plotted in the figure for comparison with an expontial fitted by least squares to the "good" points. The discrepancy between the two exponentials is within the accuracy of
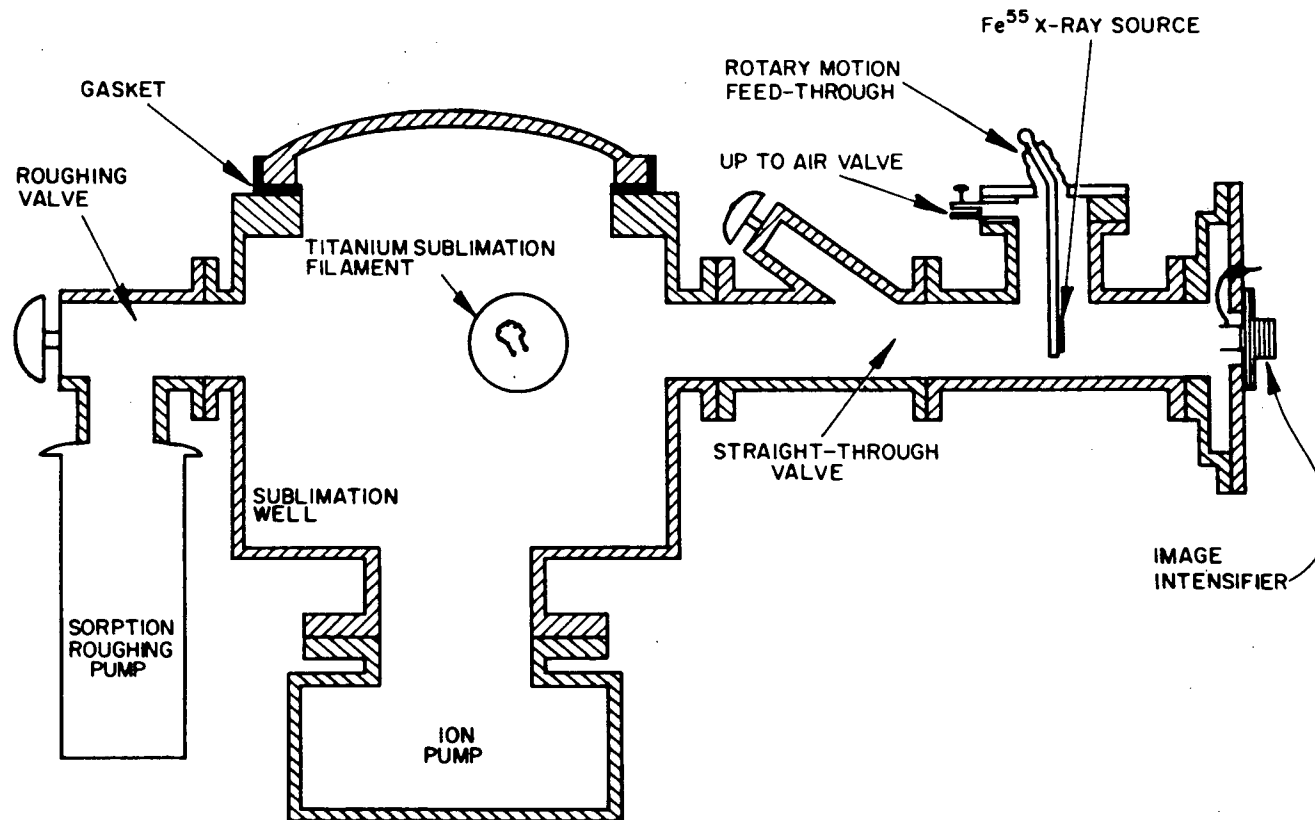
Figure 2-10. Facility for study of the long term effect of operation in high vacuum. Rotating the Fe^{55} source allows background measurements to be made.
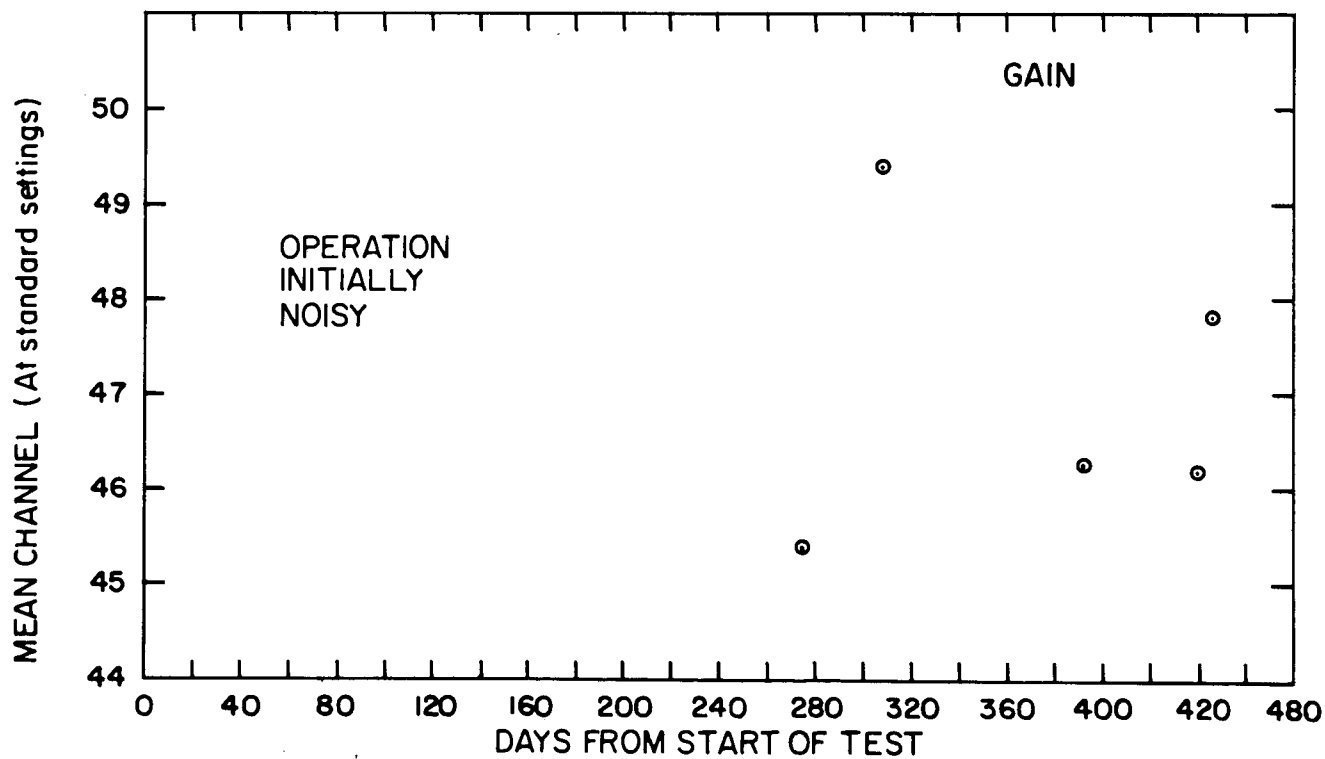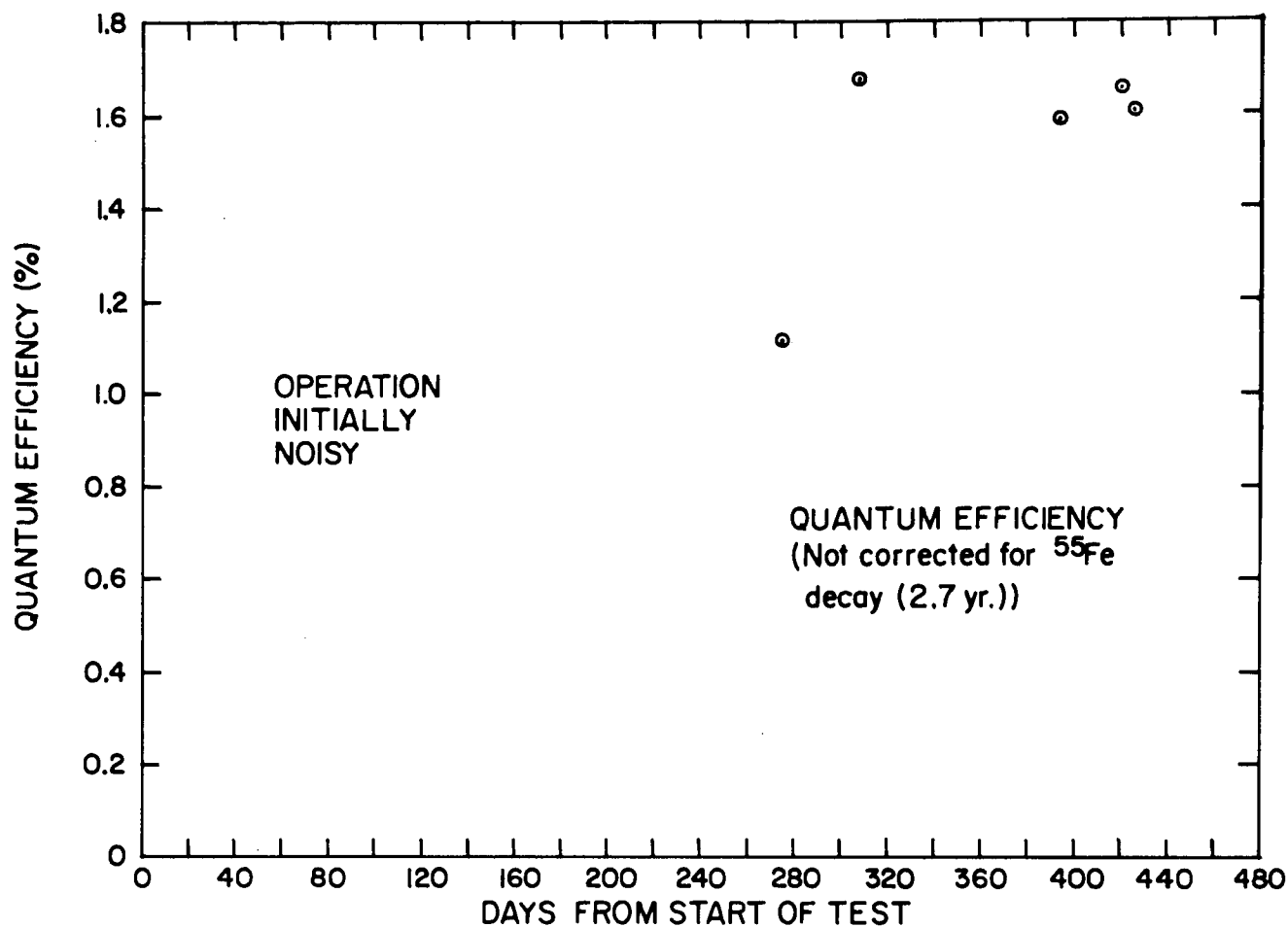
Figure 2-11. Life Test Performance of MCP No. 1
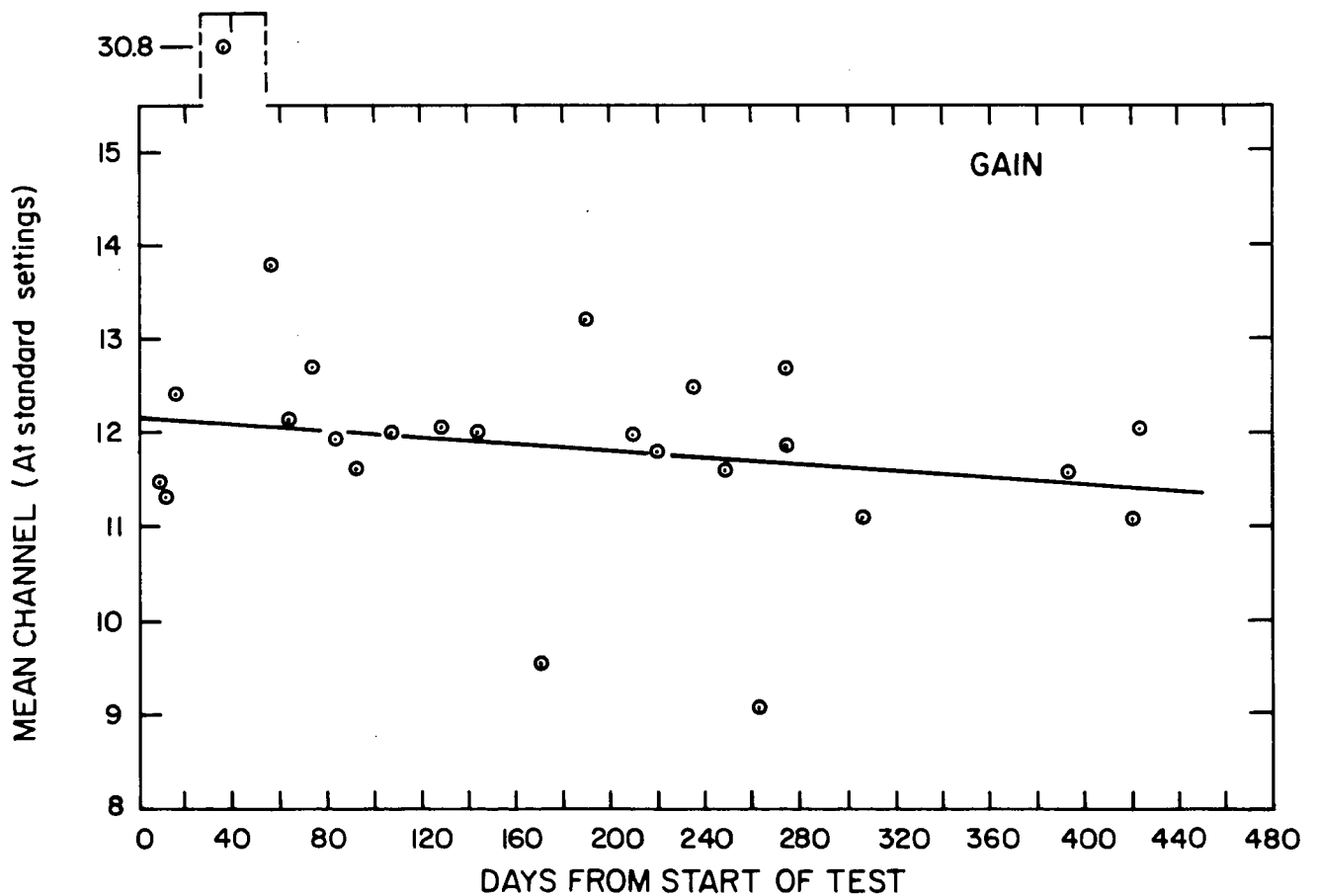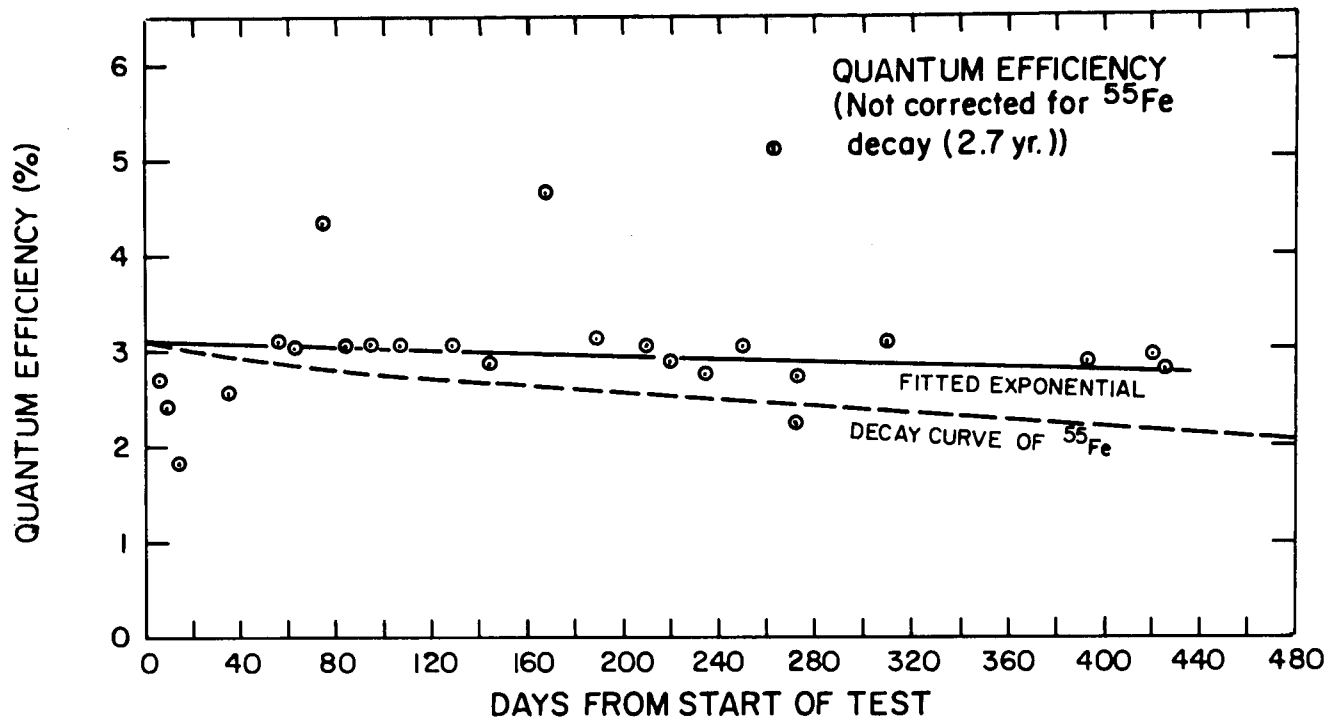
Figure 2-12.   Life Test Performance of MCP No. 2

the measurement when the short term noise fluctuations involved
are considered. Fitting the "good" points of the gain with a
straight line now seems to produce a slight downward slope.
The slope of the fitted line is about -5% per year of the original
gain and the true value can safely be assumed to be less than
10%.

The noise observed in these tests has been reduced by AS&E's
move to its new building and by grounding the back of the pre-
amplifier to the vacuum system by means of a braided strap. It
is significant that the noisy MCP has become useful again and
that the one which has permited exact observations has proven
itself useful for extended missions.

An MCP was operated in the fixture shown in Figure 2-5, to
measure the count life. An aluminum anode bremsstrahlung
generator with a coiled tungsten filament is providing a high in-
tensity beam; the count rate is about 5×10^6 persecond. Periodic
measurements of the gain and QE for detection of ^{55}Fe X-rays
have shown no degradation in performance as can be seen from
Figure 2-13. The total of counts expected on HEAO-C was far
exceeded.

2.5 Evaluation of Chevron Microchannel Plate

A Bendix A3050X Chevron type microchannel plate assembly was
obtained. This type of assembly has superior gain characteristic
over a single plate because the electron multiplication can be
greatly increased without severe ion feedback. Pertinent
characteristics of this chevron plate assembly are as follows:

Electron gain at 2800V	1×10^7
Nominal resolution	5 line pairs/mm
Max. output current/cm^2	$10^{-6} A/cm^2$
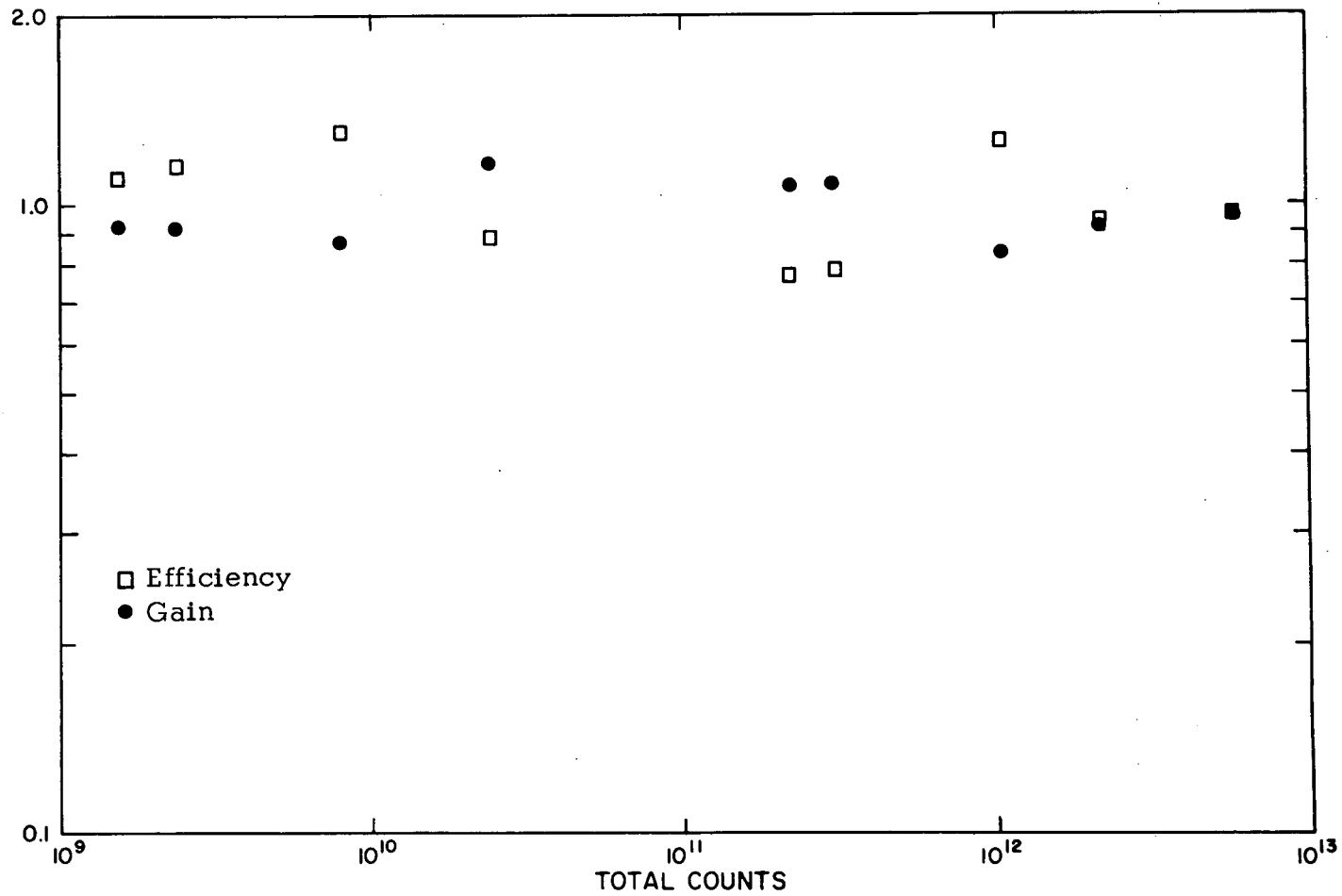
Figure 2-13. The QE and gain of an MCP subjected to many more total counts than would be expected during the life of HEAO-C. The normalization is arbitrary.

Max. recommended count rate at 1×10^7 gain 10^6 counts/sec-cm^2

Channel to channel center spacing   53 μm

Nominal active area diameter   40 mm

Preliminary testing of the chevron plate assembly using a solid anode indicates a gain increase by an approximate factor of 60 over that for the typical single microchannel plate evaluated in this program when the chevron plate assembly was operated at 2000V (1,000V across each plate). The gain became significantly higher when operated at the rated 2,800 volts but the noise also increased significantly (this may be to problems in the support and wiring assembly).

Its quantum efficiency at 2,000V was observed to be roughly 5% for the 1.49 keV Al K X-rays.

A digital table was employed in a vacuum system to rotate this device about an axis which would align the 15° biased channels with the incident X-ray beam. The resulting efficiency curve (Figure 2-14) showed a peak at 10° rotation from the surface of the plate perpendicular to the beam with a rapid drop off at greater angles. However, during the course of these measurements the device became extremely noisy and eventually useless. This situation particularly effects the readings made at higher angles and calls them into question. These measurements were performed after the wire readout studies noted in Section 3.2 but using the same vacuum system. This system was oil pumped and not trapped. An examination of this chevron microchannel plate by the manufacturer revealed no apparent physical damage thereby strengthening the assumption that its failure was due to an oil coating.

Figure 2-14.   Quantum Efficiency of Bendix
Chevron Microchannel Plate
Al (k) X-Rays
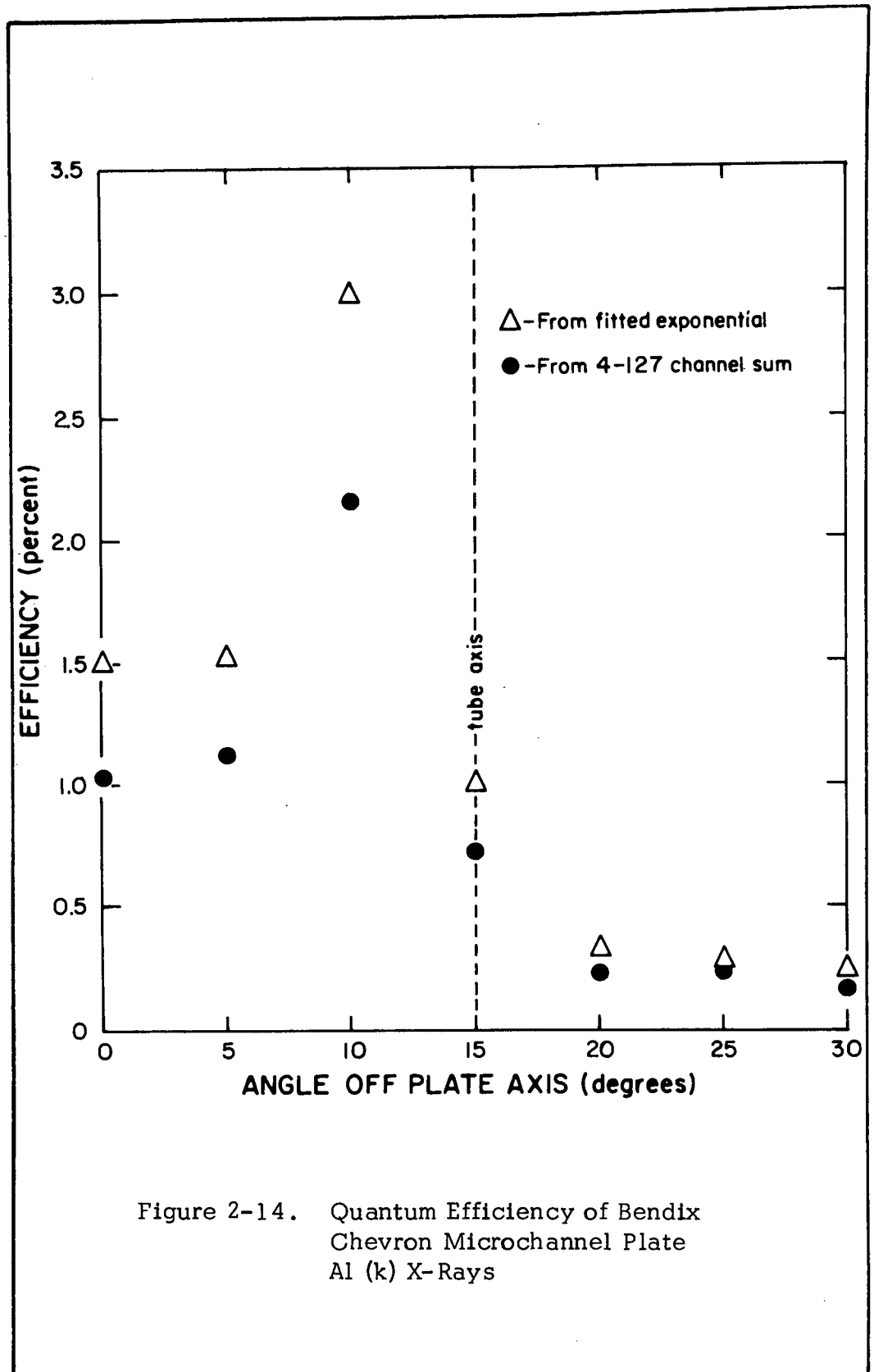
3.0 IMAGING MCP OUTPUTS

Two methods of obtaining positional information from microchannel plates were studied: the use of a phosphor viewed by a low light level vidicon and a wire array readout by charge division and interpreted by a minicomputer. The latter system has the advantage of operating in a single photon mode whose ideal readout system would determine only the position of single counts rather than scanning the entire field. In addition, pulsed sources could be studied more closely with a system which tagged each event with its time of arrival rather than scanning at regular intervals.

3.1 Video Viewing of MCP Phosphor Outputs

A video system has also been assembled for observing the output of an image intensifier inside a vacuum chamber. A Secondary Electron Conduction (SEC) vidicon is mounted in an airtight container, viewing the fiber optic face of the image intensifier through a relay lens, as shown in Figure 3-1. The container can maintain the vidicon in an atmospheric pressure environment for days. A SONY AV-3600 video tape recorder has been procured, and is used for recording the video output.

The image intensifier-vidicon system was used in AS&E's large chamber at the end of the 200 foot X-ray tube, (Figure 3-2) to record the response of a grazing incidence telescope. The ATM engineering model telescope, a two element paraboloid-hyperboloid configuration with an 84 inch focal length, was illuminated with X-rays from the microfocus source. The image intensifier could be translated relative to the telescope for focusing, and the entire arrangement could be rotated. Figure 3-2 shows the experimental set-up.
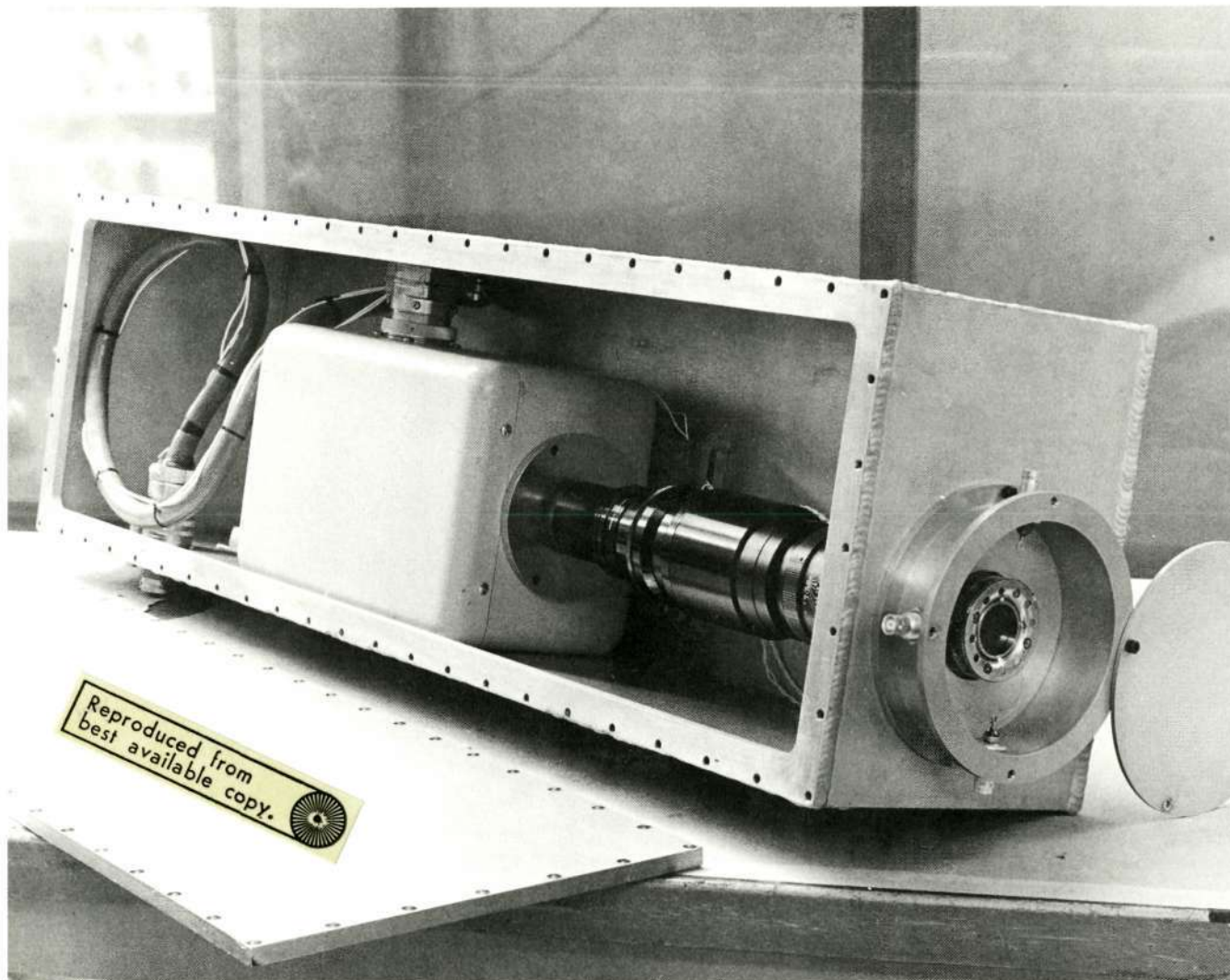
CL-557

Figure 3-1   The Image Intensifier-Vidicon System Currently in Use at AS&E.
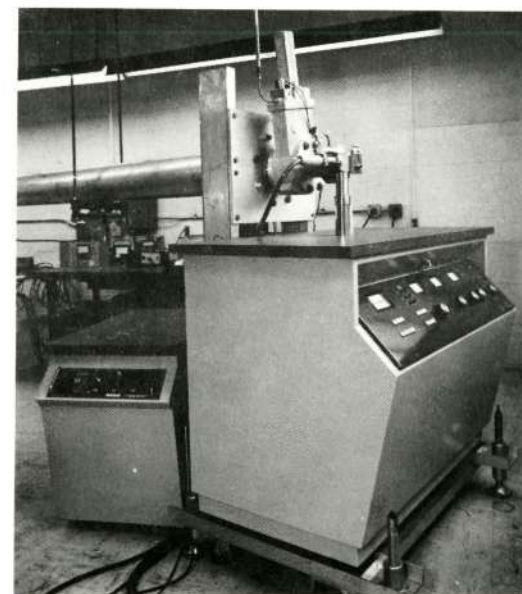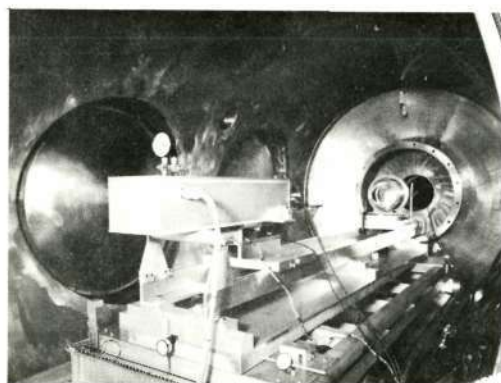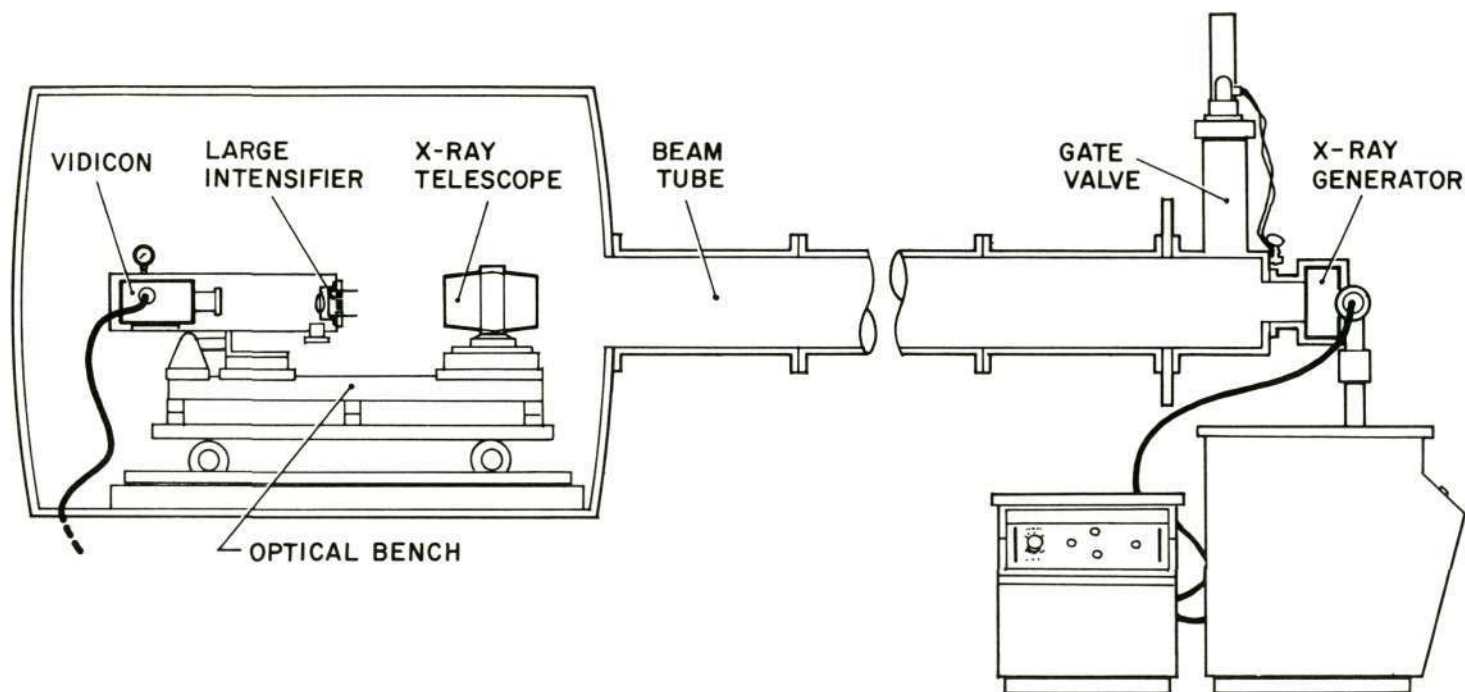
Figure 3-2 The 220 foot X-ray beam tube facility. X-rays produced by the
microfocus source, right, are transmitted by the beam tube to
the large chamber, left. The X-ray telescope focusses the
X-rays onto the MCP, and the vidicon records the output of the
image intensifier.

Figure 3-3a shows the video picture when the input face of the MCP
is .25 inches from the focal plane of the telescope. The familiar
ring pattern is observed. In Figure 3-3b, the MCP has been moved
to the focal plane, and the image is sharp. The pictures were
produced with 2:1 magnification in the relay lens system.

3.2   Wire Array Readout of Chevron Microchannel Plate
A wire array readout assembly was constructed to evaluate the
positional information that can be obtained from the chevron plate
by non-video means. This type of system offers data compaction
advantages over a video system. A block diagram of the system
is shown in Figure 3-4. The system was digitalized as much as
possible to permit greater flexibility and to overcome the problems
of constructing and aligning the analog circuits which would
otherwise be required to perform the arithmetic required to deter-
mine the position of the X-ray. Figure 3-5 shows the NOVA
computer and other electronics required for this measurement.
In this operation two ADC's are interfaced to the computer through
the accumulators. The ADC's digitalize signals from opposite ends
of the parallel array of wires. The wires are connected by cap-
acitors which provide a uniform impedance across the array. Thus,
the distance from one end of the array is proportional to $h_r/(h_r + h_\ell)$
where h_r and h_ℓ are the pulse heights observed at the right and
left sides of the array. The computer performs this arithmetic and
uses the result as an address to increment a memory location.
Details of the chevron plate mounting and the wire array are
shown in Figure 3-6. These wires were 4 mil tungsten wound
under tension on ceramic block with 5 mil grooves on 10 mil
centers. Only the 20 center wires were brought to the charge
divider which consisted of 100 pf capacitors. The wires were
also grounded through 1 meg ohm resistors. The remaining eighty
were simply grounded for this test.
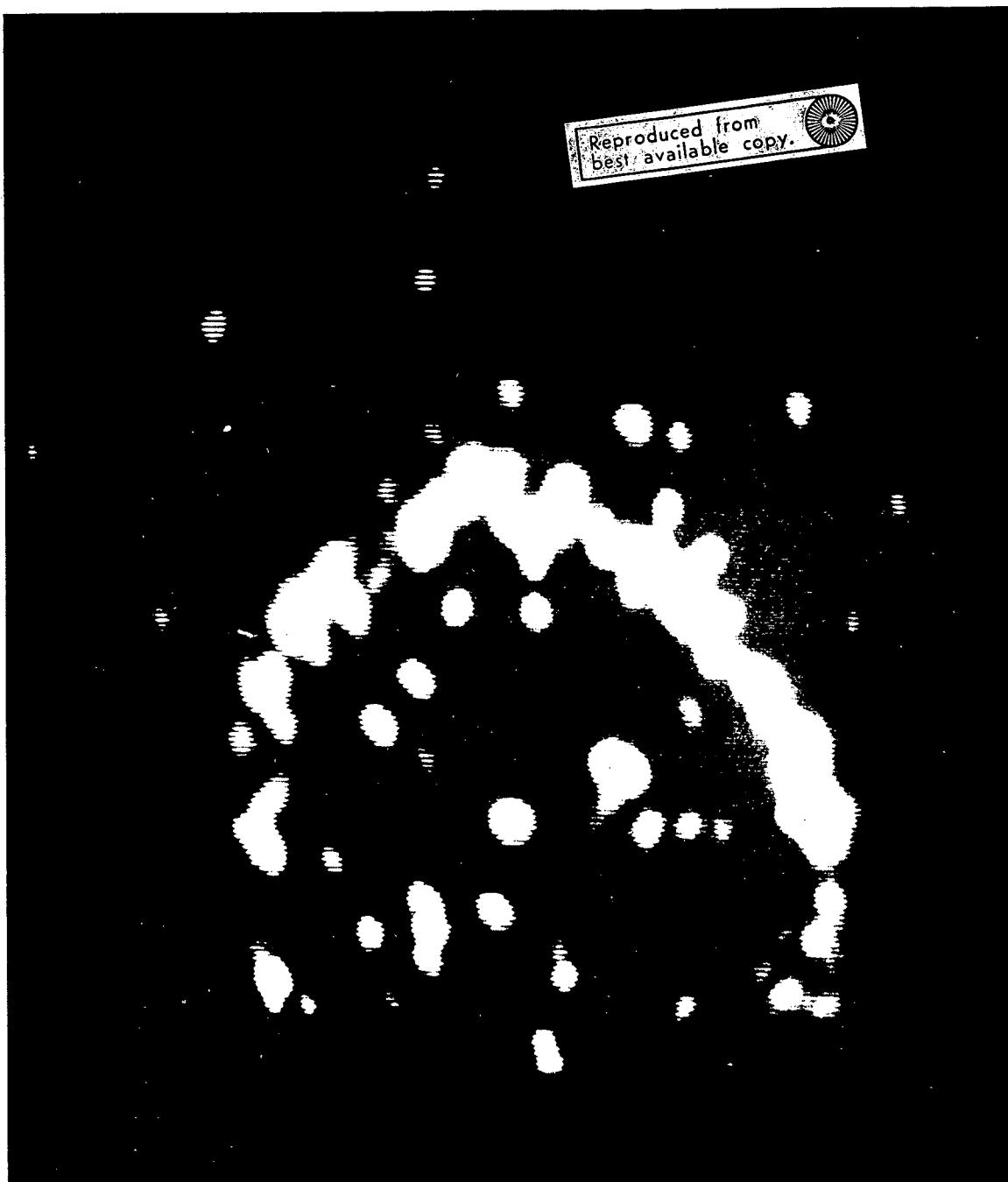
Figure 3-3a   Video picture of the fiber optic output of an image
intensifier.   The MCP is .25 inches from the focal
plane of the telescope producing a ring-shaped image.
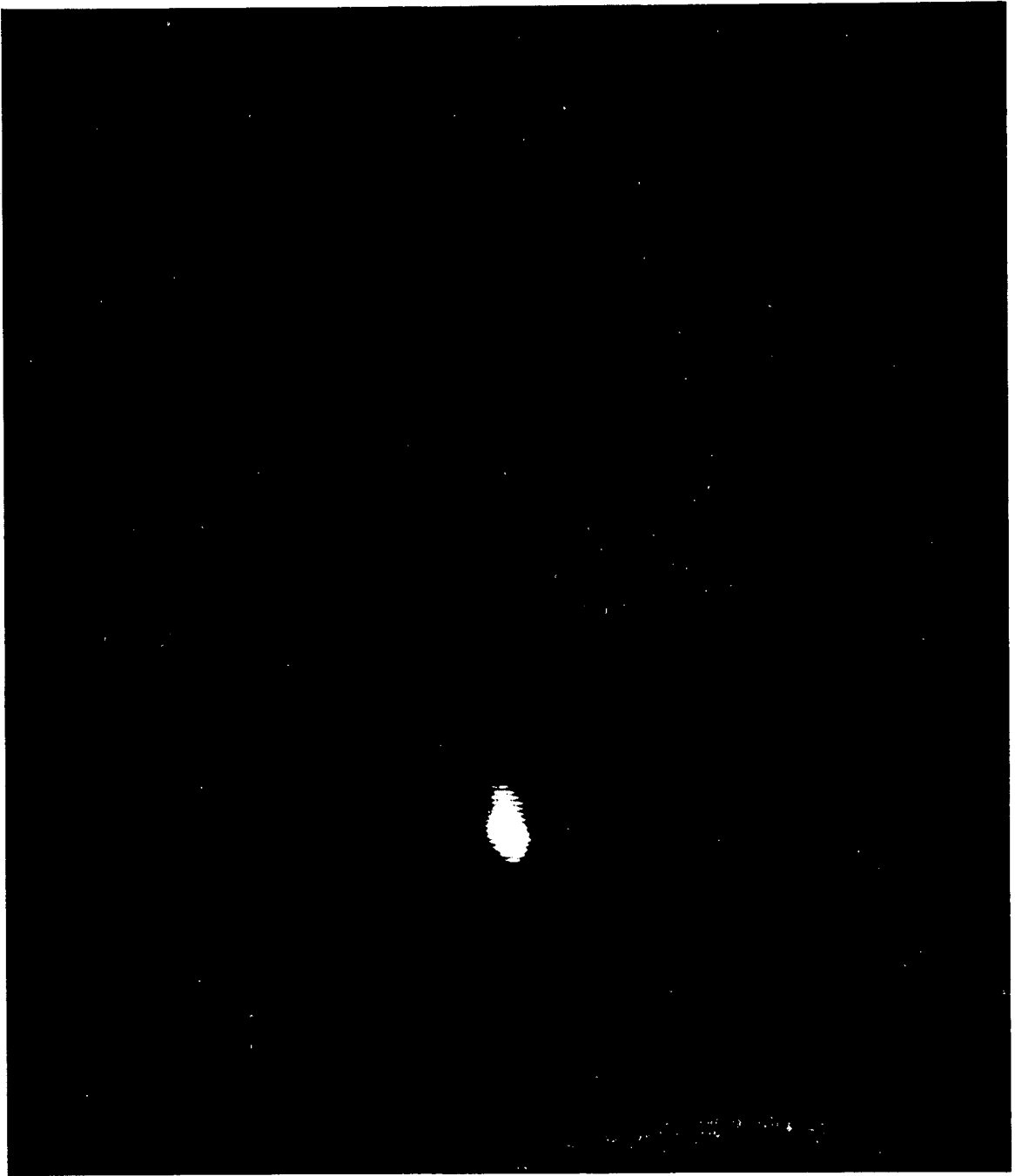
Figure 3-3b Video picture of the fiber optic output of an image
            intensifier. The MCP is the focal plane and the
            image is sharp.
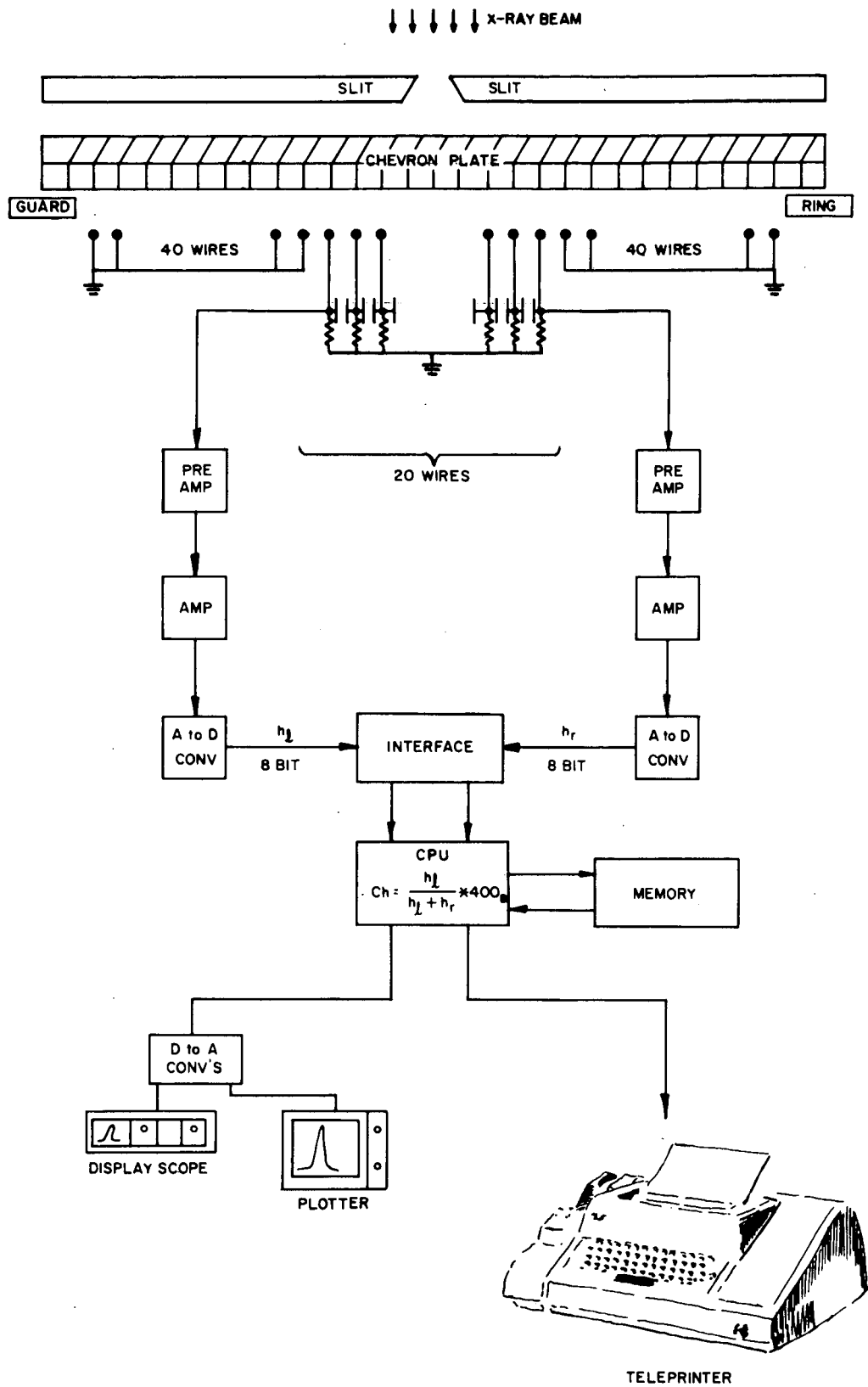
Figure 3-4. Block Diagram of System for Wire
Array Readout of Chevron Plate
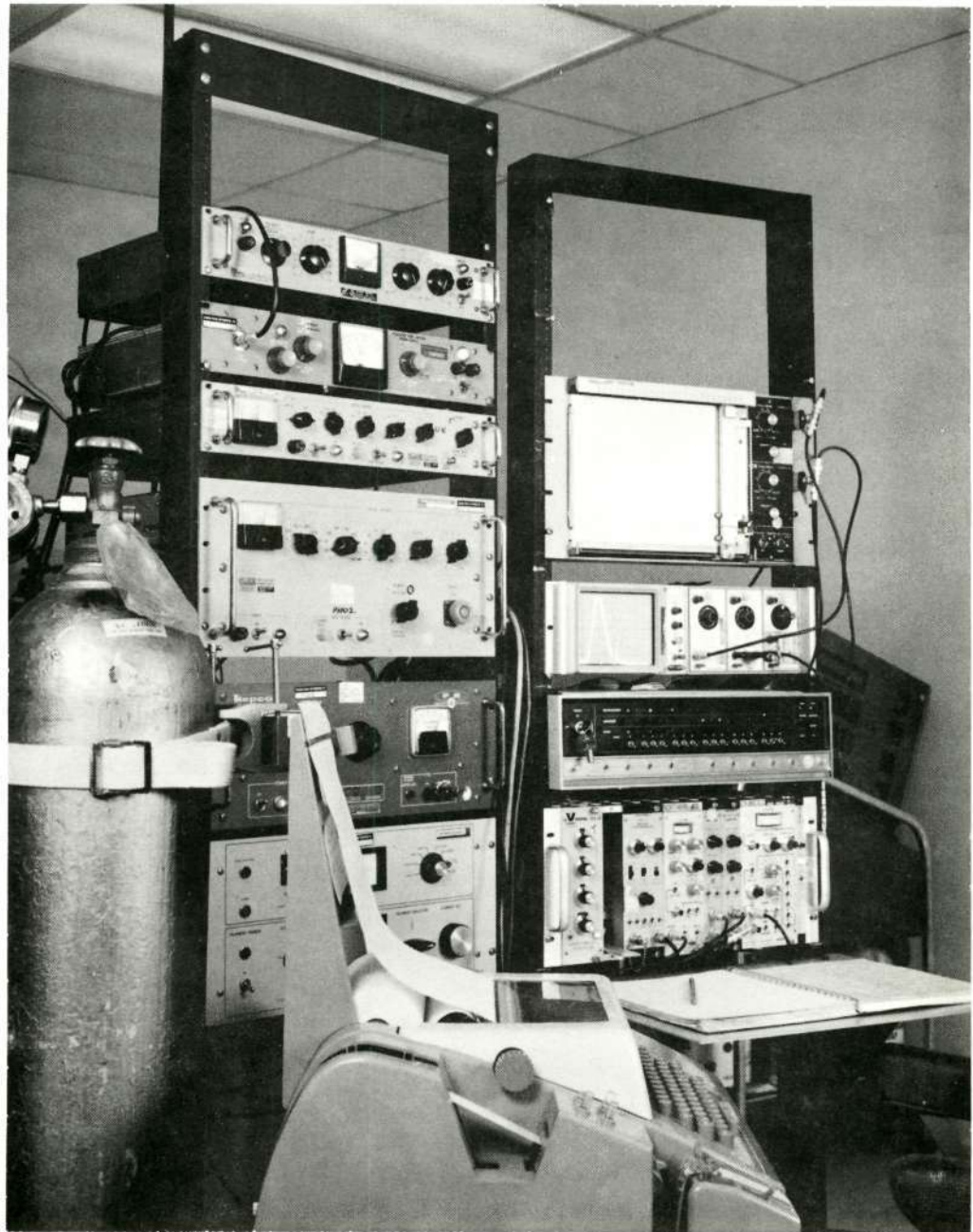
EG-023

Figure 3-5.   Photograph of Electronics for Wire Array
Readout. The Minicomputer, Amplifiers,
ADC's and Display are in the Rack at the
Right. The Rack on the Left Contains
Power Supplies.

| INCHES | 1| | | | 2| | | | 3| | | | 4| | | | 5| | | | 6|

AS&E
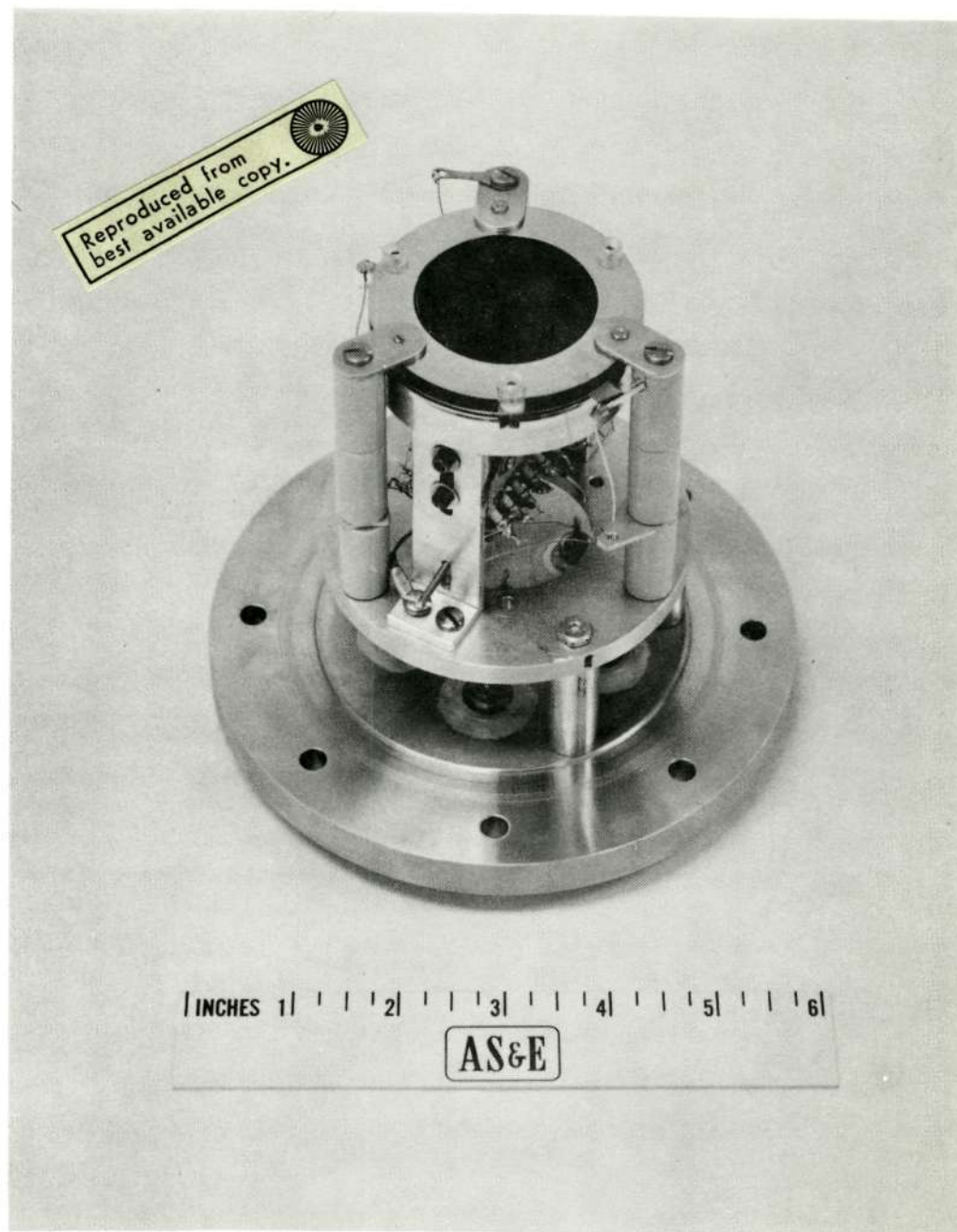
EG-022

Figure 3-6a.   Views of Chevron Microchannel Plate with
Wire Array (Complete Assembly)
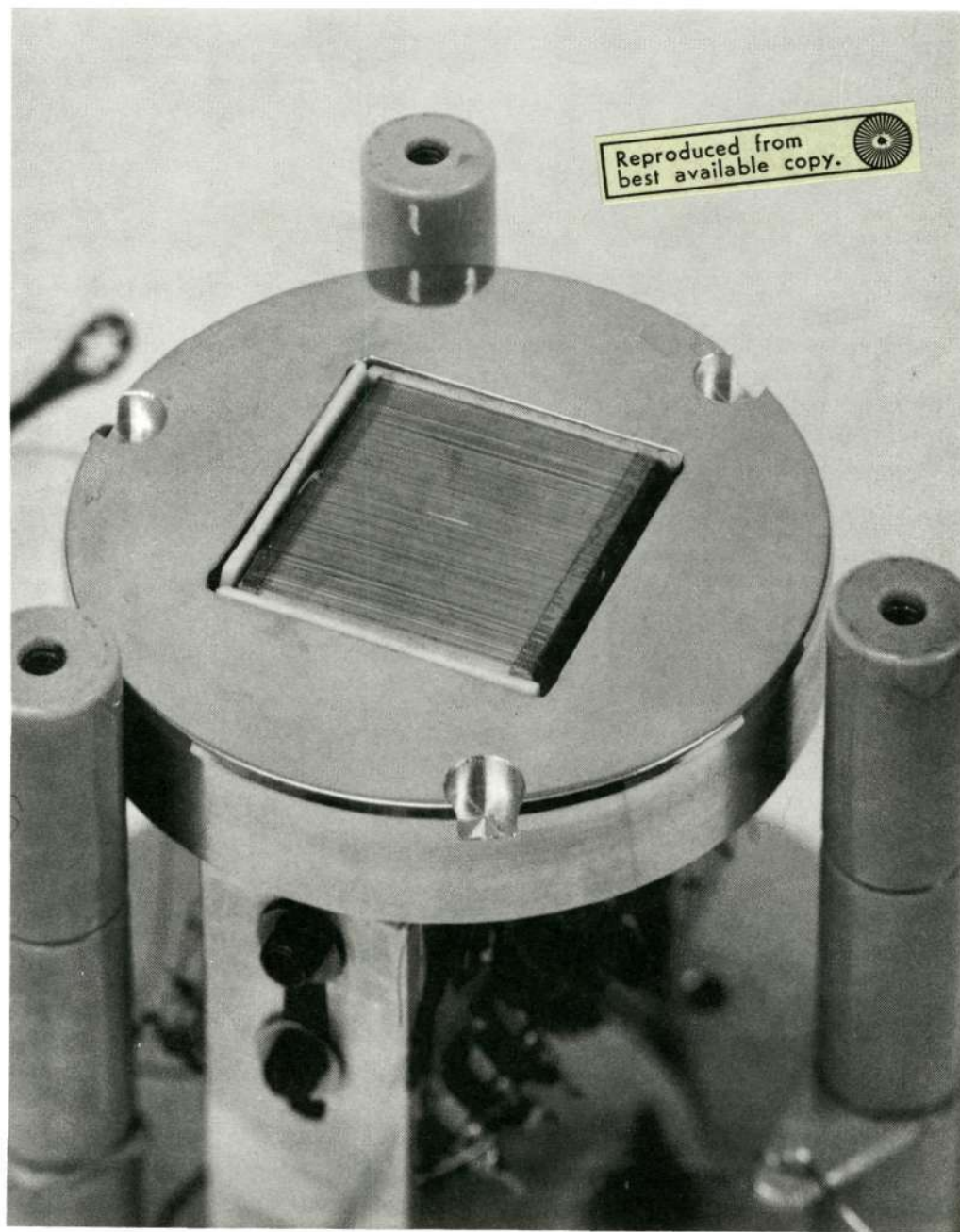
EG-021

Figure 3-6b.   Views of Chevron Microchannel Plate with Wire
Array (With Chevron Plate Removed Showing
Wire Array and Guard Ring)
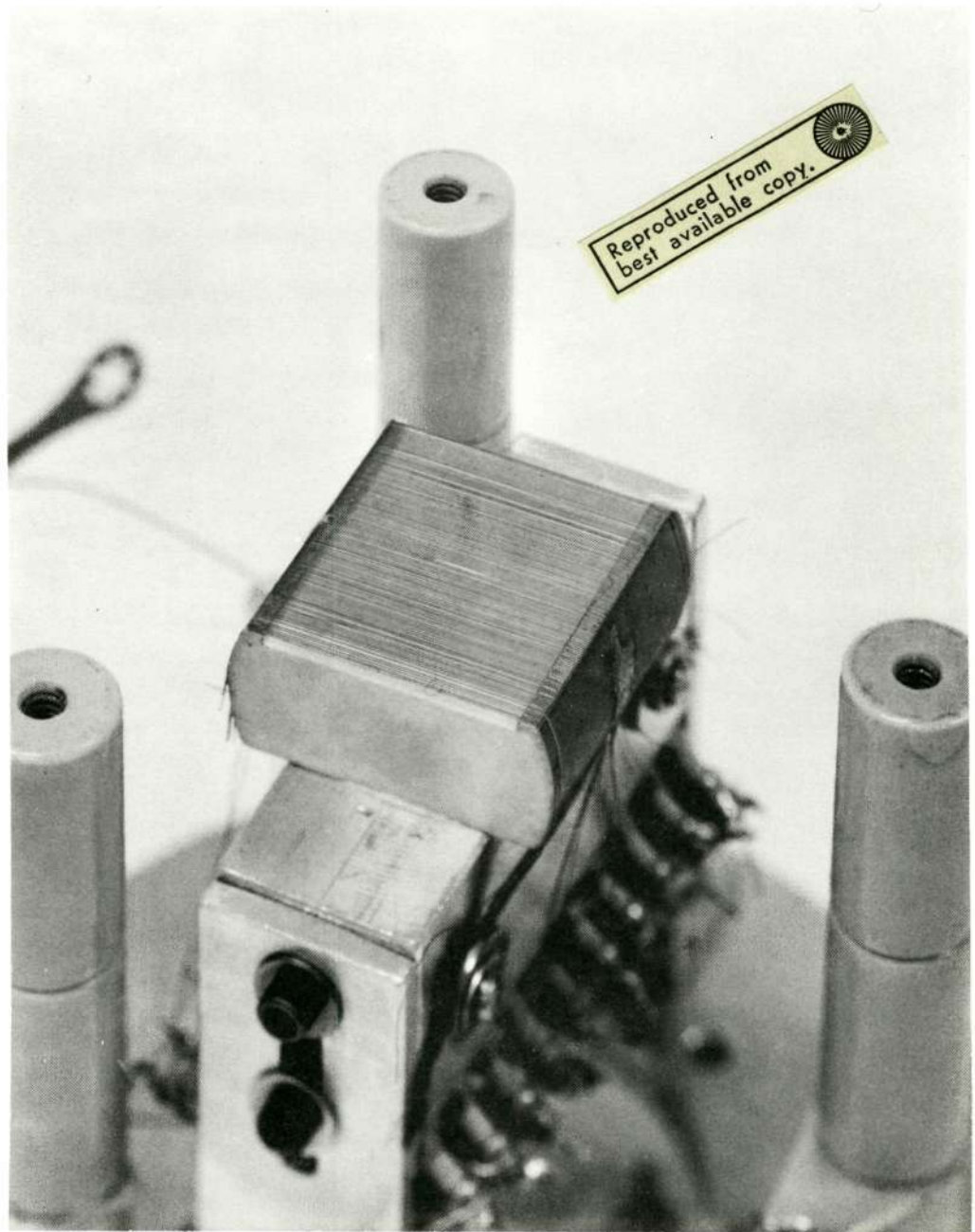
EG-020

Figure 3-6c. Views of Chevron Microchannel Plate with
Wire Array (With Guard Ring Removed Showing
Wire Array and Connections to Charge Divider)

For the purpose of this test the chevron plate and wire array were kept fixed and a slit was placed about 0.25 inches from the chevron plate on a digital table. The X-ray source was about 0.5 inch diameter and was about 30 feet distant. The digital table could be moved in 0.625 mil increments by means of stepping motors.

Figure 3-7 shows the effect of varying the collecting (chevron plate exit face to wire array) voltage. While the extremely narrow peak (less than the slit width wide) at 1 volt is not fully understood, the most likely reason for it is extreme diffusion of the electrons at this low voltage producing what is sensed as a narrow peak upon change collection. Two hundred volts was selected as the optimum as it produced a peak width compatible with the slit width but did not collect too heavily on individual wires. The effect of 5 mil movements of the slit near the center and ends of the 200 mil active array are shown in Figure 3-8.

The linearly of these measurements is shown by two least square fits in Figure 3-9. The solid line is a fit to all eight points and the dashed line to only the four center points. Some compression near the ends is noted.

The individual spectra from the ends of the wire array charge divider (with the slit near one end) are shown in Figure 3-10. The one with the higher gain shows the expected peak in the chevron plates output (it is below the discriminator level setting in the other).

The spatial distributions (figures 3-7 and 3-8) show considerable skirting. It was discovered subsequent to these measurements that the knives of the slit diverged by 12 mils in one inch of length. Another probable cause of skirting would be misalignment
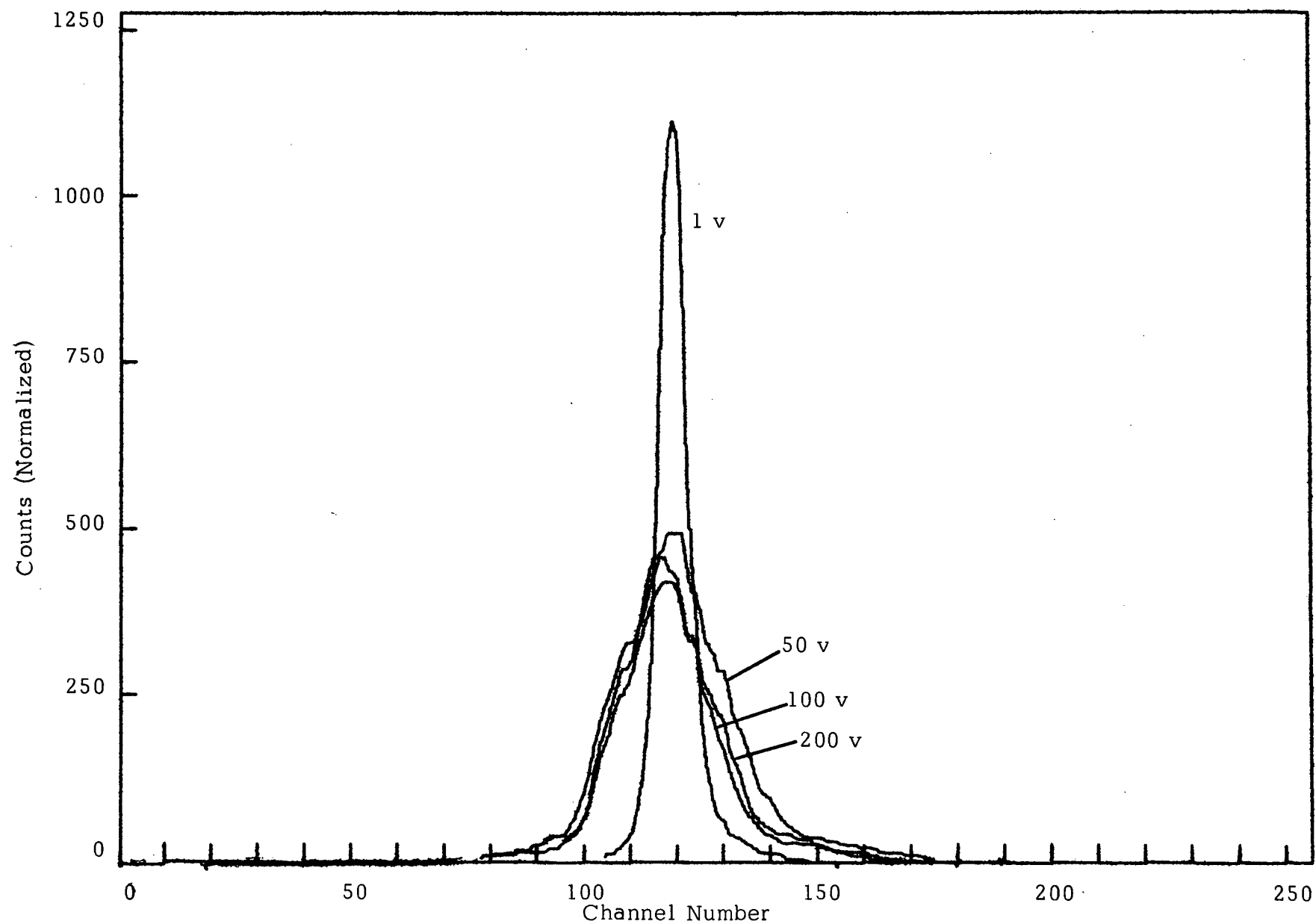
Figure 3-7.   Effect of Collecting Voltage on Position Distribution from Wire Array Charge Division
The 25 mil Slit Width is equivalent to 35 Channels.
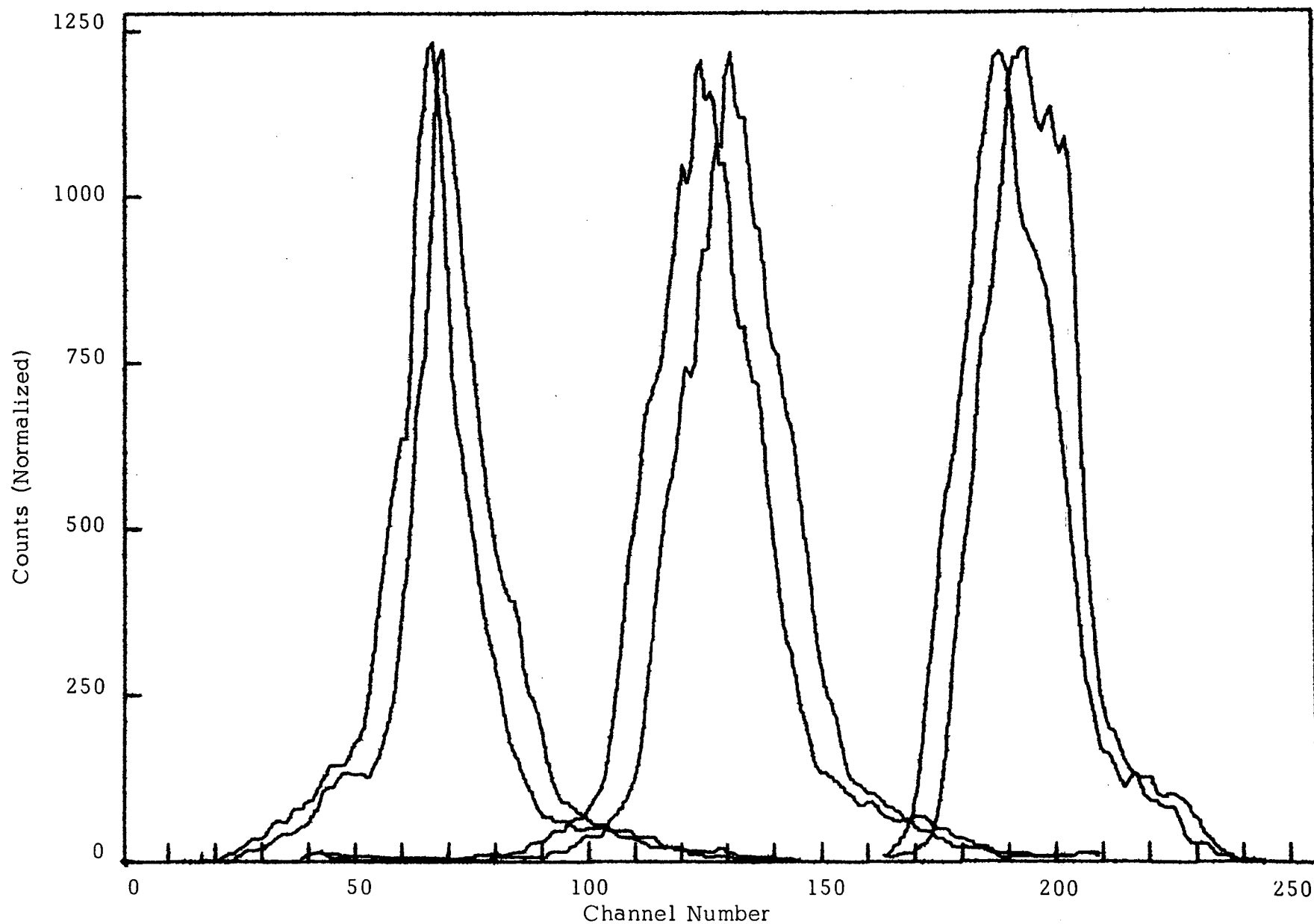
Figure 3-8.   Illustrating effect of 5 mil slit displacements at center and near each end of active
section of wire array.   Some of the structure is due to the discrete wire spacing.
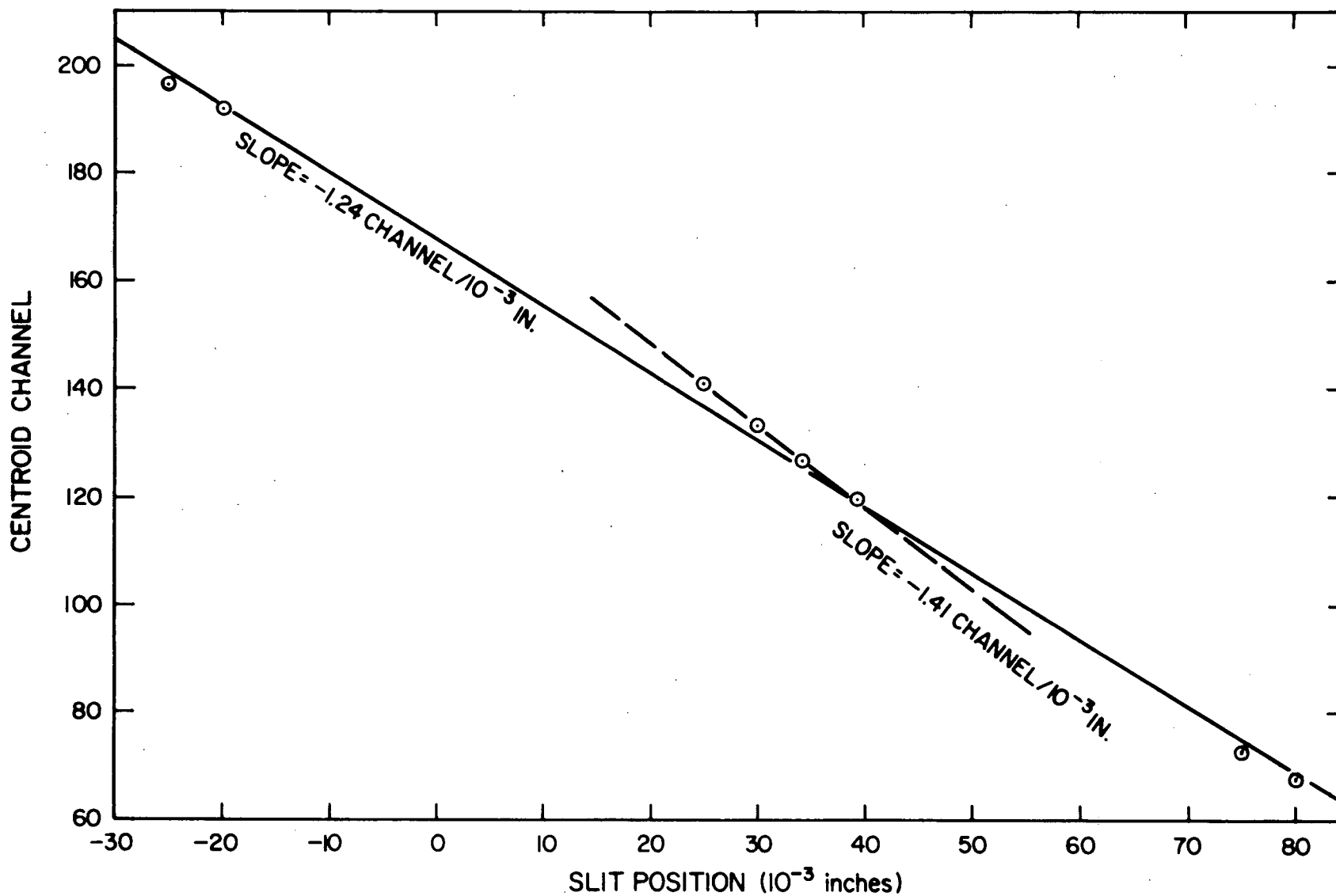
Figure 3-9.   Centroid Channel Number vs. Slit Position for Wire Array Readout. The Solid Line
is a Least Squares Fit to All Points; the Dashed Line is a Fit to the Four Center
Points Only.
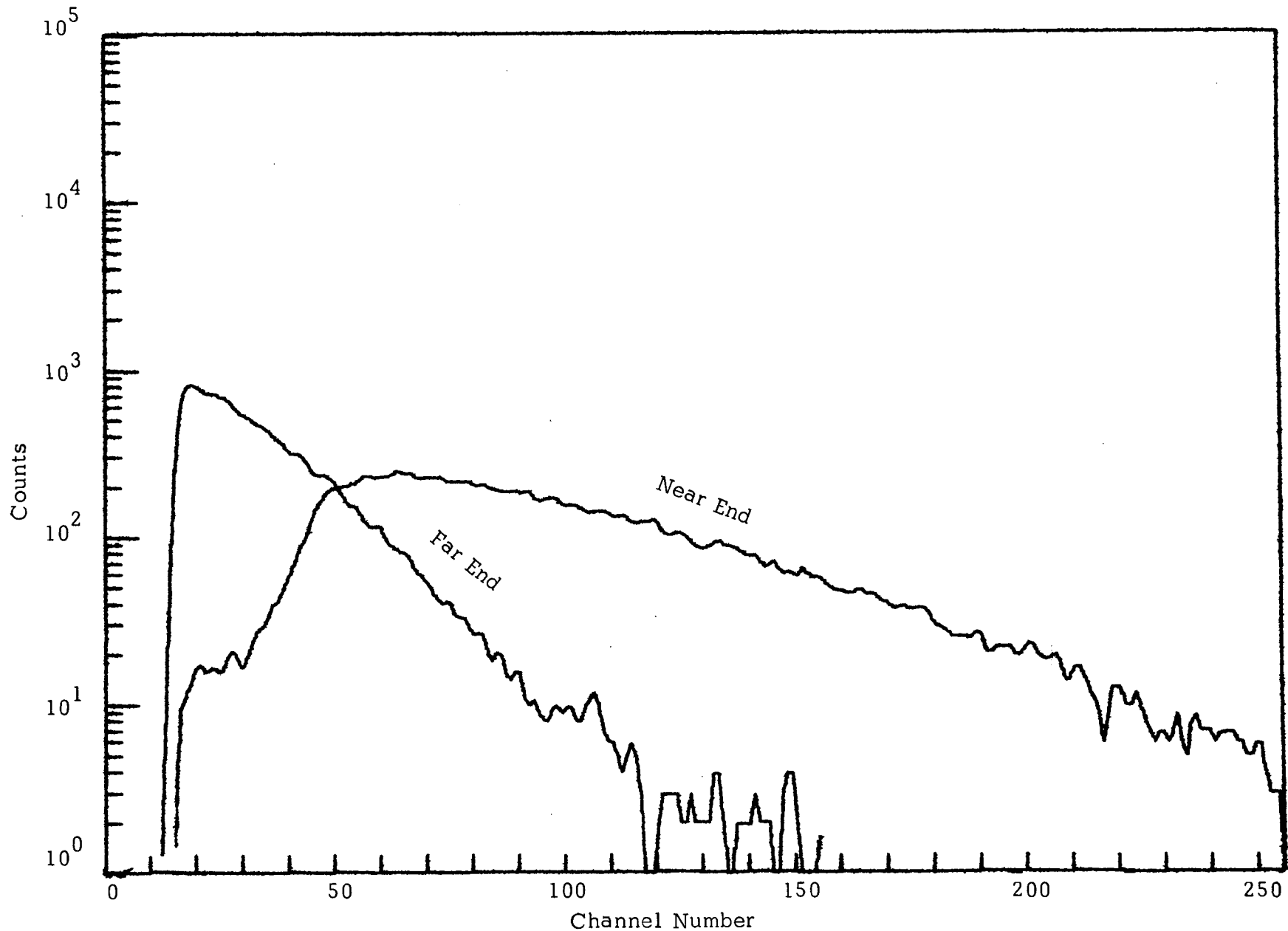
Figure 3-10. Spectra taken from opposite ends of charge divider behind chevron microchannel plate. The near end spectrum shows a peak in the distribution expected from this type of device.

of the slit with the wires. We assumed the alignment was good to about 15 minutes of arc which could produce an effect equivalent to a slit knife divergence of about 5 mils. Finding the value of the remaining error by subtracting RMS values gives

$$\sqrt{(12)^2 - (12/2)^2 - (5/2)^2} = 10 \text{ mils}$$

Factors which could cause this are:

1. Vibration of the chamber; the presence of large vacuum pumps was causing some vibration of the chamber and and the digital table had a considerable cantilever to it.

2. The analog-to-digital converter zero intercepts and amplifier gain settings were not optimized for minimum skirting due to the short time the vacuum system was available.

3. Non-linearities could have existed in the charge divider.

4. A compromise had to be made betwen wire tension and frequency of wire breakage. This could allow the wires to be non-linear by one or two mils.

Considering the brief period the testing facility was available to us, the performance of this wire array readout system was very promising.

4.0 OPTICAL DESIGN STUDIES

We have performed a number of analytical studies of the optical properties of X-ray mirrors as a function of the design parameters. The principal results have been published (J. App. Optics) and are contained in Appendices B and C.

4.1 Baez Optics

We have derived an analytical expression for the resolution of a Baez mirror and verified these results as well as evaluated other properties such as effective area by means of ray tracing calculations. We find that the resolution is proportional to the distance off axis and the ratio of mirror segment length to focal length. These results are given in detail in Appendix B. A Baez crossed parabola telescope was constructed. The unit, which is shown in Figure 4-1, consisted of one polished plate in each direction. The telescope was aligned to a predetermined focal spot and the curvature of the glass was adjusted to obtain the desired focal length. The curvature adjustments were performed in visible light by demanding that images using either the front or back portion of a plate were both centered on the desired focal spot; the adjustments were quite easy in practice and required about 20 minutes per plate after a moderately convenient setup was obtained.

The resulting X-ray focus using only one of the plates is shown in Figure 4-2; the width of the line is about 30 arc seconds and some slight scatter can be detected in the original negatives. The large density gradients at the edges of the line image indicate that the resolution was limited by poor focusing rather than by the quality of the surfaces.
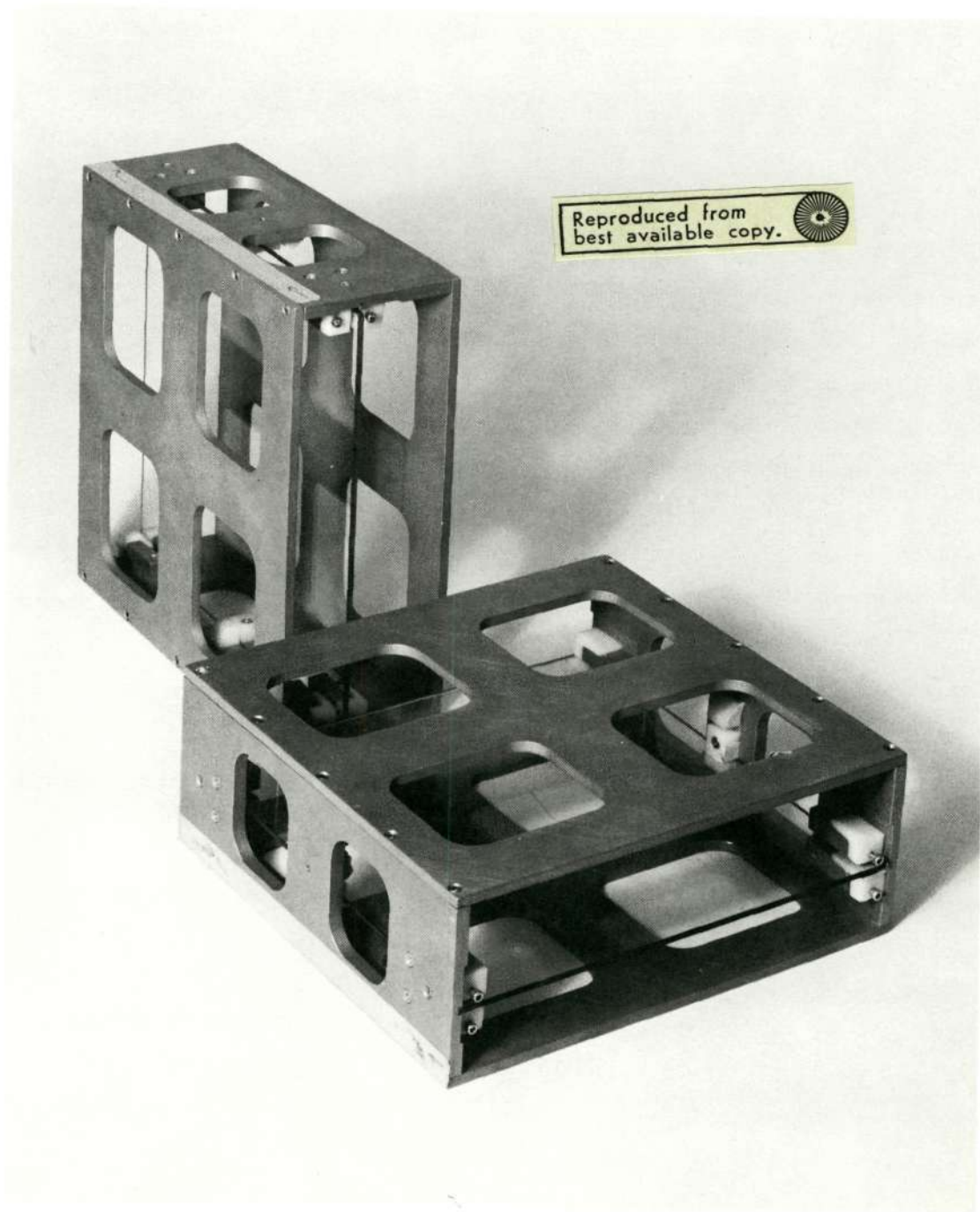
EL-024

Figure 4-1   A model Baez telescope. Each plate is 1/8 by 8 x 8
             inches and is selected polished plate glass. The
             segment length to focal length ratio is the same as
             proposed for the LOXT mission.

4-2

A two dimensional X-ray focus obtained with two such plates is shown in Figure 4-3. The spot is about 30 arc seconds by 40 arc seconds and again is limited by being out of focus. This resolution is already adequate for the LOXT mission and was achieved with rather simple devices.

4.2 Paraboloid-Hyperboloid Design Studies

We have evaluated the optical characteristics of X-ray telescopes of the paraboloid-hyperboloid type by means of a ray tracing procedure. Most of the results can be expressed as simple empirical formulae which are given in Appendix C; these results include the theoretical resolution, focal plane curvature, and resolution and vignetting factors for sources at a finite distance such as would be used in a test program. The principal result is that the resolution can be expressed as the sum of two terms, a term guadratic in the angle off axis and proportional to the grazing angle, and a second term which is linear in the angle off axis and proportional to the square of the grazing angle. The latter term, which always dominates for small off axis angles, can be eliminated by using the Wolter-Swartz shield solutions rather than the conic section designs. We are now constructing such a telescope in our solar astronomy program.

We have also evaluated the effects of various environments upon the preliminary LOXT high resolution mirror design; these results are given in Table III. In most of these calculations a perfect thermal match between mirror surface materials and support structures was assumed.

4.3 Telescope Mirror Evaluation

Mirror flats of graphite epoxy composition obtained from CONVAIR were tested for scattering using aluminum K X-rays (1.49 keV). Flat #1 was approximately 2 inches square and consisted of 0.06
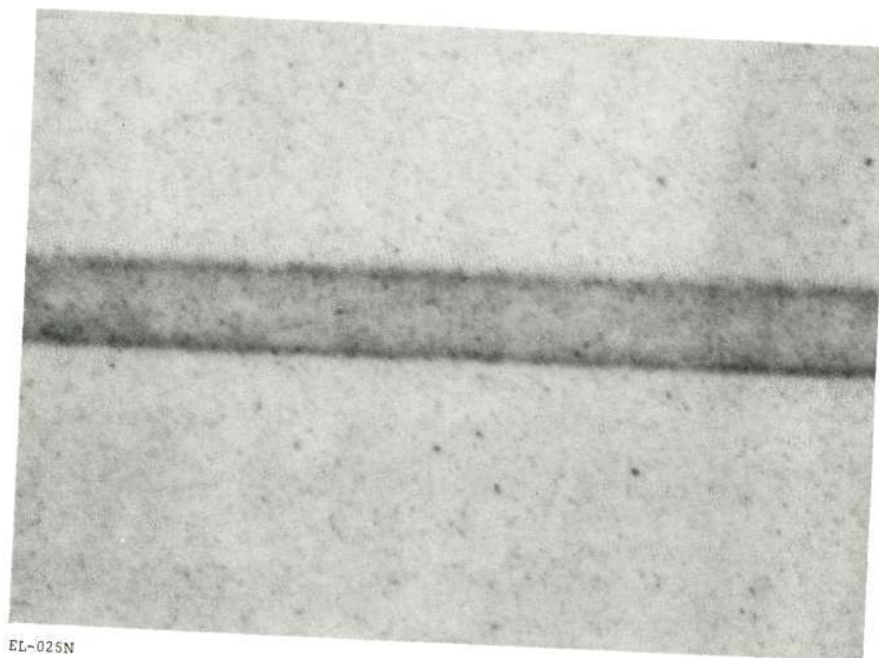
EL-025N

Figure 4-2   X-ray photograph of a small source taken with one of the mirrors shown in figure 4-1. The width of the line is about 30 arc seconds. The distribution indicates that the plate was somewhat out of focus but not limited by surface scatter.
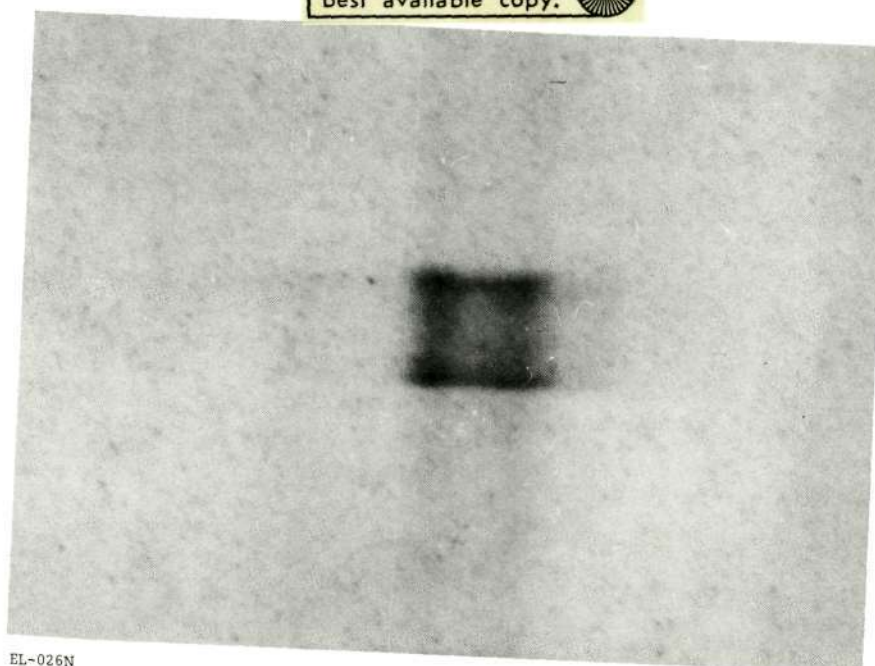
EL-026N

Figure 4-3   X-ray photograph of a small source taken with both of the units shown in figure 4-1. The spot is about 30 by 40 arc seconds and slightly out of focus

TABLE III

ENVIRONMENTAL EFFECTS ON LOXT PRELIMINARY
MIRROR DESIGN OPTICAL CHARACTERISTICS

Environmental Condition	RMS Blur Circle Radius for Axial Rays (arc second)
1. Gravity loading, assuming stiff flange supports at segments' ends and 1/2 inch Fused Silicon Wells	0.125
2. * Transverse Temperature Gradient, assuming $\alpha = 0.8.10^{-6}\ ^{O}C^{-1}$ ΔT across mirror	
$= 2.5\ ^{O}C$	0.336
$= 10\ ^{O}C$	1.34
3. *Axial Temperature Gradient, assuming $\alpha = 0.8.10^{-6}\ ^{O}C-1$ ΔT across mirror	
$= 2.5\ ^{O}C$	0.014
$= 10\ ^{O}C$	0.057

*These values assume a perfect thermal expansion
match between the supporting flanges and the
mirror materials.

inch composition covered with 0.05 inch of Vicor and 1000 $\overset{o}{A}$ of nickel. Flat #2 was a rectangle approximately 3" x 12" and consisted of 0.180" composition covered with 0.023" of quartz and 1000 $\overset{o}{A}$ of nickel. Flat #3 was circle approximately 10" in diameter and its exact structure was not given. Table IV below summarizes the results of the tests.

Table IV

	Angle of (Degrees) Incidence	Scatter FWHM (arc second)
Flat #1	0.641	59
Flat #2	0.561	145
Flat #3	0.620	194

Except for Flat #1, the scatter distribution had complicated structures.

This poor performance is believed to be attributable to the polishing techniques used rather than the intrinsic properties of the materials.

The scattering tests performed upon conventionally polished bulk fused silica and evaporated Ni on conventionally polished bulk fused silica essentially have reproduced the incident beam structure of about 5 arc seconds characteristic width.

5.0 CONCLUSIONS

Microchannel plates have proved to be rugged and useful X-ray conversion devices which preserve spatial resolution and as such are suitable in focal plane readout devices for the HEAO-C Mission. The spatial readout can be obtained either by collecting the electrons on a phosphor screen and viewing it through fiber optics and relay lenses with a low light level vidicon or by means of a crossed wire array utilizing charge division. The latter method operates in a single photon mode permitting data compaction and timing of pulsed sources. The performance of the wire array readout system was very promising. More developmental work is required to determine and reach its ultimate resolution in a 2-dimensional system.

The two areas requiring further development are the quantum efficiency and a practical version of the charge sensitive readout. Both of these areas will be continued in the Phase B portion of the HEAO-C program. We will attempt to inprove the quantum efficiency by using scintillator/photocathode assemblies. The practical development of a charge sensitive imaging readout will require the preparation of a large scale wire grid essentially by semiconductor fabrication techniques.

APPENDIX A
ASE-2978

Computer Program for Microchannel
Plate Evaluation

5 - 2

COMPUTER PROGRAM FOR MICROCHANNEL PLATE EVALUATION

A listing of the NOVA computer program developed for microchannel plate evaluation is given in this appendix. The values noted for the inputs apply to the lifetime readouts only.

; MICROCHANNEL PLATE EVALUATION PROGRAM

; REQUIRED: 1) FLOATING POINT INTERPRETER

;   2) INITIALIZATION ROUTINE

;   3) CARRIAGE RETURN/LINE FEED SUBROUTINE

; CALLED BY "Q" KEY

; PRIOR TO CALL REGION TO BE FITTED MUST BE INTENSIFIED

; INPUTS: 1) ZERO ENERGY CHANNEL (INCLUDE SIGN)
;   (ABOUT - 3.1)
;   2) CONVERSION FACTOR FROM SIGMA TO SIGMR
;   (ABOUT 1288.9)
;   3) Q.E. CONVERSION FOCTOR
;   (ABOUT 1.157E-6)
; PROGRAM WILL OUTPUT: 1) CHANNEL 0 INTENSITY

;   2) CHANNEL 30 INTENSITY

;   3) TRUE ZERO INTENSITY

;   4) SIGMA

;   5) INTEGRATED COUNTS

;   6) QUANTUM EFFICIENCY (%)

;   7) SIGMA(P)

; DISPLAY WILL SHOW DATA CURVE AND THE CALCULATED
;   CURVE OVERLAPPED WITH THE CALCULATED CURVE INTENSIFIE

```
011600                 .LOC    11600

; READ IN

11600 006005  IITST:  FINI              ; INIT AND ENTER FLT PT
11601 006004          FETR
11602 120000          FDFC    0         ; READ IN ZERO ENG CH
11603 040573          FSTA    0,ZECH    ; AND STORE IT
11604 120000          FDFC    0         ; READ IN CONV FACTOR FOR SIGMAP
11605 040573          FSTA    0,CFSP    ; AND STORE IT
11606 120000          FDFC    0         ; READ IN QUAMTUM EFF CONV FACTO
11607 040573          FSTA    0,QECF    ; AND STORE IT

; CALCULATE MATRIX ELEMENTS

11610 004104          FJSR    104       ; INITIALIZE SWEEP
11611 176400          FSUB    3,3       ; CLEAR AC3
11612 054572          FSTA    3,SEN     ; CLEAR FOR SUM OF SEN
11613 054573          FSTA    3,SLN     ; CLEAR FOR SUM LN Y
11614 054574          FSTA    3,SXLN    ; CLEAR FOR SUM X*LN Y
11615 054575          FSTA    3,SX      ; CLEAR FOR SUM X
11616 054576          FSTA    3,SX2     ; CLEAR FOR SUM OF SX↑2
```

```
11617 064144   NXCHN:  FLD3    144     ; GET CHANNEL NUMBER
11620 072062           FST3    @62     ; STORE FOR FLOAT
11621 006061           FJSR    @61     ; AND FLOAT IT
11622 105000           FMOV    0,1     ; SAVE IT IN FAC 1
11623 006060           FJSR    @60     ; GET AND CONVERT DATA
11624 101001           FMOV    0,0,FSGT        ; CHECK FOR =<0
11625 020571           FLDA    0,C1F   ; IF IT IS, MAKE IT A ONE
11626 034556           FLDA    3,SEN   ; GET SUM ON EN
11627 117000           FADD    0,3     ;   AND ADD NEW DATA
11630 054554           FSTA    3,SEN   ;     AND STORE IT BACK
11631 131000           FMOV    1,2     ; SAVE CHANNEL NO
11632 034560           FLDA    3,SX    ; GET SUM ON X
11633 110100           FMPY    0,2     ;   AND WEIGHT IT
11634 157000           FADD    2,3     ;     AND ADD NEW DATA
11635 054555           FSTA    3,SX    ;       AND STORE IT BACK
11636 034556           FLDA    3,SX2   ; GET SUM ON SX↑2
11637 130100           FMPY    1,2     ;     AND WEIGHT IT
11640 157000           FADD    2,3     ;       AND ADD NEW DATA
11641 054553           FSTA    3,SX2   ;       AND STORE IT BACK
11642 034544           FLDA    3,SLN   ; GET SUM ON LN Y
11643 110020           FALG    0,2     ; TAKE LOG OF INTENSITY
11644 110100           FMPY    0,2     ;     AND WEIGHT IT
11645 157000           FADD    2,3     ;       AND ADD NEW DATA
11646 054540           FSTA    3,SLN   ;        AND STORE IT BACK
11647 034541           FLDA    3,SXLN  ; GET SUM ON X LN Y
11650 130100           FMPY    1,2     ;   AND WIGHT IT
11651 157000           FADD    2,3     ;     AND ADD NEW DATA
11652 054536           FSTA    3,SXLN  ;       AND STORE IT BACK
11653 010144           FISZ    144     ; INCREMENT CHANNEL NUMBER
11654 014145           FDSZ    145     ; DECREMENT CHANNELS TO GO
11655 000742           FJMP    NXCHN   ; GO TO NEXT CHANNEL

        ; CALCULATE   D = SEN*SX↑2 - SX*SX

11656 024526           FLDA    1,SEN
11657 034535           FLDA    3,SX2
11660 030532           FLDA    2,SX
11661 164100           FMPY    3,1
11662 150100           FMPY    2,2
11663 146400           FSUB    2,1
11664 044534           FSTA    1,D

        ; CALCULATE A0 = EXP((SLN*SX↑2 - SXLN*SX)/D)

11665 030521           FLDA    2,SLN
11666 170100           FMPY    3,2
11667 024521           FLDA    1,SXLN
11670 020522           FLDA    0,SX
11671 120100           FMPY    1,0
11672 112400           FSUB    0,2
11673 020525           FLDA    0,D
11674 110200           FDIV    0,2
11675 150220           FEXP    2,2
11676 050524           FSTA    2,A0

        ; CALCULATE A1 = (SEN*SXLN - SX*SLN)/D

11677 020505           FLDA    0,SEN
11700 120100           FMPY    1,0
11701 024511           FLDA    1,SX
```

A-3

```
11702 030504          FLDA      2,SLN
11703 130100          FMPY      1,2
11704 142400          FSUB      2,0
11705 024513          FLDA      1,D
11706 120200          FDIV      1,0
11707 040515          FSTA      0,A1
```

; CALCULATE AND PRINT OUT RESULTS

```
11710 006074          FJSR      @74       ; CARRIAGE RETURN/LINE FEED
11711 020511          FLDA      0,A0      ; GET ZERO CHANNEL COUNTS
11712 140000          FFDC      0         ; OUTPUT ZERO CHANNEL CONTENTS
11713 006074          FJSR      @74
11714 020512          FLDA      0,C30F    ; GET FLOATING THIRTY
11715 004453          FJSR      CCC       ; GO TO CALC CHANNEL CONTENTS
11716 140000          FFDC      0         ; OUTPUT CHANNEL 30 CONTENTS
11717 006074          FJSR      @74
11720 020456          FLDA      0,ZECH    ; GET ZERO ENERGY CHANNEL
11721 004447          FJSR      CCC
11722 140000          FFDC      0         ; OUTPUT TRUE ZERO INTENSITY
11723 024473          FLDA      1,C1F     ; GET A FLOATING ONE
11724 030500          FLDA      2,A1      ;    TO INVERT A1
11725 151400          FPOS      2,2
11726 144200          FDIV      2,1       ;        TO GIVE SIGMA
11727 006074          FJSR      @74
11730 144000          FFDC      1         ;          AND PRINT IT OUT
11731 006074          FJSR      @74
11732 120100          FMPY      1,0       ; CALC INTEGRAL COUNT
11733 140000          FFDC      0         ; AND PRINT IT OUT
11734 030446          FLDA      2,QECF    ; GET QUANT EFF CONV FACTOR
11735 140100          FMPY      2,0       ; AND CALCULATE Q.E. IN %
11736 006074          FJSR      @74
11737 140000          FFDC      0         ; AND PRINT IT OUT
11740 030440          FLDA      2,CFSP    ; GET CONV FACT FOR SIGMA(P)
11741 144100          FMPY      2,1
11742 006074          FJSR      @74
11743 144000          FFDC      1         ; PRINT OUT SIGMA(P)
11744 006074          FJSR      @74
```

; ROUTINE TO CALCULATE SPECTRUM

```
11745 064463          FLD3      C200
11746 070140          FST3      140
11747 064462          FLD3      C377
11750 070141          FST3      141
11751 004104          FJSR      104
11752 176400          FSUB      3,3
11753 030443          FLDA      2,C1F
11754 161000   NXCH:  FMOV      3,0
11755 004413          FJSR      CCC
11756 006063          FJSR      @63
11757 010020          FISZ      20
11760 072020          FST3      @20
11761 142405          FSUB      2,0,FSGE
11762 000404          FJMP      OUT
11763 157000          FADD      2,3
11764 014145          FDSZ      145
11765 000767          FJMP      NXCH
11766 100000   OUT:   FEXT
11767 000443          JMP       EXIT
```

A-4

C-2

; SUBROUTINE TO CALC CHANNEL CONTENTS

```
11770 024434   CCC:    FLDA    1,A1
11771 120100           FMPY    1,0
11772 100220           FEXP    0,0
11773 024427           FLDA    1,A0
11774 120100           FMPY    1,0
11775 001400           FJMP    0,3

11776 000000   ZECH:   0                       ; ZERO ENERGY CHANNEL
11777 000000           0
12000 000000   CFSP:   0                       ; CONV FACTOR FOR SIGMA(P)
12001 000000           0
12002 000000   QECF:   0                       ; QUANTUM EFF CONV FACTOR
12003 000000           0
12004 000000   SEN:    0                       ; NUMBER OF CHANNELS
12005 000000           0
12006 000000   SLN:    0                       ; SUM OF LN Y
12007 000000           0
12010 000000   SXLN:   0                       ; SUM OF X*LN Y
12011 000000           0
12012 000000   SX:     0                       ; SUM OF X
12013 000000           0
12014 000000   SX2:    0                       ; SUM OF X↑2
12015 000000           0
12016 040420   C1F:    40420                   ; ONE FLOATING
12017 000000           0
12020 000000   D:      0                       ; DENOMINATOR IN MATRIX SOLUTION
12021 000000           0
12022 000000   A0:     0                       ; UNCORRECTED ZERO INTERCEPT
12023 000000           0
12024 000000   A1:     0                       ; ATTENUATION COEFFICIENT
12025 000000           0
12026 041036   C30F:   41036                   ; THIRTY FLOATING
12027 000000           0
12030 000200   C200:   200                     ; LOWER ADDRESS FOR CALC SPECTRM
12031 000377   C377:   377                     ; UPPER ADDRESS FOR CALC SPECTRM

12032 022403   EXIT:   LDA     0,@.+3
12033 042403           STA     0,@.+3
12034 000270           JMP 270

12035 000733           733
12036 000732           732

      000167           .LOC  167
00167 011600           11600

                       .END
```

A-5

```
A0      012022
A1      012024
C1F     012016
C200    012030
C30F    012026
C377    012031
CCC     011770
CFSP    012000
D       012020
EXIT    012032
IITST   011600
NXCH    011754
NXCHN   011617
OUT     011766
QECF    012002
SEN     012004
SLN     012006
SX      012012
SX2     012014
SXLN    012010
ZECH    011776
```

APPENDIX B
from ASE-2519

Orthogonal Mirror Telescopes
for X-ray Astronomy

$A - 7$

ORTHOGONAL MIRROR TELESCOPES
FOR X-RAY ASTRONOMY

L. P. VanSpeybroeck, R. C. Chase, and T. Zehnpfennig*

American Science & Engineering, Inc.
Cambridge, Massachusetts   02142

ABSTRACT

Crossed mirror telescopes are presented as an alternative to the present telescope systems used in x-ray astronomy. These instruments generally have a higher x-ray collecting efficiency but a poorer angular resolution than the more conventional paraboloid-hyperboloid telescopes. They also can be made more easily and quickly as was demonstrated by a recent rocket flight which used a simplified mirror design with only one-dimensional focusing.

* Now at Visidyne Corporation, Woburn, Massachusetts

The application of focusing x-ray optics to x-ray astronomy was first discussed by Giacconi and Rossi[1]. Since that time much work has been done on grazing incidence imaging systems. One type of system utilizes reflecting conic sections of revolution[2,3]. Telescopes of this geometry have been used with great success for obtaining high resolution photographs of the sun in x-rays[4,5]. Fisher and Meyerott[6] have built another type of system with one-dimensional focusing which is composed of reflecting parabolas of translation. A system of one-dimensional focusing has recently been flown successfully in a sounding rocket by Gorenstein et al.[7]; during this flight x-ray images of the Cygnus Loop were obtained. As an alternative to the present instruments, we have designed several telescope configurations which focus the x-rays with sets of two orthogonal parabolas of translation. The use of crossed mirrors for x-ray focusing was first proposed by Kirkpatrick and Baez[8]. McGee successfully demonstrated the use of crossed-spherical reflectors in an x-ray microscope[9].

A simplified Kirkpatrick-Baez device is shown in Figure 1a. The incident ray successively strikes two parabolas at approximately right angles to one another. In practical designs, the surface area is increased by using many approximately parallel parabolas as in Figure 1b.

The equations for the individual surfaces can be written:

$$X_1^2 = P_1^2 + 2P_1 (Z_1 + a); \qquad Y_1 \text{ arbitrary} \qquad (1)$$

$$Y_2^2 = P_2^2 + 2P_2 Z_2; \qquad X_2 \text{ arbitrary} \qquad (2)$$

where Z is the symetry axis, the focal plane is at $Z = 0$ and the x-rays first strike the surface described by equation (1). The displacement of the focus of the first parabola is necessary because

of the second reflection, and optimum focus is achieved when $a = P_2$. We have calculated the exact solution to this geometry[*], and if $a \approx P_2$, the principle error is determined by the length of the mirror segments; neglecting all sources of error and corrections small compared to the error determined by the length of the mirror section, we obtain the following approximate intersection in the focal plane:

$$Y_F = f(1 - \Delta_2) \tan \theta \sin \phi \qquad (3)$$

$$X_F = f(1 + \Delta_1) \tan \theta \cos \phi + f \left(\frac{X_1}{f}\right) \left(\frac{a - P_2}{f}\right) \qquad (4)$$

where the initial ray direction is given by the polar angle θ, and azimuthal angle ϕ, and the ray intersections with the surfaces occur at X_1, Y_1, Z_1 and X_2, Y_2, Z_2 and

$$Z_1 = f(1 + \Delta_1); \quad Z_2 = f(1 - \Delta_2); \quad \Delta_1, \Delta_2 \geq 0 \qquad (5)$$

The radius of the blur circle for a symmetric geometry is thus proportional to (Δ_{max}) which is the length of the mirror segment over the focal length. Therefore, this quantity should be minimized to obtain high resolution. However, it must be maximized to obtain a large area, and for a given application a compromise is required.

In one of our designs we arranged parallel sets of mirrors into four rectangular modules. The appearance of the modules at the front aperture are shown in Figure 1c. Each module consists of 22 parabolic sheets followed by 26 sheets at right angles to the first. We analyzed the performance of this telescope with a ray-tracing computer program. Fixed angle rays arriving at random locations in the front aperture were traced through the system in a Monte-Carlo process. The surface reflection efficiency as a

*The exact solutions are:

$$
y_F = \frac{\left(z_2 + P_2\right)\left(1 + \dfrac{P_1}{z_1 + a}\right)\left(1 + \dfrac{P_2}{z_2}\right)\tan\theta\,\sin\phi}{1 + \left(\dfrac{x_1}{z_1 + a}\right)\tan\theta\,\cos\phi + \left(\dfrac{y_2}{z_2}\right)\left(1 + \dfrac{P_1}{z_1 + a}\right)\tan\theta\,\sin\phi}
$$

$$
\begin{aligned}
x_f = \left(z_1 + P_2\right)&\Biggl\{\left[1 + \left(\frac{x_1}{z_1 + a}\right)^2\left(1 + \frac{2(a - P_2)}{z_1 + P_2}\right)\right]\tan\theta\,\cos\phi + \left(\frac{x_1}{z_1 + a}\right)\left(\frac{a - P_2}{z_1 + P_2}\right)\\[2mm]
&+ \left(1 + \frac{a}{z_2}\right)\left(1 + \frac{P_1}{z_1 + a}\right)\left(\frac{x_1}{z_1 + a}\right)\left(\frac{y_2}{z_1 + P_2}\right)\tan\theta\,\sin\phi\\[2mm]
&+ \left(1 + \frac{a - P_2 + P_1}{z_1 + P_2}\right)\left(\frac{y_2}{z_2}\right)\left[\left(\frac{x_1}{z_1 + a}\right)^2 - \frac{(z_2 - z_1)}{z_1 + a}\right]\tan^2\theta\,\sin\phi\,\cos\phi\Biggr\}\\[2mm]
\div\ &\left\{\left(1 + \frac{x_1}{z_1 + a}\right)\tan\theta\,\cos\phi\right)\left(1 + \frac{x_1}{z_1 + a}\tan\theta\,\cos\phi + \frac{y_2}{z_2}\left(1 + \frac{P_1}{z_1 + a}\right)\tan\theta\,\sin\phi\right\}
\end{aligned}
$$

B-4

function of wavelength and grazing angle was taken into account using the formalism presented in Reference (2), pages 12-14. Rays which hit the backs or edges of mirrors were rejected. The reflecting surface was assumed to be chromium.

We define the effective collecting area of the telescope as

$$A_{eff} = A_{geom} (\frac{1}{N}) (\sum_i \epsilon_i^1 \epsilon_i^2)$$ (6)

where the sum includes only the rays which reach the focal plane, ϵ_i^1 and ϵ_i^2 are the reflection efficiencies for reflection from the first and second parabola respectively; A_{geom} is the geometric area which rays may traverse at the front aperture; and N is the number of random rays incident on the front aperture.

In Figure 2 we have plotted the effective collecting area vs. wavelength for various angles of incidence. The dip at about 21 $\overset{o}{A}$ is due to the L absorption edges of chromium. The points of this figure and of the figures which follow were calculated to approximately 5% accuracy. In Figure 2 the azimuthal angle, ϕ, of incident rays was fixed at zero degrees (ϕ measured from the x axis). At $\phi = 90°$, the effective area is appreciably larger for large θ. For 40 $\overset{o}{A}$ rays and $\phi = 90°$, $A_{eff} = 1097$ cm^2 at $\theta = 20'$, and $A_{eff} = 555$ cm^2 at $\theta = 1°$.

Some of the rays which reach the focal plane are reflected only once from either a front or a rear mirror. Others reach the focal plane undeflected. These "background" rays can easily be distinguished from rays which make two reflections because in general they will reach the focal plane at locations other than the image location of two reflections. They can also be reduced considerably by appropriate masking of the front aperture.

In Figure 3 we have plotted the RMS blur circle radius on a flat focal plane vs. polar angle of incidence. The blur circle radius is not appreciably dependent upon the azimuthal angle of incidence of the rays.

An alternative Kirkpatrick-Baez telescope configuration is shown in Figure 1d. This type of design makes more efficient use of the area available at the front aperture. Figures **4** and 5 are respectively the effective area and the resolution results for this design. The surface material is Nickel, and the dip corresponds to the L edges of Nickel. This type of design, of course, has negligible azimuthal dependance.

Telescopes of the crossed parabola design can generally be fabricated more easily and quickly than paraboloid-hyperboloid types of comparable x-ray gathering capacity. Because the mirrors need not be self-supporting during polishing or over large spans in the final instrument, they can be made quite thin, and this in turn makes very efficient use of the available front aperture. The use of optical flats assures the best possible surface finish available and therefore the highest reflection efficiencies. Experiments can be precisely tailored to their objectives because the telescopes are easily made. For example, a telescope of large grazing angle would be used for soft x-ray sources, whereas a smaller grazing angle instrument would be used to detect the hard portion of the spectra.

The sounding rocket flight of Gorenstein et al.[7] demonstrates that parabolas of translations, such as have been proposed here, can be successfully fabricated. The telescope used on this rocket consisted of eight plates of 0.10 cm thick chromium plated commercial float glass backed by 0.051 cm of steel. Each plate was 18.8 cm x 40.6 cm and was constrained to the calculated parabola

by a series of accurately located pins. The theoretical reflectivity, calculated by the same program which yielded Figures 2 through 5, was verified at 9.87 $\overset{o}{A}$ to within about 20% by laboratory measurements. The resolution, however, was considerably worse than calculated as a result of ripples in the glass.

In conclusion, the crossed-parabola systems should find application in astronomical observations such as high sensitivity surveys, photometry and certain kinds of spectroscopy where a large effective area rather than high angular resolution is the most important factor.

REFERENCES

1. R. Giacconi and B. Rossi, J. Geophys. Res. <u>65</u>, 773 (1960).

2. R. Giacconi, W. P. Reidy, G. S. Vaiana, L. P. VanSpeybroeck and T. F. Zehnpfennig, Space Sci. Rev. <u>9</u>, 3 (1969).

3. J. D. Mangus and J. H. Underwood, Appl. Opt. <u>8</u>, 95 (1969).

4. G. S. Vaiana, W. P. Reidy, T. Zehnpfennig, L. VanSpeybroeck, and R. Giacconi, Science <u>161</u>, 564 (1968).

5. L. P. VanSpeybroeck, A. S. Krieger and G. S. Vaiana, Nature <u>227</u>, 818 (1970).

6. P. C. Fisher and A. J. Meyerott, IEEE Trans. Nucl. Sci. <u>NS-13</u>, 580 (1966).

7. P. Gorenstein, <u>et al</u>. "Soft X-Ray Observation of the Cygnus Loop," presented to the International Astronomical Union General Assembly XIV, Brighton, 1970 (to be published).

8. P. Kirkpatrick and A. V. Baez, J. Opt. Soc. Am. <u>38</u>, 766 (1948).

9. J. F. McGee in <u>X-Ray Microscopy and Microradiography</u> (ed. by V. E. Cosslett, A. Engström and H. H. Patte). Academic Press, New York, p. 164 (1957).

FIGURE CAPTIONS

Figure 1a   A simple Kirkpatrick-Baez device.

Figure 1b   A nested set of orthogonal mirrors.

Figure 1c   A representation of the front aperture of the telescope
with rectangular geometry. The focal length of this
telescope is 559 cm as measured from the plane be-
tween orthogonal sets of parabolas. The depth of
each set is 50. 8 cm. The thickness of the mirrors
is 0. 635 cm.

Figure 1d   A representation of the front aperture of the telescope
with sixteen fold symmetry. The focal length is
792. 5 cm. The depth of each of the two sets of
orthogonal parabolas is 61. 0 cm. The mirror
thickness is 0. 317 cm. Each module is encased in
a container 0. 635 cm thick and has 51 mirrors; 26
in the front set and 25 in the rear set.

Figure 2   Effective collecting area of the telescope with rec-
tangular geometry vs. incident wavelength. Results
are given for several values of the incident polar
angle θ. The azimuthal angle of incident rays is
fixed.

Figure 3   The RMS blur circle radius of the telescope with
rectangular geometry vs. incident polar angle.

Figure 4   The effective area of the telescope with sixteen fold
symmetry vs. incident wavelength for various polar
angles.

Figure 5   The RMS blur circle radius of the telescope with
sixteen fold symmetry vs. incident polar angle.
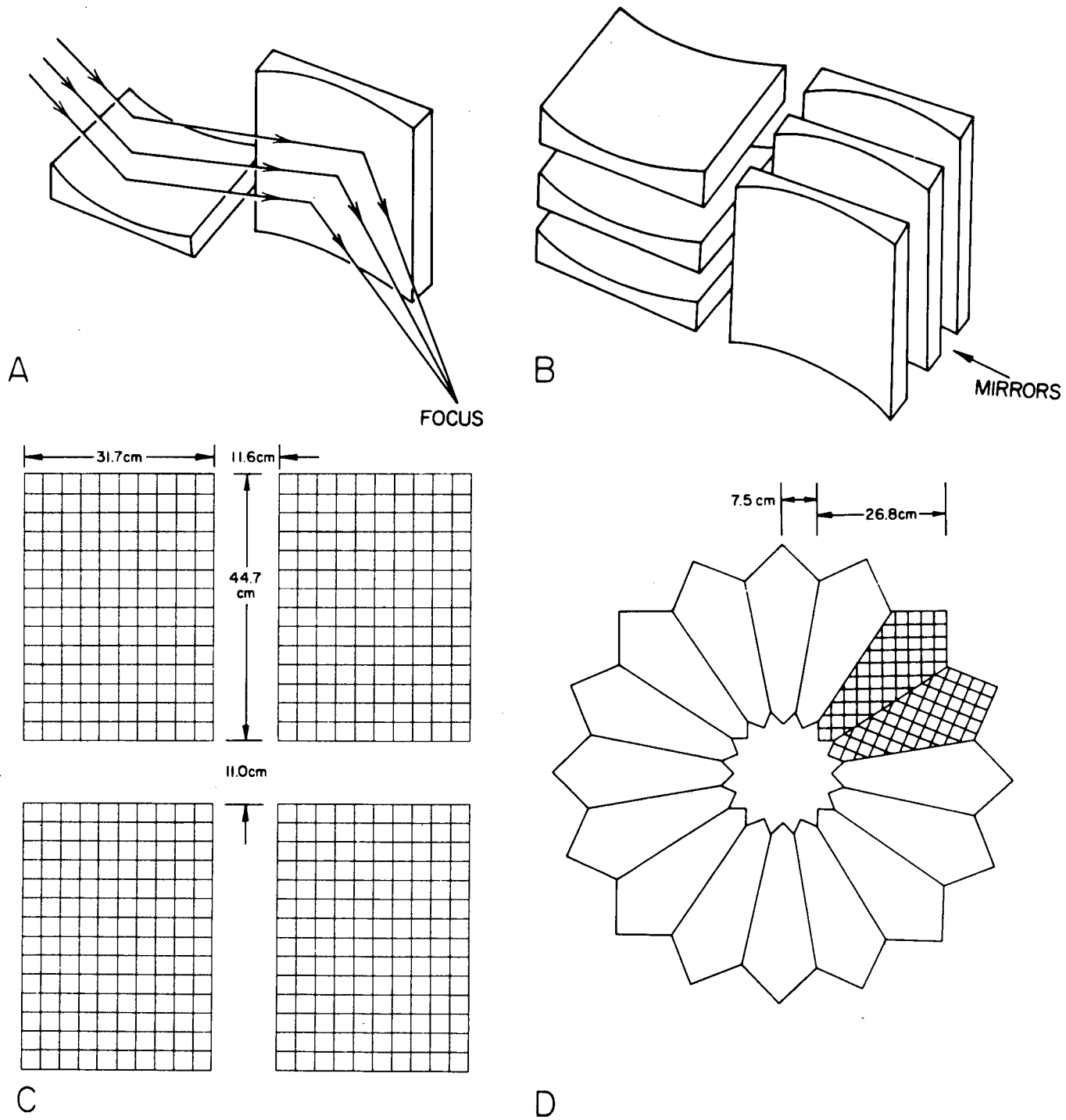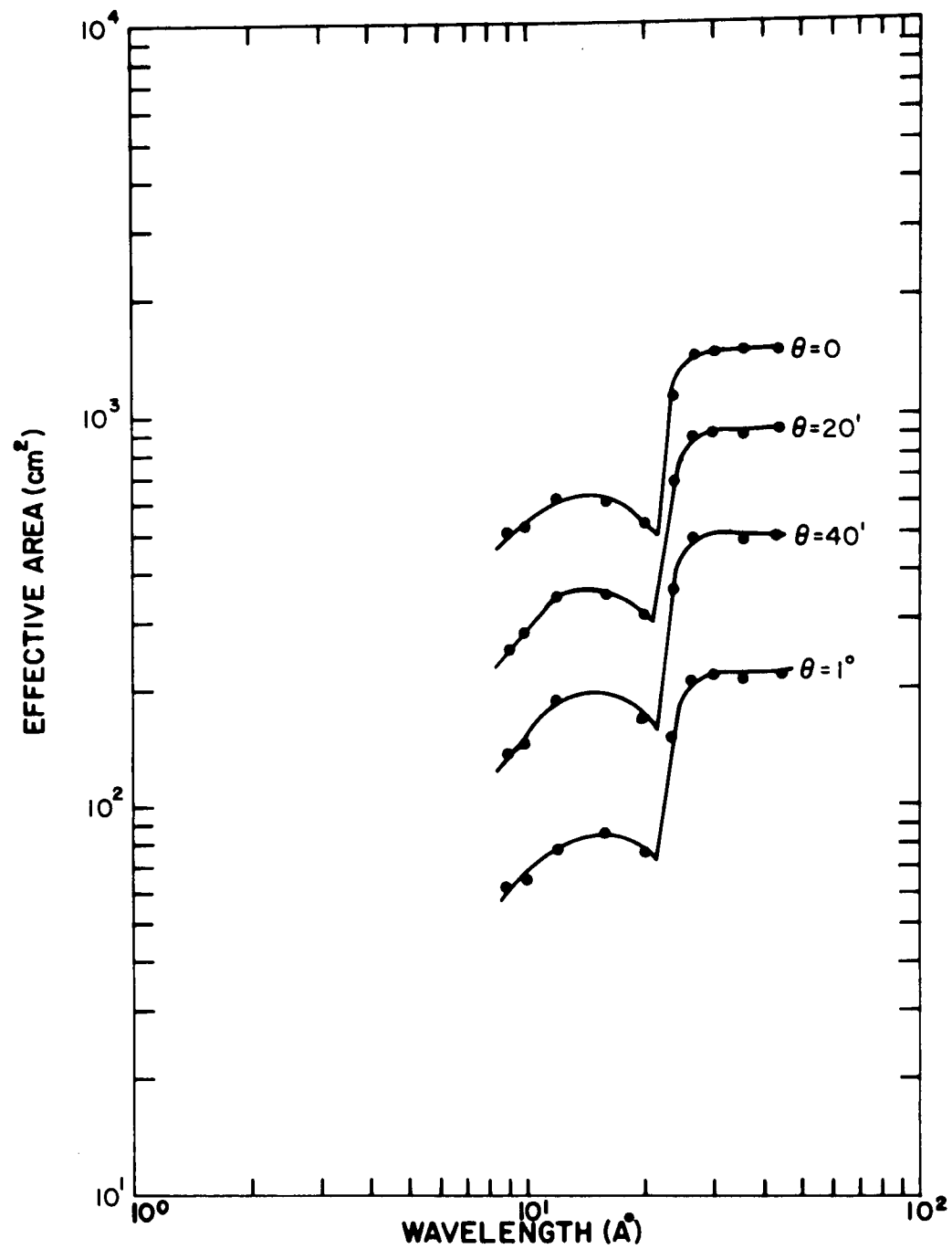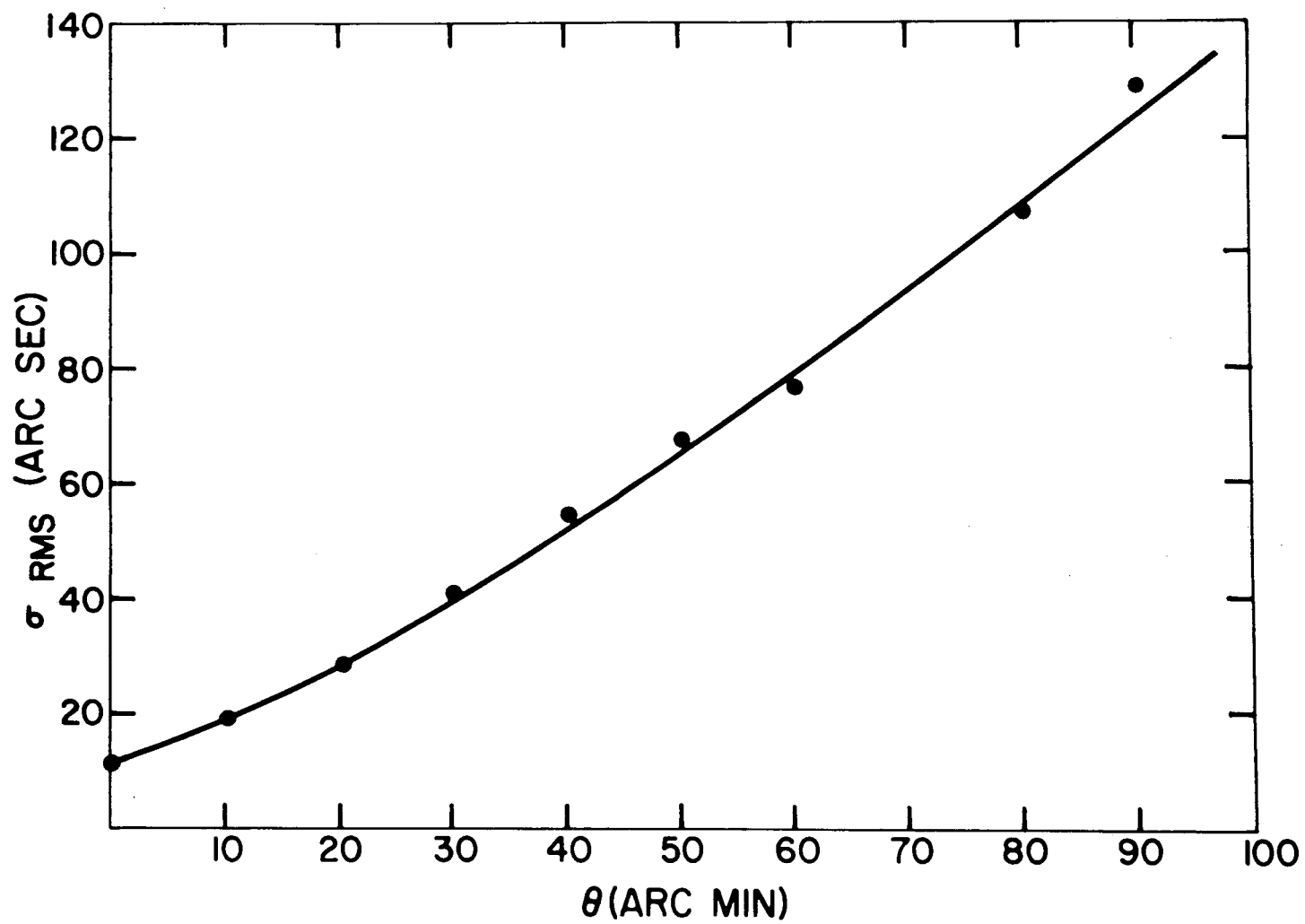
A

FOCUS
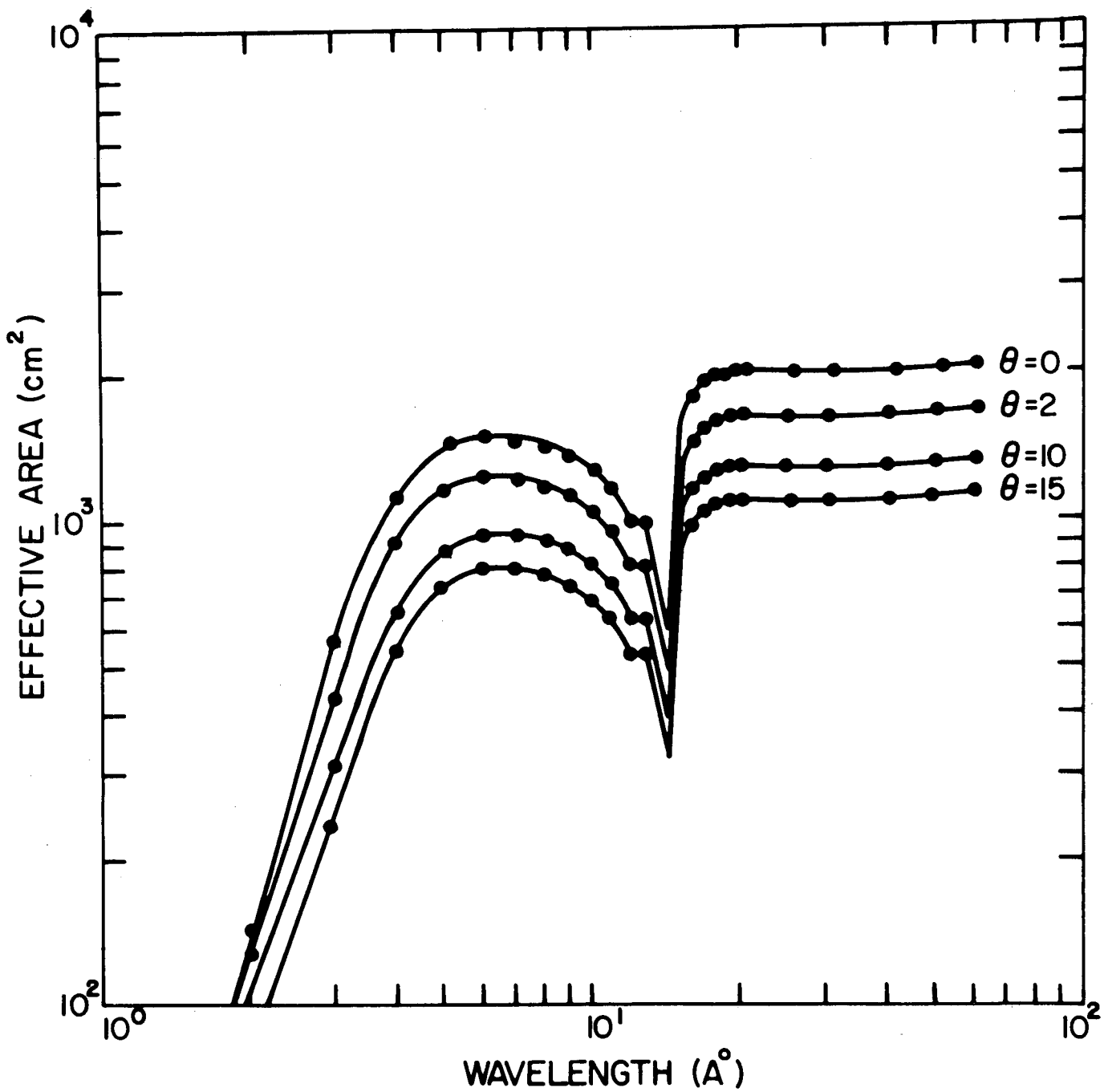
B

MIRRORS

C

D

31.7cm

11.6cm

44.7 cm

11.0cm

7.5 cm

26.8cm

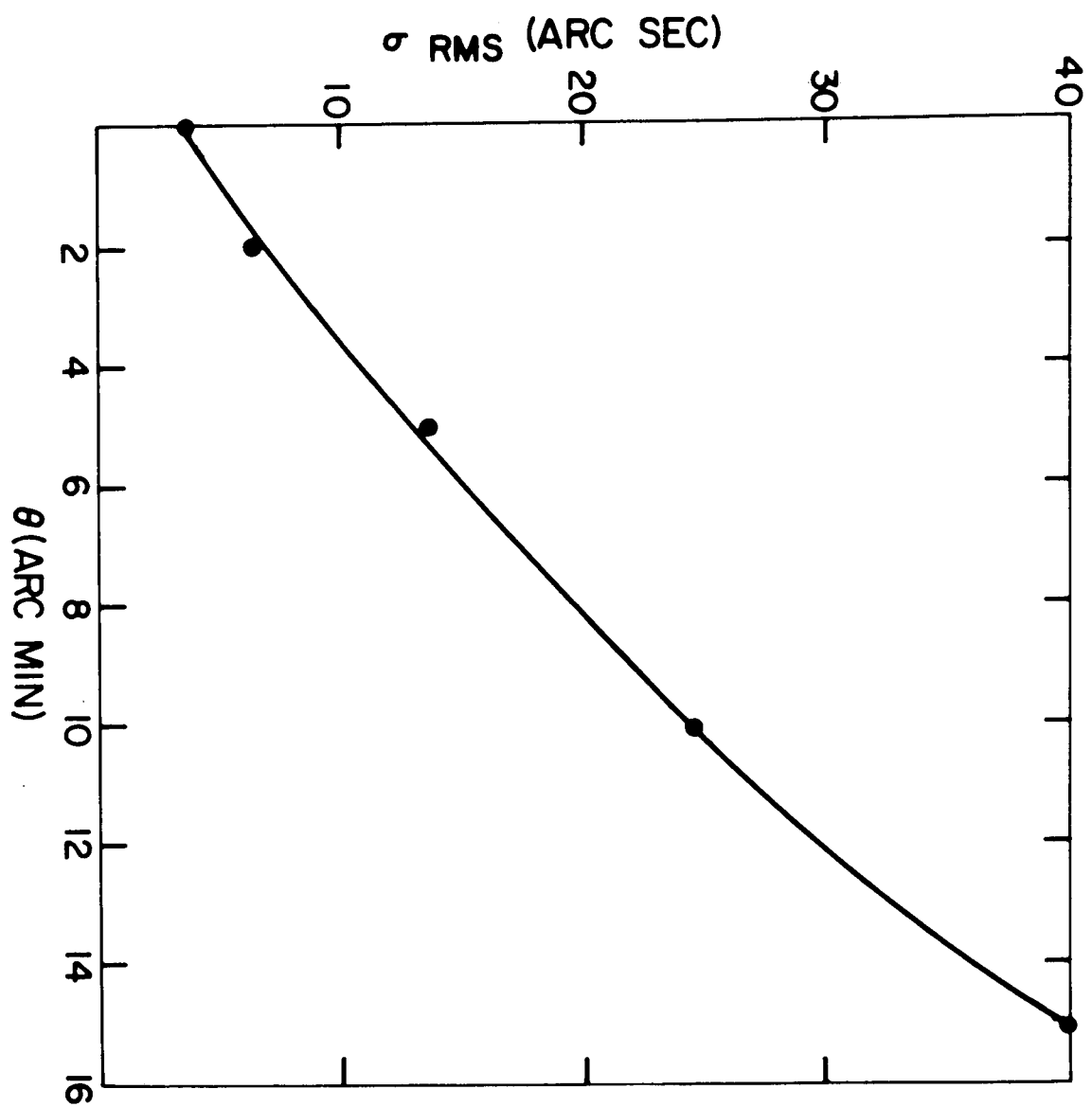Figure 1

Figure 2

B-11

Figure 3

Figure 4

Figure 5

B-14

APPENDIX C
from ASE-2686

Paraboloid-Hyperboloid X-ray Telescopes

B - 15

PARABOLOID-HYPERBOLOID X-RAY TELESCOPES

L. P. VanSpeybroeck and R. C. Chase

American Science and Engineering
Cambridge, Massachusetts 02142

ABSTRACT

We have evaluated the principal optical characteristics of Paraboloid-Hyperboloid X-ray telescopes by a ray tracing procedure; we find that our results for resolution, focal plane curvature, and finite source distance effects may be approximated in terms of the design parameters by simple, empirical formulae which should be useful to people considering X-ray telescope experiments.

This work has been partially supported by NASA contract NAS8 24385.

Giacconi and Rossi[1] first discussed the application of focusing X-ray optics to astronomy. The highest resolution X-ray mirrors presently being used in X-ray astronomy consist of two successive concentric figures of revolution in which the two generating curves are concentric conic sections having a common focal point. These telescopes were first studied systematically by Wolter[2]. Giacconi et al. [3] have recently reviewed this subject. Mangus and Underwood[4] have previously discussed some of the design considerations for these telescopes. We have performed a systematic evaluation of the principal properties of X-ray mirrors such as shown in Figure 1 and called Telescopes of the First Kind by Wolter; in this case the X-rays successively strike a paraboloid and a hyperboloid which are confocal, coaxial and arranged so that the angular deviations of a ray at the two surfaces are additative. These have a shorter focal length for a given aperative than the other systems considered by Wolter and also have certain structural advantages resulting from the fact that the optical surfaces intersect. We find that our results for resolution, focal plane curvature, effective area, and finite source distance effects can be summarized by simple empirical formulae which should be useful to people considering X-ray telescope experiments.

Description of the Surface

The equations for a paraboloid and hyperboloid which are coaxial and confocal can be written:

$$r_p^2 = P^2 + 2PZ + \frac{4e^2 Pd}{e^2 - 1} \qquad \text{(Paraboloid)}$$

$$r_h^2 = e^2 (d + Z)^2 - Z^2 \qquad \text{(Hyperboloid)}$$

In the above equations the origin is at the focus for axial rays, Z is the coordinate along the axis of symmetry, and r is the radius of the surface of Z. The common focus is at $Z = \frac{-2e^2 d}{(e^2 - 1)}$. There are thus three independent

parameters, e, d, and p, which describe the surfaces; it is useful, however, to consider the surfaces to be determined by three other parameters, Z_o, α, and ξ which are more easily visualized, and are defined as follows:

Z_o = The distance from the axial ray focus to the intersection plane of the paraboloid and hyperboloid; this is essentially the focal length and determines the scale of the optics.

α = $1/4$ arc tan (r_o/Z_o) = $1/2$ $(\alpha_p{}^* + \alpha_h{}^*)$ where r_o is the radius of the surfaces at their intersection and $\alpha_p{}^*$, $\alpha_h{}^*$ are the grazing angles between the two surfaces and the path of an axial ray which strikes at an infinitesimal distance from the intersection. Note that if tan $\theta_p{}^*$ and tan $\theta_h{}^*$ are the slopes of the two surfaces at the intersection, then $\alpha_p{}^* = \theta_p{}^*$, $\alpha_h{}^* = \theta_h{}^* - 2\theta_p{}^*$, and $\alpha = 1/2$ $(\theta_h{}^* - \theta_p{}^*)$.

ξ = $\alpha_p{}^*/\alpha_h{}^*$ = the ratio of the two grazing angles for an axial ray striking near the intersection of the two surfaces.

The asterix is used in this notation to specify values of the variables at the intersection plane.

The original parameters, e, d, and p can then be determined as follows:

a). $\theta_p{}^* = (\dfrac{2\xi}{1+\xi})$ (α)

b). $\theta_h{}^* = (\dfrac{2(1+2\xi)}{1+\xi})$ (α)

c). $P = Z_o$ tan (4α) tan $\theta_p{}^*$

d). $d = Z_o$ tan (4α) tan $(4\alpha - \theta_h{}^*)$

e). $e = \cos(4\alpha)$ $(1 + \tan(4\alpha) \tan \theta_h{}^*)$

Two other parameters, L_p and L_h, the lengths of the paraboloid and hyperboloid sections, are necessary to define an actual mirror. We have considered L_p to be a free design parameter but have constrained L_h to be just long enough so that axial rays striking the front of the paraboloid also strike the back of the hyperboloid. This results in some loss of off-axis rays which will be discussed below. This constraint results in the following equation for L_h:

$$\frac{L_h}{L_p} = \frac{P}{ed + (e-1)L_p} \approx \frac{\xi}{1 + \dfrac{\xi L_p}{Z_o}} \tag{1}$$

The geometrical properties of a given telescope and source are thus determined by the four free design parameters $(Z_o,\ \alpha,\ \xi,\ L_p)$ and the angle θ between the incident rays and the optical axis.

Procedure

Our principal analytical technique has been a Monte-Carlo ray-tracing procedure. The input data to the computer programs include a geometrical description of the telescope, the surface material of the reflecting surfaces, the wavelength of the incident X-rays, and the location of the point source of X-rays. A random position on the telescope front aperture is chosen, and an incident ray is required to go through this point. The ray is followed until it is reflected onto the focal plane properly, or is lost. The surface reflection efficiency is calculated by the approximate formulae given by Giacconi et al.[2]. Additional random rays are traced in this way until the desired results are known with sufficient accuracy. The results include the telescope effective area, $A_{effective}$, and r. m. s. blur circle radius, σ, for both flat and optimally curved focal surfaces. The formal definitions of these quantities are as follows:

$$A_{effective} = A \left(\frac{1}{N}\right) U_o$$

$$\sigma^2 = \sigma_x^2 + \sigma_y^2$$

$$\sigma_x^2 = \frac{U_{xx}}{U_o} - \left(\frac{U_x}{U_o}\right)^2$$

and

$$U_o = \sum_i \epsilon_i^p \epsilon_i^h$$

$$U_x = \sum_i x_i \epsilon_i^p \epsilon_i^h$$

$$U_{xx} \quad \sum_i x_i^2 \epsilon_i^p \epsilon_i^h$$

The summations include only those rays which reach the focal plane. ϵ_i^p and ϵ_i^h are the reflection efficiencies for reflection from the paraboloid and hyperboloid respectively. A is the geometric area which rays may traverse at the front aperture, and N is the number of random rays incident on this geometric area. x_i and y_i are the coordinates of the point of intersection of a ray with the focal plane. The entries in all of the tables and graphs of this paper which were calculated by this Monte-Carlo procedure exhibit the random fluctuations characteristic of the method.

Resolution

A systematic study of many different telescopes reveals that the RMS blur circle radius can be described quite accurately by a simple empirical relation.

$$\sigma_D = \frac{\sqrt{\xi}}{5} \frac{\tan^2 \theta}{\tan \alpha} \left(\frac{L_p}{Z_o}\right) + 4 \tan \theta \tan^2 \alpha \tag{2}$$

where σ_D is expressed in radians. The coefficient of the second term was fixed at 4.0* (see Page 15), and the factor of $\left(\frac{1}{5}\right)$ is a fit to a selection of points in the region.

$$\frac{1}{2}^{\mathrm{O}} \leq \alpha \leq \frac{7}{2}^{\mathrm{O}} \qquad\qquad 0 \leq \theta \leq 30'$$

$$.035 \leq \left(\frac{L_p}{Z_o}\right) \leq .176$$

$$\frac{1}{4} \leq \xi \leq 4$$

Out of 200 points used in the fit only 20 of the points differ from the formula by more than 20%, and none differ by more than 30%. These deviations may be due to our random procedure or, more likely, to the presence of additional terms in the expansion of σ_D.

The presence of the second term in the formula is due to the fact that Wolter telescopes of this type do not exactly satisfy the Abbe Sine Rule[2]. We have discovered that this second term disappears for telescopes of the Wolter-Schwarzchild variety[5]. These latter telescopes are similar to the paraboloid-hyperboloid telescopes but exactly satisfy the Abbe Sine condition. They will be the subject of a later paper.

The image distribution is quite different for the two cases in which one of the two terms dominates: When the first term dominates the image distribution in the Gaussian plane is peaked near the center and falls off approximately as $\frac{1}{r}$ to a maximum radius determined by L_p; whereas when the second term dominates the image distribution becomes a ring which is unpopulated at the center.

The resolution is seen to be a reasonably slow function of the parameter ξ, and there are advantages to the choice $\xi = 1$, which approximately maximizes the collecting area for a given total mirror length or polished area, and also maximizes the X-ray reflection efficiencies at short wavelengths for a given diameter to focal length ratio. In the remainder of this paper we usually will set $\xi = 1$, and this value may be assumed where no other value is indicated. This also results in $\theta_p \approx \alpha_p \approx \alpha_h \approx \alpha; \theta_h \approx 3\alpha.$

In Stellar X-ray astronomy the most important design parameter usually is the telescope collecting area, and it is useful to re-express equation (2) in terms of the area rather than the segment length. To fix the collecting area, the scale must be chosen by specifying one of the lengths, r_o, Z_o, or L_p. The geometrical area presented to axial rays is then given by

$$A = (2\pi r_o)(L_p \tan \alpha) \tag{3}$$

and for small α we can re-express equation (2) as

$$\sigma_D \approx (\frac{1}{40\pi}) \frac{\tan^2 \theta}{\tan^3 \alpha} (\frac{A}{Z_o^2}) + 4 \tan \theta \tan^2 \alpha \tag{4}$$

The rms blur circle radius is given as a function of the incident angle for one value of (A/Z_o^2) and various values of α in Figure 2. The solid lines were calculated using equation (4) while the points are the results of the Monte-Carlo ray tracing procedure.

In Figures 3 and 4 the results of equation (4) are plotted as a function of the parameter α for various values of (A/Z_o^2) and two fixed incident angles ($\theta = 5'$, $10'$). The curves exhibit an optimum value of α for a given incident angle, area, and focal length. The optimum value of $\alpha = \alpha^\dagger$ is given by

$$\tan \alpha^\dagger = \left[(\frac{3}{320\pi}) \tan \theta (\frac{A}{Z_o^2}) \right]^{1/5} \tag{5}$$

Note that $\alpha^\dagger$ is fairly insensitive to θ and (A/Z_o^2). The results of equation (5) for typical values of θ and $(\frac{A}{Z_o^2})$ are plotted in Figure 5. The optimum value of α is about one degree for most practical cases.

Focal Plane Curvature

The optimally curved focal plane can be described in terms of a parameter, $\delta(r)$ which is the axial distance of the surface above the normal focal plane at a distance r off axis. Empirically,

$$\delta = \frac{0.11\,(1+\xi)}{2} \cdot \left(\frac{r^2 L_p}{Z_o^2}\right) \left(\frac{1}{\tan \alpha}\right)^2 \tag{6}$$

The accuracy of this formula is roughly the same as that of equations (2) and (4). The effect of using a flat focal plane is to double the first ($\tan^2 \theta$) terms in equations (2) and (4).

Collecting Area

Figure 6 is a plot of a typical telescope as a function of effective area λ for several values of θ. The mirror surface is made of a nickel alloy, kannigen, and is similar to one we have flown on several rocket flights. Its descriptive parameters are: $r_o = 11.43$ cm; $L_p = 22.86$ cm; and $Z_o = 132.08$ cm. The surface reflection efficiency as a function of wavelength and grazing angle has been taken into account using the formalizm presented in Reference (3), Pages 12-14. The dip at about 14 $\overset{o}{A}$ is due to the L absorption edges of nickel. The effective area of this and similar telescopes can be described very well as the product of three factors

$$A_{effective} = [A]\,[V(\alpha, \theta)]\,[R(\alpha, \lambda)] \tag{7}$$

where A is the geometric area, $V(\alpha, \theta)$ is a "vignetting factor," $R(\alpha, \lambda)$ is the surface reflection efficiency for the particular material used, and λ is the wavelength of the X-rays. Our ray-tracing studies show that the vignetting factor is negligibly dependent upon $\left(\frac{L_p}{Z_o}\right)$. Figure 7 is a plot of $V(\alpha, \theta)$ vs. θ and α; this result depends upon our technique for choosing the length of the hyperboloid. We find that:

$$V(\alpha, \theta) \approx 1 - (2/3)\,(\theta/\alpha) \qquad (\theta < \alpha) \tag{8}$$

C-8

Finite Distance Effects

We have studied the effects of placing the point source of X-rays at a finite distance from the telescope. Tracing rays from this new source location shows that the focal plane is shifted from the normal focal plane approximately as the simple lens law predicts. That is

$$\frac{1}{p} + \frac{1}{q} = \frac{1}{z} \tag{9}$$

where p and q are the axial distances from the central plane to the point source and new focal plane respectively.

The blur circle radius for an on-axis point source at finite distance is approximately proportional to $\frac{L_p}{Z_o} \tan \alpha$. Figure 8 shows the dependance of σ_D on α, $\frac{L_o}{Z_o}$, and $\frac{p}{Z_o}$. These results can be approximated by

$$\sigma_D = 4 \left(\frac{L_p}{Z_o}\right) \tan \alpha \left(\frac{Z_o}{p}\right)^2 \tag{10}$$

(for on-axis rays).

There is also a loss of collecting area at finite distances which is primarily due to vignetting, although there is also some loss in reflection efficiency; the latter effect is less than might be expected because the grazing angles at the two surfaces vary in opposite directions. Empircally we have found that the loss of effective area due to vignetting from finite sources goes approximately as

$$A(P) \approx \frac{1 - \dfrac{5Z_o}{2p}}{1 + \dfrac{5Z_o}{2p}} \tag{11}$$

This formula is accurate to about 2%. Note that there is negligible dependence upon either α or L_p.

Nested Surfaces

Equation (2) shows that σ_D increases with L_p, so that increasing the collecting area by lengthening the mirrors results in a loss of resolution. The collecting area may be increased without a substantial loss of resolution by nesting additional surfaces inside the original surface rather than increasing the mirror length. The tolerances for adding such additional surfaces are determined by the focal plane scale rather than by the wavelength since diffraction limited performance is not expected even from a single surface.

Our method of designing multiple surface telescopes begins with the choice of Z_o, L_p, r_o, and L_h of the largest surface. The minimum wall thickness necessary for structural rigidity is also fixed. Additional surfaces are then added with smaller values of r_o, but with the same values of Z_o, L_p, and L_h. These additional surfaces are chosen to be just small enough to pass all axial rays which strike the next larger surface. In practice the limiting condition is that the back of the hyperboloid should not interfere with rays striking near the intersection plane $(Z = Z_o)$ of the next larger surface. Hence the radii of the inner surfaces are determined at $Z = Z_o - L_h$ and not at the central plane where $Z = Z_o$. We calculate the parameters describing the paraboloid and hyperboloid of the smaller surfaces by means of an itterative computer program. The choice of L_h follows the scheme of equation (1) only for the largest surface. The choice of a curved focal plane must also be a compromise between the several surfaces.

Figure 9 is an example of the effect of the parameter L_p and the number of surfaces upon effective area and resolution. Nine points have been calculated, and the lines have been sketched in to interpolate approximately. Figure 10 is an example of the effect of mirror wall thickness on effective

area for a 3 surface telescope and a 5 surface telescope. The telescope parameters for Figures 9 and 10 are: $Z_o = 609.6$ cm; $r_o^{max} = 44.75$ cm; and $L_o = 55.88$ cm. The advantages of the multiple surface approach are obvious, and the ray tracing results show that no unexpected consequences of nesting surfaces occur.

Conclusions

The empirical formulae of this paper should be adequate for the preliminary design of X-ray telescopes and associated test facilities. The ray-tracing techniques used in this study also are easily adapted to determining the properties of a particular design and evaluating the effects of finite tolerances and mechanical deformations upon its performance.

Acknowledgments

Many people at AS&E have contributed to the development of X-ray telescope technology. The contributions of Dr. Ricardo Giacconi and Professor Bruno Rossi, who first suggested these telescopes for astronomical use, Drs. G. Vaiana, H. Gursky, W. Reidy, and Mr. T. Zehnpfennig have been particularly important.

FIGURE CAPTIONS

Figure 1   A representation of the type of paraboloid-hyperboloid telescopes discussed in this paper. The back hyperboloid focus is confocal with the paraboloid focus.   The front focus of the hyperboloid is also the focus of the telescope.

Figure 2   The rms blur circle radius is given as a function of the incident angle for one value of (A/Z_o^2) and several values of α.   The solid lines were calculated using equation (4) while the points are the results of the Monte-Carlo ray tracing procedure.

Figure 3   The rms blur circle radius is given as a function of α for several values of (A/Z_o^2). θ is fixed at 5'. The curves were calculated using equation (4).

Figure 4   The rms blur circle radius is given as a function of α for two values of (A/Z_o^2). θ is fixed at 10'. The curves were calculated using equation (4).

Figure 5   The optimum value of α is given as a function of θ for several values of (A/Z_o^2).   The curves were calculated using equation (5).

Figure 6   The effective area of a typical telescope as a function of X-ray wavelength, λ, for two values of θ.

Figure 7   A plot of the Vignetting factor, $V(\alpha, \theta)$, as a function of θ for several values of α.

Figure 8   The rms blur circle radius is given as a function of the finite source distance divided by the focal length.   The results are shown for several values of (L_p/Z_o) and α.

Figure 9   The rms blur circle radius at $\theta = 10'$ is given as a function of
            effective area at $\theta = 0$ for specific telescopes. The effect of
            L_p and the number of surfaces is shown. Nine points have been
            calculated and the lines have been sketched in to interpolate
            approximately.

Figure 10   The telescope effective area is given as a function of the mirror
            wall thickness for a 3 surface telescope and a 5 surface tele-
            scope.

REFERENCES

1. Giacconi, R., and Rossi, B., _J. Geophy. Res._ 65, 773 (1960).

2. Wolter, H., _Ann. Physik_ 10, 94 (1952).

3. Giacconi, R., Reidy, W. P., Vaiana, G. S., VanSpeybroeck, L. P.,
    and Zehnpfennig, T. F., _Space Sci. Rev._ 9, 3 (1969).

4. Mangus, J. D., and Underwood, J. H., _Appl. Opt._ 8, 95 (1969).

5. Wolter, H., _Ann. Physik_ 10, 286 (1952).

---

*This term is easily derived for short cone optics and must be present for any two surface mirror with non-aero first surface slope at the intersection of the two surfaces. The focal plane coordinates of an off-axis ray in the x-z plane which strikes near the intersection are given by:

$$x_i = -Z_o \tan \theta \frac{\left\{\dfrac{\cos^2 2\alpha}{\cos^2 4\alpha}\right\} \left\{1 + \cos 2\phi \tan^2 2\alpha\right\}}{1 - \tan \theta \cos \phi \tan 4\alpha}$$

$$y_i = -Z_o \tan \theta \frac{\left\{\dfrac{\cos^2 2\alpha}{\cos^2 4\alpha}\right\} \left\{\sin 2\phi \tan^2 2\alpha\right\}}{1 - \tan \theta \cos \phi \tan 4\alpha}$$

where ϕ is the azimuthal angle at which the ray strikes the surface. This result does not depend on ξ.
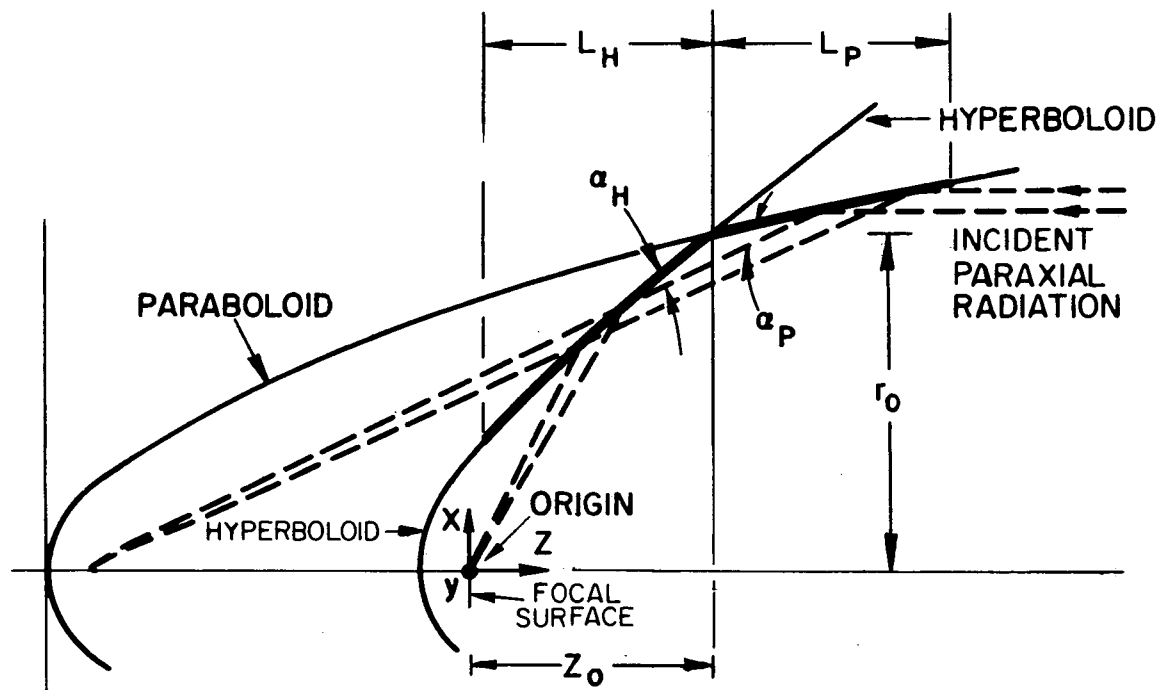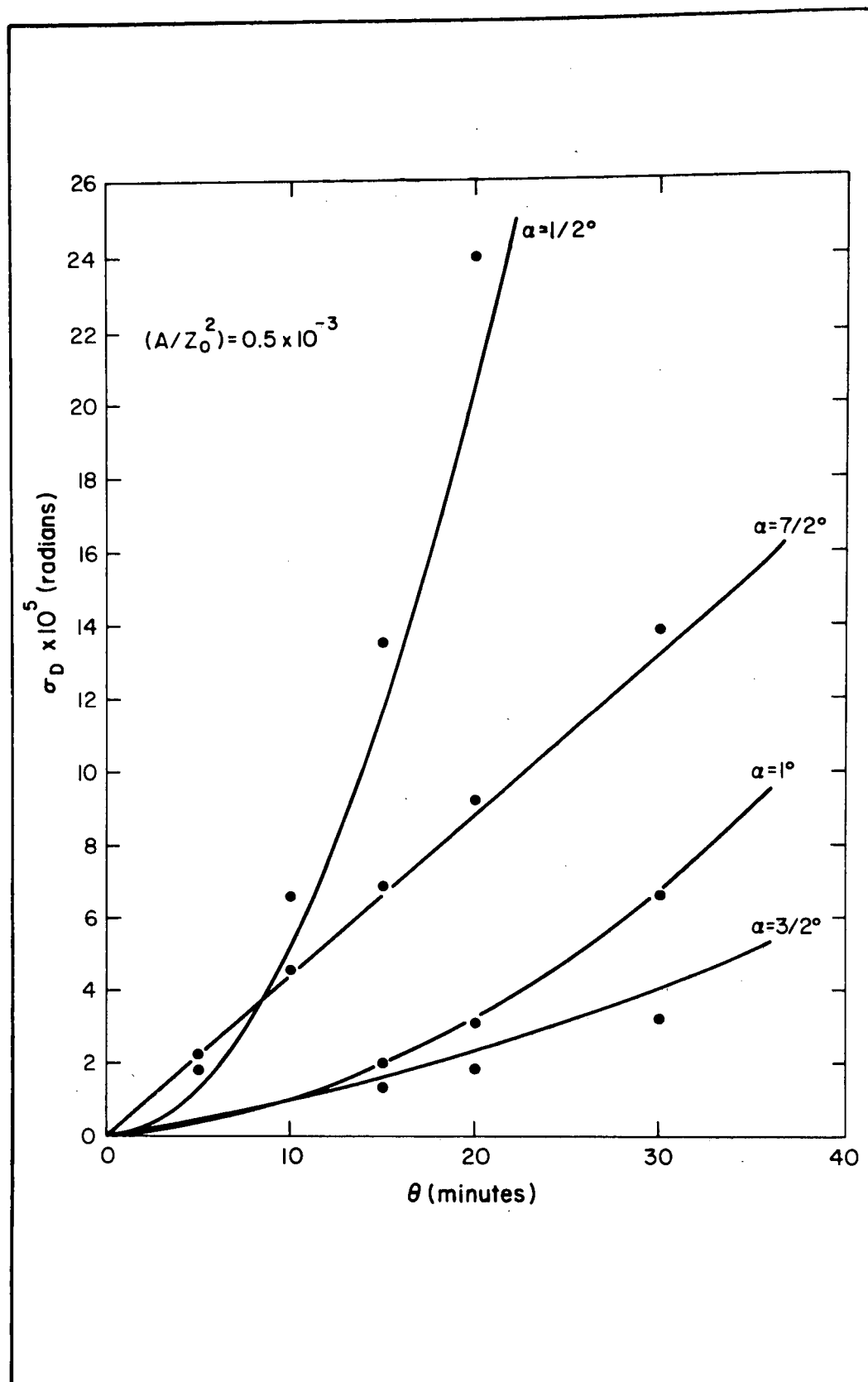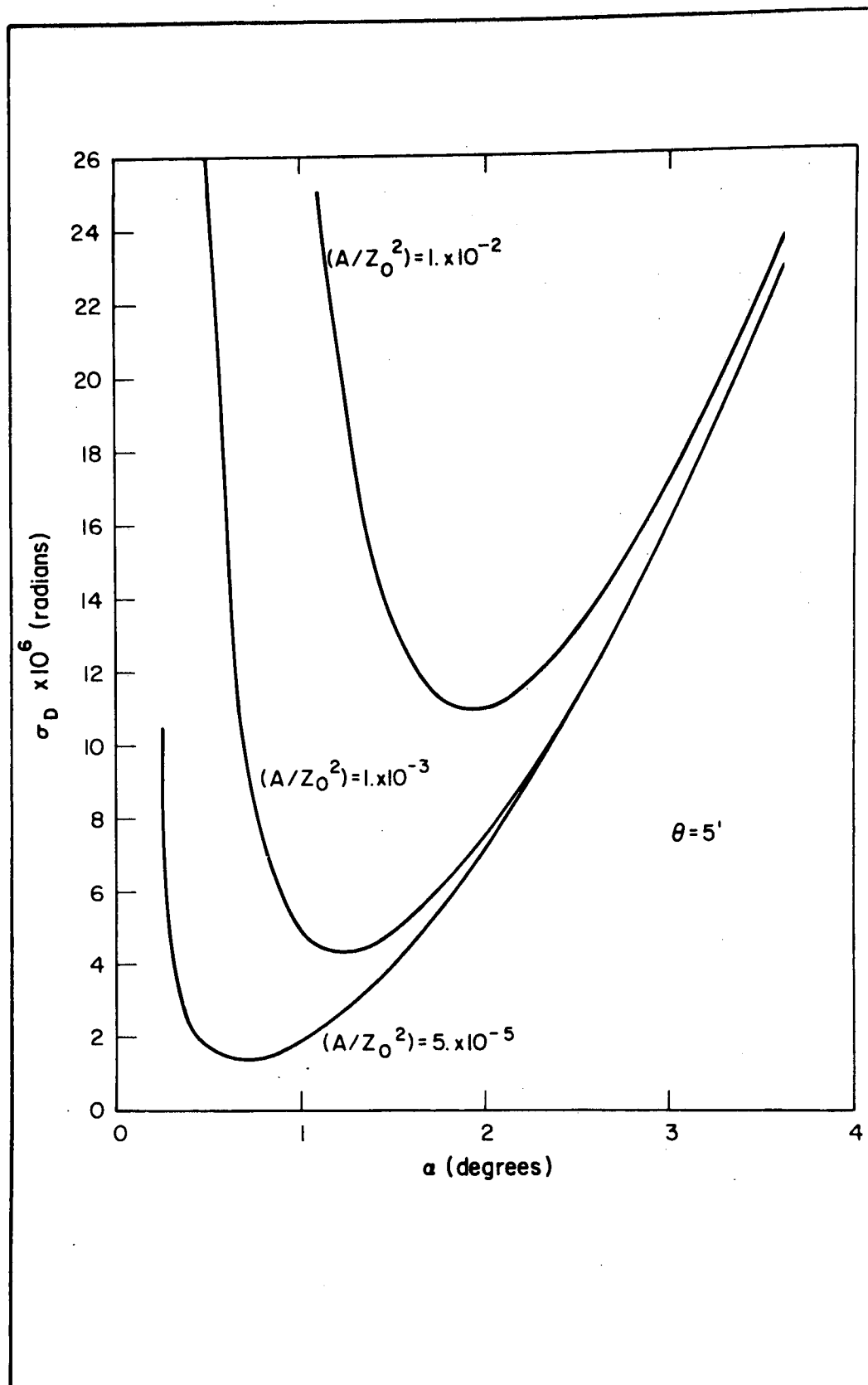
Figure 1

Figure 2

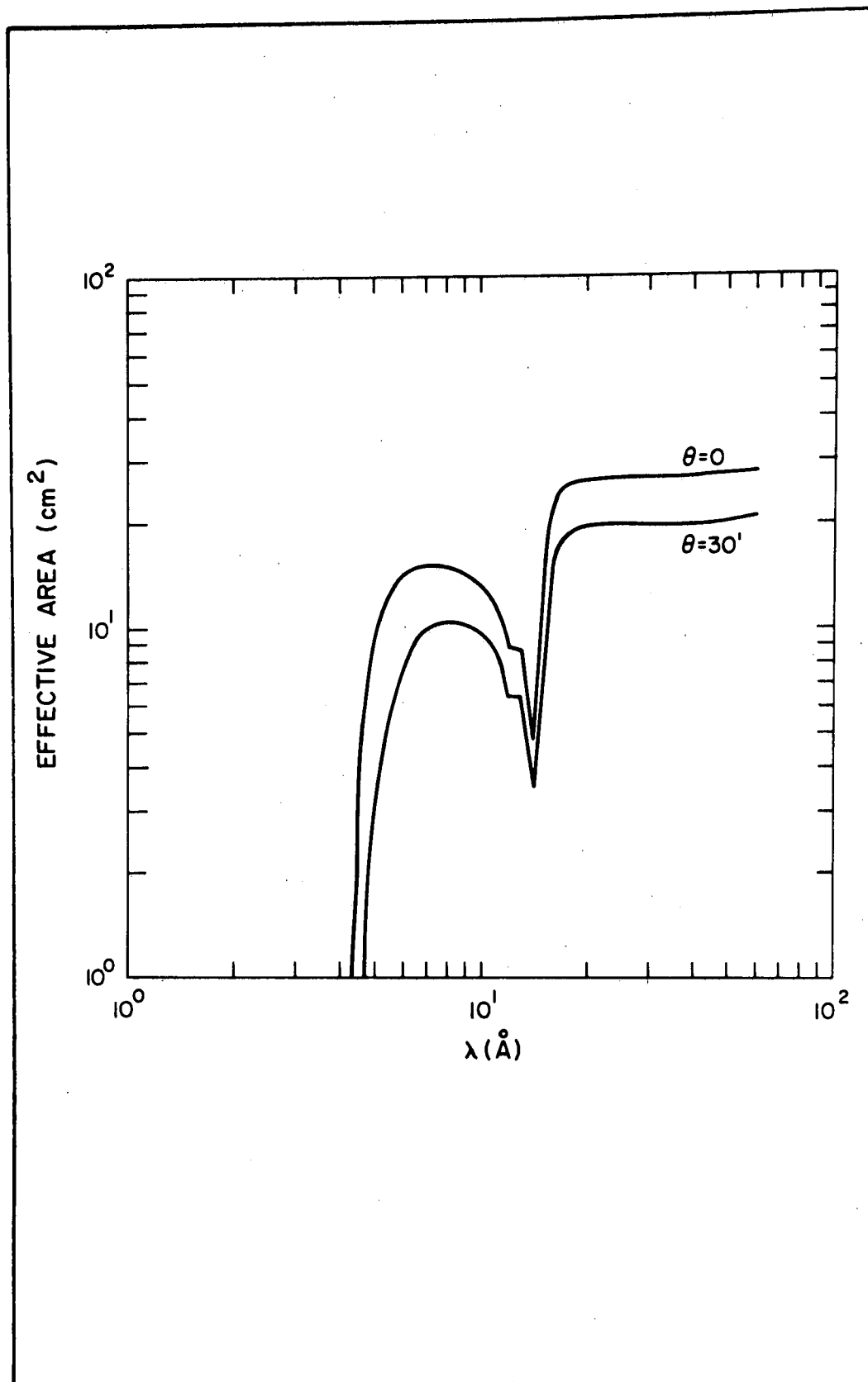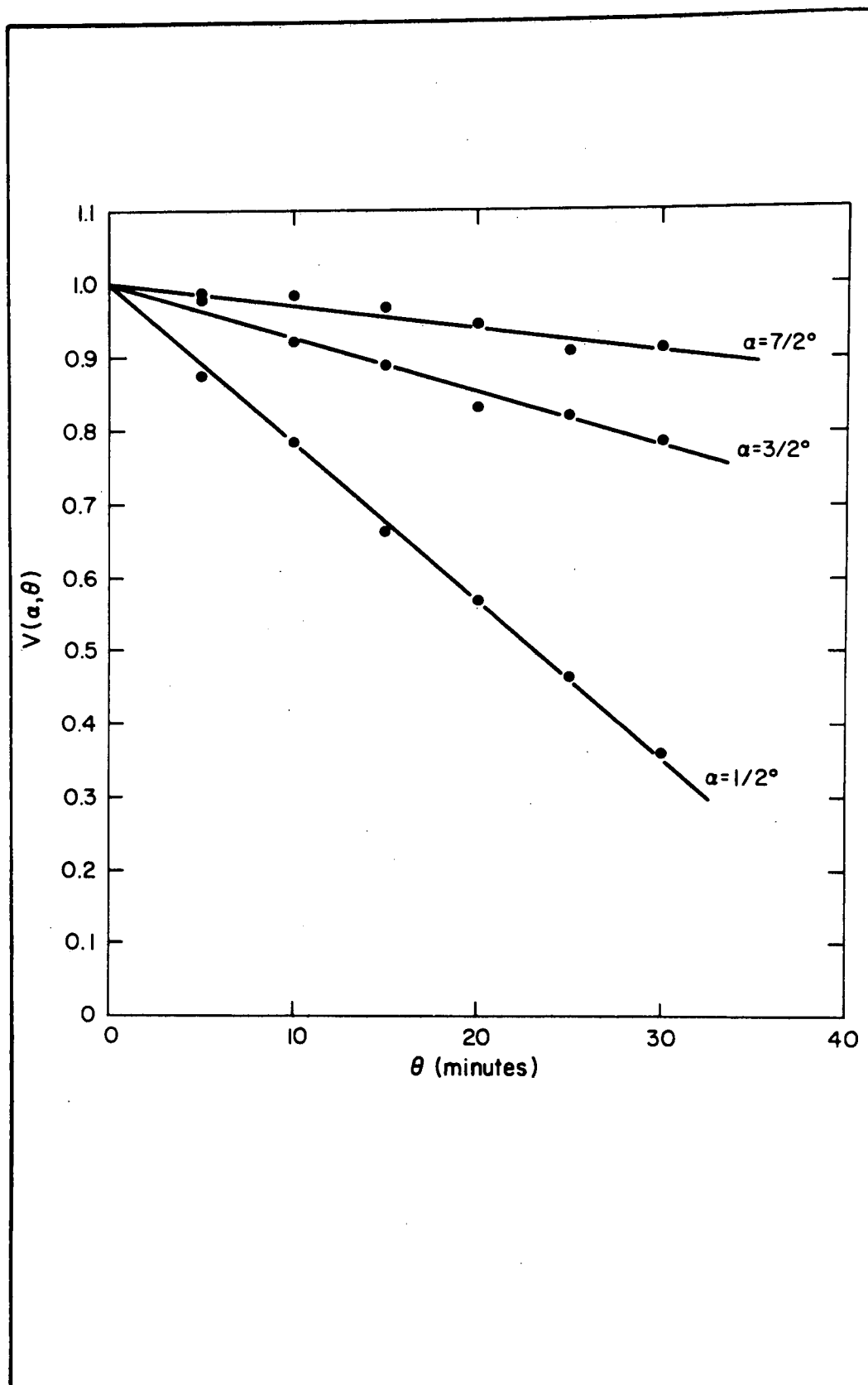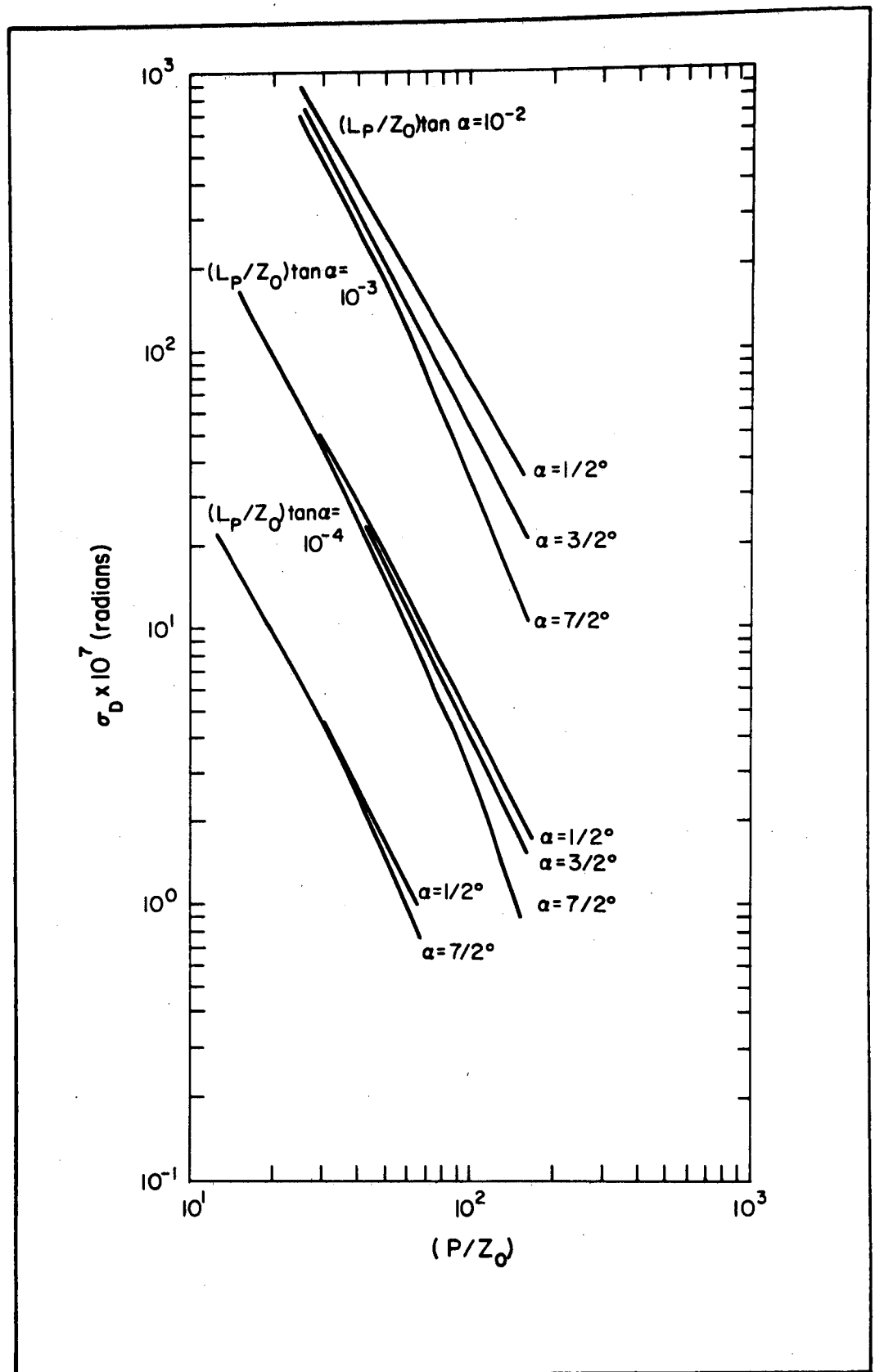Figure 3
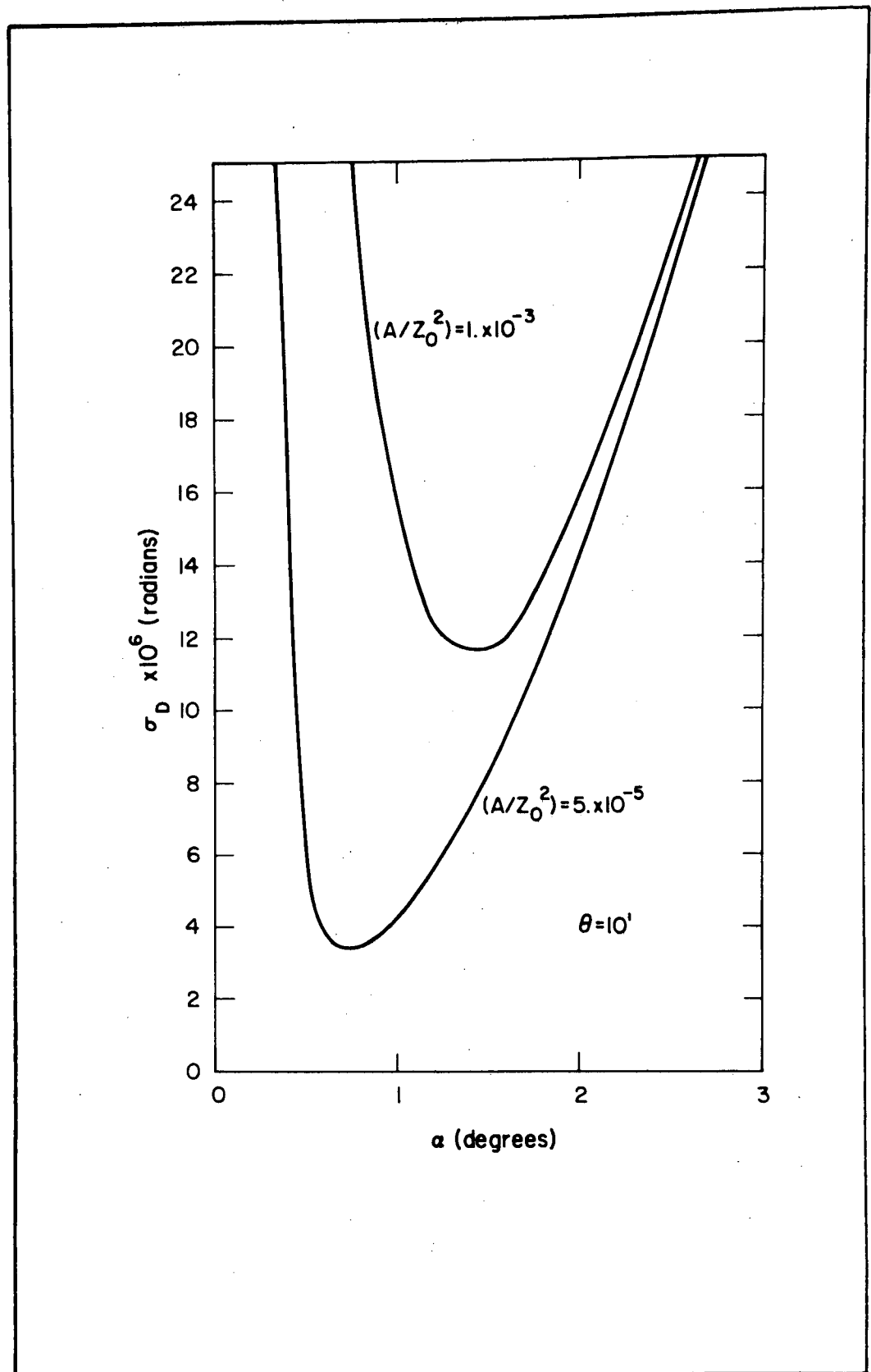
Figure 4
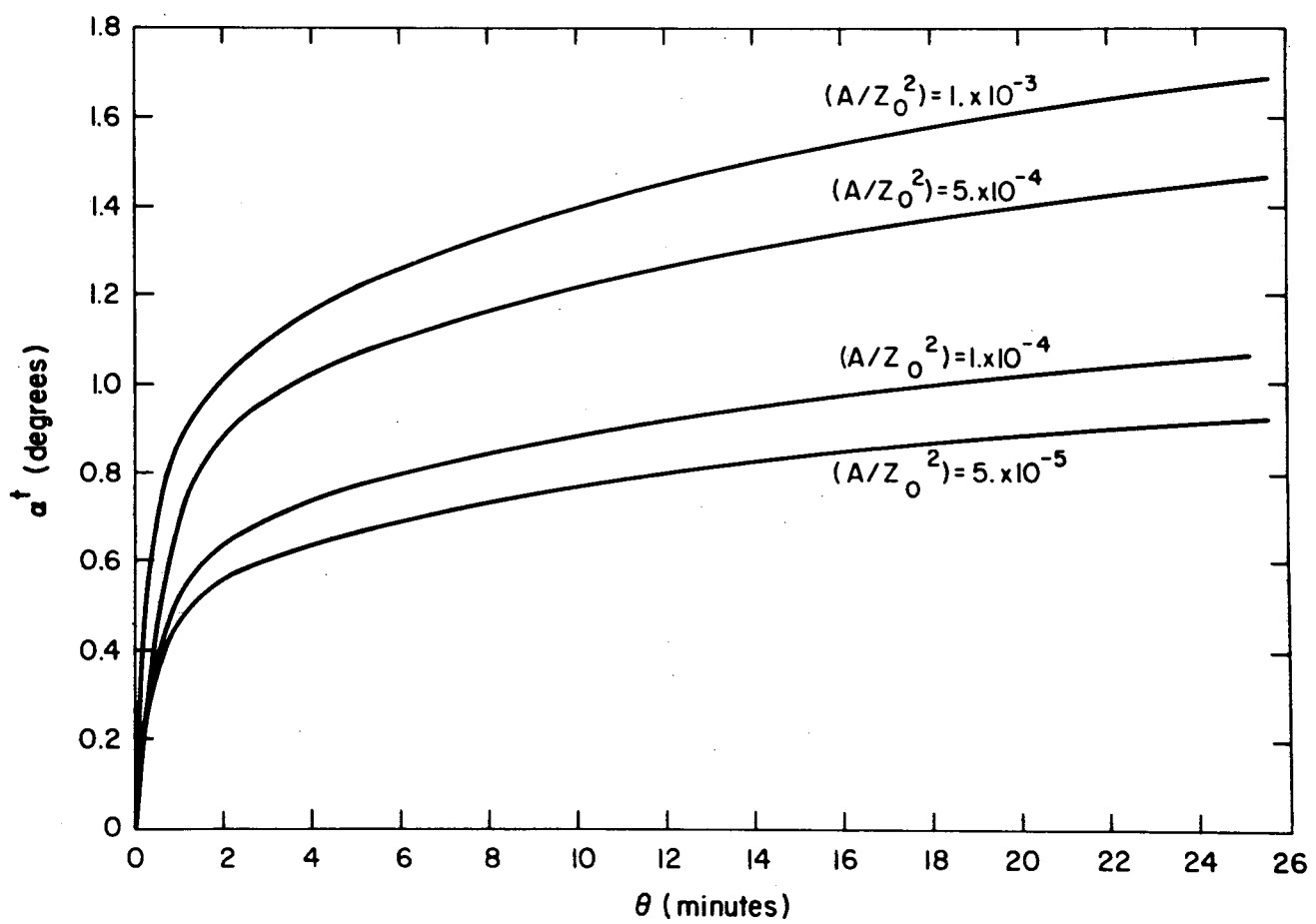
Figure 5

Figure 6

Figure 7

Figure 8

C-23

Figure 9

Figure 10